

Study of End-loss Ion Flux in the GAMMA 10/PDX
Tandem Mirror for Divertor Simulation

Kazuya Ichimura

Doctoral Program in Physics

Submitted to the Graduate School of
Pure and Applied Sciences
in Partial Fulfillment of the Requirements
for the Degree of Doctor of Philosophy in
Science

at the
University of Tsukuba

CONTENTS

Chapter 1	Introduction	3
Chapter 2	Experimental Apparatus	7
2.1	GAMMA 10/ PDX Tandem Mirror	7
2.2	Plasma Confinement in a Tandem Mirror	8
2.2.1	<i>Plasma confinement by a Mirror Magnetic Field</i>	8
2.2.2	<i>Plasma Confinement by Electrostatic Potential</i>	10
2.3	Specifications of GAMMA 10/PDX Mirror Cells.....	12
2.3.1	<i>Central-Cell</i>	12
2.3.2	<i>Anchor-Cell</i>	12
2.3.3	<i>Plug/Barrier-Cell</i>	12
2.3.4	<i>End-Cell</i>	12
2.4	Plasma Heating and Fueling	13
2.4.1	<i>Plasma Gun</i>	13
2.4.2	<i>Ion Cyclotron Range of Frequency Heating</i>	14
2.4.3	<i>Electron Cyclotron Resonance Heating</i>	14
2.4.4	<i>Neutral Beam Injection</i>	14
2.4.5	<i>Gas Puffs</i>	14
2.4.6	<i>Supersonic Molecular Beam Injection</i>	15
2.5	Plasma Diagnostics	15
2.5.1	<i>Microwave Interferometers</i>	15
2.5.2	<i>Diamagnetic Loop</i>	15
2.5.3	<i>Neutral Particle Analyzer</i>	16
2.5.4	<i>Thomson Scattering System</i>	16
2.5.5	<i>Directional Mach Probe</i>	16
2.5.6	<i>Calorimeter</i>	16
2.5.7	<i>High Speed and Middle Speed Cameras</i>	17
2.5.8	<i>End Plate</i>	17
2.5.9	<i>Loss Electron Diagnostic</i>	17
2.5.10	<i>End-Loss ion Energy Analyzer</i>	18
2.6	Divertor Simulation Experimental Module.....	19
Chapter 3	Method of the End-Loss Ion Flux Analysis	21
3.1	Measurement of the Ion Flux by ELIEA	21
3.2	Evaluation of the Ion Energy	22
3.3	Evaluation of the Ion Particle Flux	24
3.4	Evaluation of Measurement Errors	24
Chapter 4	Analysis of the GAMMA 10/PDX End-Loss Flux in Standard Experiments	25
4.2	<i>V-I Characteristics and Ion Energy Distribution in Standard Operations</i>	26
4.3	<i>Energy Analysis on the Standard End-Loss Ion Flux</i>	27

4.3.1	<i>Energy Analysis by Single-Component Maxwellian Model</i>	27
4.3.2	<i>Energy Analysis by Double-Components Maxwellian Model</i>	30
4.4	Analysis on the Ion Particle Flux	33
4.5	Typical Radial Profile of the End-Loss Ion Flux	36
Chapter 5	Enhancement of the Ion Particle Flux by Additional Fueling and Heating	39
5.1	Ion Particle Flux in Previous Works	39
5.2	Enhancement of the Particle Flux by Supersonic Molecular Beam Injection	40
5.3	Enhancement of the Particle Flux by ICRF Heating in Anchor Region	42
5.3.1	<i>Additional ICRF Heating with East Anchor DAT</i>	42
5.3.2	<i>Additional ICRF Heating with West Anchor DAT</i>	44
5.3.3	<i>Gas Puffing with Anchor DAT</i>	46
5.3.4	<i>Simultaneous ICRF Heating in East and West Anchor-Cells</i>	49
5.3.5	<i>Effect of Plasma Potential on Particle Flux Enhancement</i>	51
5.4	Enhancement of the Particle Flux by Plasma Gun	51
5.5	Summary of the High Particle Flux Operations	55
Chapter 6	Numerical Analysis on the End-Loss Flux Production	56
6.1	Development of Flux Calculation Code	56
6.1.1	<i>Original Plasma Build-Up Code</i>	56
6.1.2	<i>Upgrade for Flux Calculation Code</i>	57
6.1.3	<i>Calculation of the Cell-To-Cell Transport of Plasma Particles</i>	59
6.1.4	<i>Particle Balance Equations</i>	61
6.1.5	<i>Energy Balance Equations</i>	62
6.2	Evaluation of Axial Confinement Time	63
6.3	Analysis of the End-Loss Ion Flux by the Code	64
6.5	Discussion	66
Chapter 7	Conclusion	70
Concluding Remarks	71
Acknowledgements	72
References	73

Chapter 1 Introduction

In recent fusion study, experimental works with linear plasma machine are being noted since these works play an important role for development of critical part of a fusion reactor, which is called divertor [1]. However, plasmas in conventional linear experimental devices generally have low temperature and therefore there exist a gap of plasma parameters between the real divertor and linear divertor simulator. In order to fulfill the gap, a linear divertor simulator with high plasma temperature is needed. Finding such experimental method is attractive and interesting not only because it is important for the divertor study, but also it will bring deeper understanding of plasma physics in linear systems such as particle transport.

As many researchers notices, a fusion reactor is one of the most promising energy sources for human beings. The fuels for a fusion reactor; deuterium and tritium exist in seawater and therefore they are virtually infinite. Also, a fusion reactor is more acceptable to our society than a fission reactor since a fusion reaction has no risk of reactor's run-away. So far, a large number of researchers have been working on the fusion study and now, in 2015, the study is on the phase of confirming the operation scenario of fusion plasma by upcoming experimental fusion reactor ITER [2]. In order to achieve fusion plasma, plasma must be heated to the temperature of more than 10 keV in well conditioned vacuum chamber. In such case, enormous load of heat and plasma particle flux strikes the inner wall of the vacuum vessel and the wall material will be deeply damaged. Then, in order to develop fusion power plant, the handling of such heat and plasma particle is critical. An idea of divertor configuration was proposed in order to protect the wall materials from the heat load.

With the divertor configuration, the heat and particle flux emitted from the fusion plasma are led to the divertor region, whose design is specialized to reduce heat and moderate particle flux incident to the wall. The plasma entered to the divertor region is cooled by the interaction with an impurity gas such as argon or neon [3]. When the plasma in the divertor region is cooled enough, plasma detachment [4], which is a strong neutralization of the plasma in front of the wall, will occur and the damage for the wall materials are drastically decreased. In the expected fusion reactor, the power output of the plasma is so large and precise control of the detachment state is required. Therefore we must study the physics of divertor plasma behavior and plasma wall interactions (PWI) in order to develop a divertor system suitable to future fusion reactor.

In such studies, an experimental work with linear plasma device is quite convenient and important. Geometry of a linear device is relatively simple and therefore it is easy for workers to operate a device and to analyze physical phenomena seen in the experiment. However, due to physical or technical difficulty, plasma parameters such as plasma temperature, density and particle flux are usually lower than those in tokamak divertor. Especially it is difficult to obtain high plasma temperature and high plasma density simultaneously in one linear machine. Therefore in the study of divertor physics, it is necessary to perform the divertor

simulation experiments in many linear devices of different parameter ranges. For example, the physical process of plasma detachment is investigated in NAGDIS II [5], MAP-II [6] and TPD-Sheet IV [7]. In APSEDAS [8] and PSI-2(JULE-PSI) [9], effects of the plasma irradiation on target materials are studied. For the investigation of PWI in steady state and high particle flux conditions, research projects with MAGNUM-PSI [10] and MPEX [11] are in progress. Target plasma parameters of those machines and the plasma parameters expected in ITER [12] are listed in Table 1.

Table 1, Target plasma parameters of linear divertor machines and plasma parameters expected in SOL and divertor region of ITER plasma.

	Plasma Temperature (eV)	Particle Flux (particles/m ² sec)	Heat Flux (MW/m ²)
ITER SOL Plasma	> 100	10 ²³	150 ~ 200
ITER Divertor Plasma at Target Plate	0.1 ~ 15	10 ²³ ~ 10 ²⁵	~ 10
NAGDIS II	5 ~ 10	10 ²³	0.9
MAP-II	~ 10	10 ²²	~ 0.1
TPD-Sheet IV	~ 15	10 ²³	0.6
APSEDAS	~ 20	10 ²¹ ~ 10 ²²	~ 0.1
PSI-2	1 ~ 20	10 ²¹ ~ 10 ²³	2
MAGNUM-PSI	0.1 ~ 10	10 ²³ ~ 10 ²⁵	10
MPEX	~ 35	10 ²⁴	10 ~ 40

With linear machines, plasma detachment in parameter range of low plasma temperature (< 20eV) is studied so far. In tokamaks, it is found that there is a disagreement of the experimental result and numerical simulation [13] and it is suggested that the high energy tail component of the particle's energy distribution (super thermal electrons) can be the cause of the disagreement [14]. Therefore divertor simulation experimental studies with high plasma temperature and high controllability of particles' energy are needed to confirm the divertor operation in fusion reactors.

Choice of the plasma generation source mainly determines the characteristics of the plasma for divertor simulator. For example, steady state plasma can be produced by helicon wave [15] or low energy arc discharge; however the plasma temperature is low in these cases. The pulse plasma source such as magneto hydro dynamics (MPD) arcjet, cascaded cathode arc [16] and compact toroid injection system [17] are able to generate plasma with heat power of several GW while their duration time is less than one millisecond. In

order to obtain higher energy of the incident plasma particles, potential biasing for the target plate is applied in machines with lower plasma temperature. With the potential biasing for low temperature plasma, the average energy of the particle is increased; however, the energy distribution of the particle is unchanged. In such case, broad energy distribution of particles observed in high temperature plasma cannot be reproduced. For the study of PWI or divertor plasma behavior with broad energy distribution, a plasma source capable of producing high plasma temperature is required. Thus, plasma heating by ICRF, ECRH or EBW is planned to be installed in MPEX. The tandem mirror device GAMMA 10/PDX has MPD arcjet, ICRF, ECRH and NBI for the production and heating of the plasma and the machine can be a candidate of plasma source of divertor and PWI study in high temperature region [18].

A tandem mirror is linear plasma machine that has functions of plasma confinement by mirror magnetic field and electrical potential. A factor that limiting the discharge length of tandem mirror system is the maximum operation time length of magnetic coils and wave plasma heating system. Therefore, the system can be operated in steady state with reasonable technological effort. The world's largest tandem mirror device GAMMA 10/PDX [19](upgraded from GAMMA 10[20]) operated in the University of Tsukuba is feasible to the divertor simulation research since its end-loss particle flux of the machine is capable of achieving plasma temperature relevant to the boundary plasma in the fusion reactor. Also it should be noted that the end-loss particles in a tandem mirror has a distribution in energy space so as the fusion divertor plasma. From the result of previous works in the tandem mirror research, it was found that the end-loss ion flux has temperature of 400 eV and particle flux of $5 \times 10^{22} \text{ m}^{-2} \text{ s}^{-1}$. In the tokamak type fusion machine like ITER or DEMO [21], expected value of ion particle flux in divertor region is $10^{23} \sim 10^{25} \text{ m}^{-2} \text{ s}^{-1}$. Therefore for the better simulation of divertor plasma physics, the end-loss ion flux must be enhanced by 1~2 orders. Also, detailed analysis of the end-loss ion flux, especially from the view point of divertor simulation study must be performed.

In order to utilize the tandem mirror for divertor simulation studies in high plasma temperature range, analysis of the end-loss flux from the view point of divertor simulation study must be performed. The objectives of this research are to investigate the basic characteristics, to analyze the energy controllability and to enhance of the particle flux of the end-loss ion flux in the tandem mirror. Since the machine have an advantage of high ion temperature as a divertor simulator, this research focus on the ion energy and the controllability of the ion temperature. In addition, the production of more intense end-loss particle flux by the tandem mirror machine will be studied. First, the ion temperature and the particle flux of the end-loss ion flux are investigated. Then, several experiments were performed in order to find an operation mode that enhances the end-loss ion flux. Fueling of an additional gas, superimposing of an additional wave heating and direct injection of an additional plasma particle are tested. It was found that the superimposing of an additional ion cyclotron range of frequency (ICRF) heating to the anchor-cell of the tandem mirror shows the best result of increasing the ion flux. In the high particle flux operation with the ICRF heating, it was found that the transport of plasma particles between the mirror cells is important to understand the production of the end-loss ion flux. In order to analyze the mechanism of the end-loss production, numerical code that taking the transport of plasma particles into account was developed. From the analysis by using the code, the transport of the plasma particles in the tandem mirror and the process of the end-loss flux production during

the anchor heating were studied.

This thesis reports the results of experimental and numerical analysis on the end-loss flux of GAMMA 10/PDX. Information of the GAMMA 10/PDX tandem mirror itself and its plasma heating, fueling and diagnostic will be introduced in chapter 2. Then, the analysis method of the end-loss flux in experiments of GAMMA 10/PDX will be explained in chapter 3. The experimental results of the end-loss ion flux obtained by the measurement will be shown in chapter 4. Results of the additional heating and fueling to the GAMMA 10/PDX plasma and their effect on the enhancement of the ion particle flux will be discussed in chapter 5. The analysis of the production of the end-loss ion flux in the tandem mirror by using the numerical code will be introduced in chapter 6. Finally, the results of this research will be summarized in chapter 7.

Chapter 2 Experimental Apparatus

In this chapter, details of the experimental device GAMMA 10/PDX [22, 23] are described.

2.1 GAMMA 10/ PDX Tandem Mirror

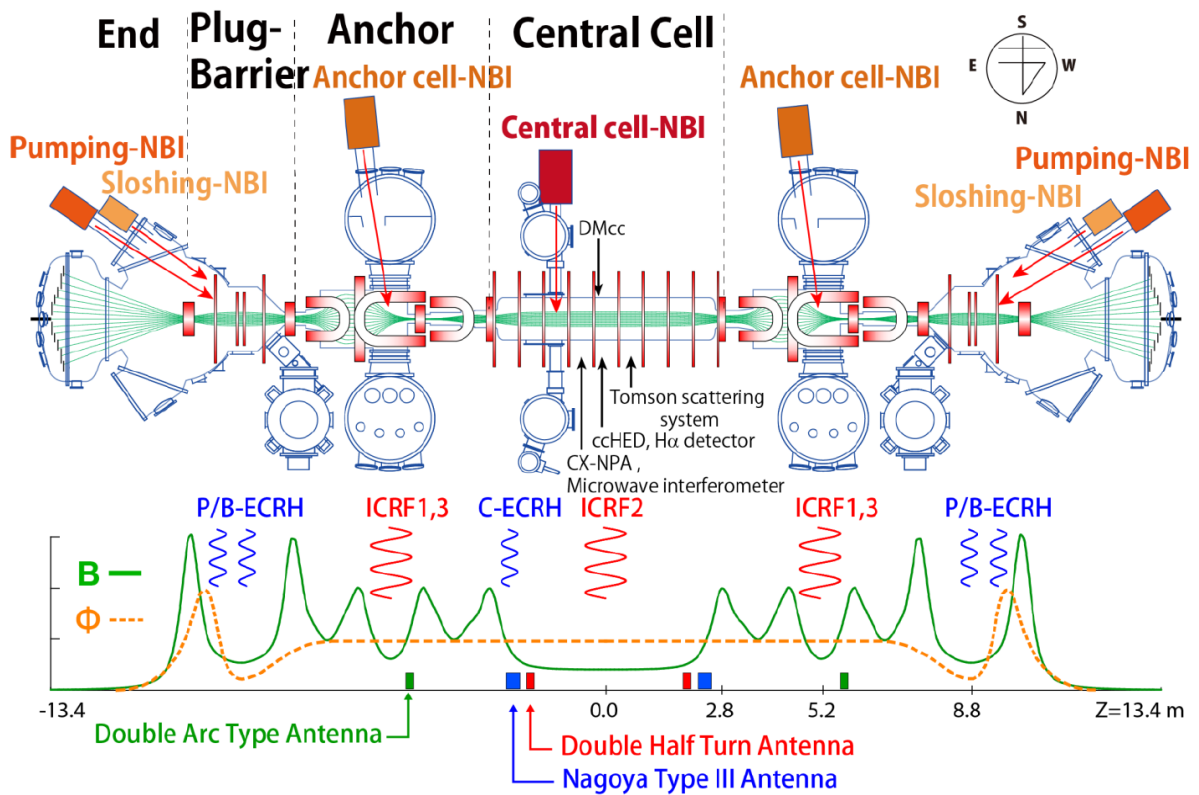


Fig. 2.1 Bird's eye view and axial profiles of magnetic field and electric potential in GAMMA 10/PDX tandem mirror.

GAMMA10/PDX has 27 m machine length and plasma radius larger than 10 cm at the center of the machine. As shown in Fig. 2.1, the tandem mirror consists of five cells of mirror confinement and two end regions along z axis; the central-cell, anchor-cells, plug/barrier-cells and end-cells. The central-cell is the main plasma confinement region located at the center of the machine. The anchor-cells are attached to the east and west sides of the central-cell and their main function is to stabilize the plasma in terms of MHD. The plug/barrier-cells are located so as to form the axial confining potential in the tandem mirror system. In the west end region, the divertor simulation study is performed by using the end-loss flux and divertor

simulation experimental module (D-module). The shape of the plasma generated in the machine is usually considered as cylindrical thus a Cartesian and a cylindrical coordinates are used for interpreting the geometry of the plasma. The z-axis is directed along the magnetic field line which heads to west. The x-axis directs vertically upward and the y-axis represents horizontal (north and south) direction in the Cartesian coordinates while these directions are defined as radial direction (r-axis) in the cylindrical system. The origins of both coordinates are set at the middle of the central-cell. In a standard operation of GAMMA 10/PDX, hydrogen plasma is started up by the ignition of plasma guns and heated up to ion temperature of several keV by high power ICRF heating systems [24]. With the electrical power supply system of the machine, the maximum discharge duration is limited to 400ms because of the heating up of magnetic coils and wave heating units.

2.2 Plasma Confinement in a Tandem Mirror

2.2.1 Plasma confinement by a Mirror Magnetic Field

A magnetic mirror is the methods of plasma confinement by a magnetic field which is based on the physical theory of energy conservation and magnetic momentum conservation. When a charged particle with certain initial velocity enters the magnetic field, the particle is given Lorentz force whose direction is perpendicular to the initial velocity. As a result, the particle starts rotating and around the magnetic field line and such motion of the charged particle is called gyro motion. Suppose that the strength of the magnetic field is kept constant in time and space, the motion of particle is only decided by the Lorentz force. On the other hand, if the magnetic field changes its strength in space, the particle will feel the force toward the direction of weaker magnetic field strength and the force is the cause of the mirror confinement. The mathematical expression for the confinement theory is following. The Larmor radius r of the gyro motion of the particle inside the mirror magnetic field can be written as equation (2-2-1).

$$r = \frac{mv_{\perp}}{qB} \quad , \quad (2-2-1)$$

m : mass of the particle v_{\perp} : velocity perpendicular to the magnetic field
 q : electrical charge B : magnetic field strength

The magnetic momentum μ is the product of the electrical current I and the area of circular motion S .

$$\mu = I \times S = \frac{mv_{\perp}^2}{2B} \quad (2-2-2)$$

The total kinetic energy of the particle ϵ is written as

$$\varepsilon = \frac{1}{2} m (v_{\perp}^2 + v_{\parallel}^2) \quad , \quad (2-2-3)$$

where

v_{\parallel} : velocity parallel to the magnetic field

The magnetic momentum μ and the kinetic energy ε are both conservative and therefore they will always be constant. Suppose that the particle is traveling from the position of smaller B to larger B . In that case, v_{\perp} must increase in order to keep μ constant. Then, according to the conservation law of ε , v_{\parallel} must decrease as v_{\perp} increases. When B become strong enough, v_{\parallel} will become zero and the particle will start moving back to the direction of smaller B as if it is reflected by a mirror. A mirror machine is making the use of that reflection of particle by magnetic field however; plasma confinement by mirror magnetic field is not perfect in an actual device. In example, if given the minimum strength of the magnetic field at the middle of the mirror magnetic field B_0 , the strength of magnetic field at the point of particle's reflection as B_{ref} , conservation of the particle's magnetic momentum is written as the following equation:

$$\mu = \frac{mv_{\perp 0}^2}{2B_0} = \frac{mv_{\perp \text{ref}}^2}{2B_{\text{ref}}} \quad , \quad (2-2-4)$$

where

$v_{\perp 0}$: velocity perpendicular to the magnetic field at B_0

$v_{\perp \text{ref}}$: velocity perpendicular to the magnetic field at B_{ref}

Also, from the conservation law of kinetic energy is written as:

$$\varepsilon = \frac{1}{2} mv_{\perp \text{ref}}^2 = \frac{1}{2} m (v_{\perp 0}^2 + v_{\parallel 0}^2) = \frac{1}{2} mv_0^2 \quad , \quad (2-2-5)$$

where

$v_{\parallel 0}$: velocity parallel the magnetic field at B_0

Note that v_{\parallel} is zero at the point of B_{ref} . Then, from (2-2-4) and (2-2-5), the following can be obtained.

$$\frac{B_0}{B_{\text{ref}}} = \frac{v_{\perp 0}^2}{v_{\perp \text{ref}}^2} = \frac{v_{\perp 0}^2}{v_0^2} \equiv \sin^2 \theta \quad (2-2-6)$$

In (2-2-6), θ represents the Pitch-angle of the charged particle with respect to the mirror magnetic field. Here, suppose that the maximum strength of the mirror magnetic field is limited B_{max} , the θ of the particle determines whether the particle can be reflected by the mirror or not. If the particle has too small θ , v_{\parallel} will

not be zero at B_{\max} and the particle will escape from the mirror. The minimum Pitch angle θ_m of the particle that can be confined by the mirror is defined as below:

$$\frac{B_0}{B_{\max}} = \sin^2 \theta_m = \frac{1}{R_m} \quad (2-2-7)$$

In a study of plasma confinement by a mirror magnetic field, the value R_m which is called mirror ratio is used to characterize the mirror system. In the velocity space, the regions of particle with its Pitch angle smaller than θ_m have the shape of cones. Therefore the region is called as loss cones. The axial particle loss from the loss cones is called the end-loss of the mirror confined plasma.

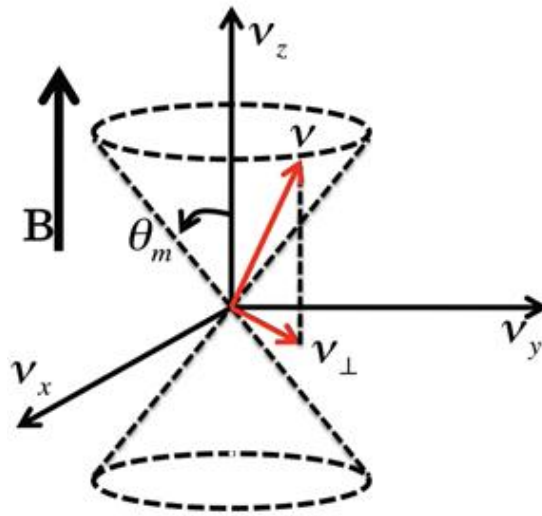


Fig. 2.2 Diagram of loss cones of mirror plasma confinement

2.2.2 Plasma Confinement by Electrostatic Potential

As stated in the last section, the mirror magnetic field cannot confine the particles in the loss cones. Then, to improve the plasma confinement, electrostatic confinement potential is used in a tandem mirror. If the value of the electrostatic potential along the mirror axis is given as the function $\phi(z)$ and the function satisfies ($\phi_{\text{ref}} > \phi_0$) while ϕ_0 is the potential at the center of the mirror and ϕ_{ref} is the potential at the point of reflection. Then, the equation (2-2-5) can be rewritten as:

$$\frac{1}{2} m v_{\perp \text{ref}}^2 + q \phi_{\text{ref}} = \frac{1}{2} m (v_{\perp 0}^2 + v_{\parallel 0}^2) + q \phi_0 \quad (2-2-8)$$

By (2-2-8) and (2-2-7) with $\phi_{\text{ref}} - \phi_0 = \phi_c$, the equation becomes:

$$\frac{1}{2}mv_{//0}^2 = \frac{1}{2}m(v_{\perp\text{ref}}^2 - v_{//0}^2) + q\phi_c = -\frac{1}{2}mv_{//0}^2(1 - R_m) + q\phi_c \quad ,$$

$$\frac{1}{2}m(v_0^2 - v_{\perp 0}^2 R_m) = q\phi_c \quad ,$$

$$\frac{1}{2}mR_m \sin^2 \theta = \frac{m}{2} - \frac{q\phi_c}{v_0^2} \quad ,$$

Therefore:

$$\sin^2 \theta = \frac{1}{R_m} \left(1 - \frac{2q\Phi_c}{mv_0^2} \right). \quad (2-2-9)$$

The equation (2-2-9) means that the regions of loss cones become narrower and thus the plasma confinement is improved by the confinement potential. In GAMMA 10/PDX tandem mirror, the plasma confinement potential is formed in the plug/barrier-cell to confine the plasma in the central-cell and anchor-cells.

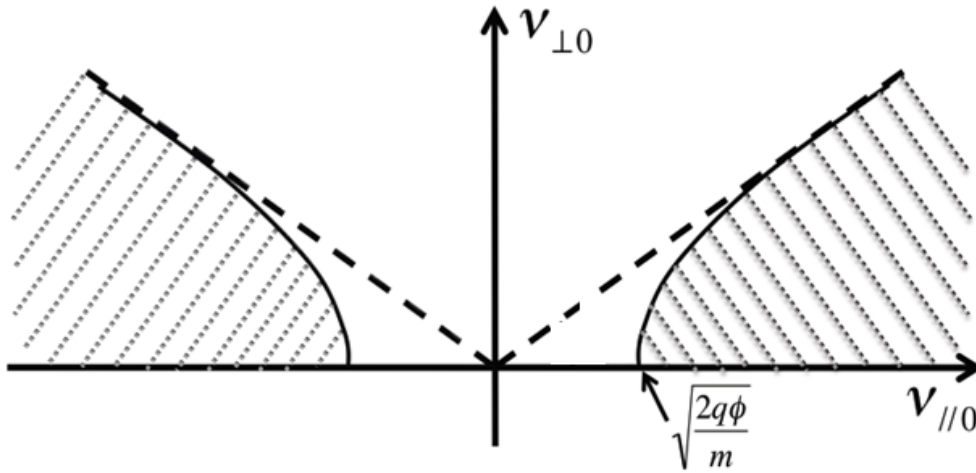


Fig. 2.3 Loss cones with plasma confinement potential

2.3 Specifications of GAMMA 10/PDX Mirror Cells

2.3.1 *Central-Cell*

The central-cell is the main plasma confinement region placed at the center of the tandem mirror. The cell have the axially symmetric magnetic mirror with mirror ratio of 5 ($B_{\max} = 2$ Tesla at the mirror throats and $B_0 = 0.4$ Tesla at the middle of the mirror field).The axial distance between the mirror throats is 5.8m.

2.3.2 *Anchor-Cell*

The east anchor-cell and the west anchor-cell are placed at eastern and western end of the central-cell. The anchor cells have the function of plasma confinement and stabilization by their magnetic field geometry which is called minimum-B configurations. The minimum-B configuration of the magnetic field is generated by specially designed magnetic coils such as baseball-coils or in-yang-coils and the configuration contribute to the stabilization of plasma in a tandem mirror. If a minimum-B configuration is not applied to the mirror machine, strong magneto hydro dynamic (MHD) instability will be induced and the plasma will collapse. In GAMMA 10/PDX, the mirror ratio of the anchor mirror is 3.3 with $B_{\max} = 2$ Tesla and $B_0 = 0.61$ Tesla.

2.3.3 *Plug/Barrier-Cell*

The east plug/barrier-cell and the west plug/barrier-cell are placed next to the anchor-cells. The configuration of the magnetic field in plug/barrier-cell is simple mirror field with its mirror ratio 6 ($B_{\max} = 3$ Tesla, $B_0 = 0.5$ Tesla). In the plug/barrier-cell, strong electron heating by electron cyclotron resonance heating (ECRH) is applied in order to form the plasma confinement potentials.

2.3.4 *End-Cell*

The end regions are located at the most outer end of the tandem mirror and the length of the region is about 3.4 m. As usually called as open ended system, no external magnetic field is applied to the region and therefore, the magnetic field lines are freely crossing the wall of vacuum vessel. During the plasma operation of the tandem mirror, a large amount of plasma particles enters to the region as the end-loss flux. Thus the region is required to have strong evacuation system of particles and electrical insulation of its wall. In GAMMA 10/PDX, large helium Cryopump and electrically floated end-plate are installed for the evacuation of particles and for the insulation of the wall respectively. For the diagnostic of the end-loss particle flux, the end-loss ion energy analyzer (ELIEA) and the loss electron diagnostic (LED) are installed at the back of the end-plate (Fig. 2.4).

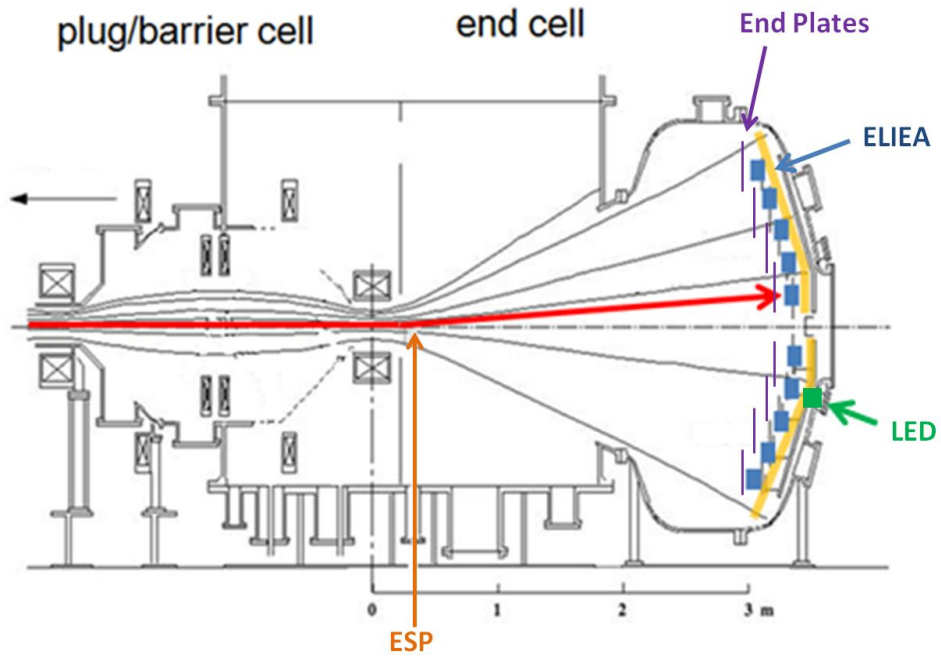


Fig. 2.4 West end-cell of GAMMA 10/PDX with ELIEA and LED devices

2.4 Plasma Heating and Fueling

2.4.1 Plasma Gun

In the experiment of GAMMA 10/PDX, seed plasma is generated by plasma guns [25] installed in the both end-cells in order to help the wave plasma heating systems in the initial phase of plasma operation. The plasma gun installed in GAMMA 10/PDX is called magneto plasma dynamic arcjet (MPD arcjet or MPD Jet) and the MPD Jet has co-axial anode and cathode as shown in Fig. 2.5. In a discharge of the MPD Jet, electric current of 6 kA flows between the anode and the cathode. Then, Lorentz force is induced within the current and magnetic field made by the current itself, and the Lorentz force thrusts ions and electrons into the direction of plasma flow. The injected plasma in each cells is used as the seed plasma of GAMMA 10/PDX.

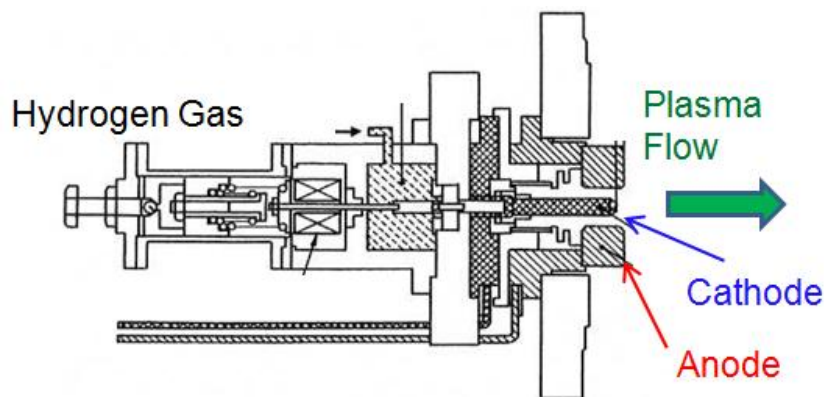


Fig. 2.5 Diagram of the MPD Jet.

2.4.2 *Ion Cyclotron Range of Frequency Heating*

The ion cyclotron range of frequency (ICRF) heating with 100~300 kW power is the main plasma heating of GAMMA 10/PDX. The radio waves excited by the ICRF system [24] have the wave frequency match the frequency of ion cyclotron motion in order to heat the ions. In GAMMA 10/PDX, three different types of antennas are installed. Two of the three types are installed at both ends of the central cell: one is the Nagoya type III antenna and the antenna is used for the production of plasma in the anchor region (ICRF1). The other is the double half turn (DHT) antenna mainly used to heat the ions in the central-cell (ICRF2). The third type of the antenna in GAMMA 10/PDX is called double arc type (DAT) antennas and the antennas are designed to heat the plasma in anchor regions (ICRF3). The Frequencies of the waves in each antenna are: 9.9 and 10.3 MHz in Nagoya type III, 6.36 MHz in the DHT antennas and 9.9 and 10.3 for DAT antennas [26].

2.4.3 *Electron Cyclotron Resonance Heating*

Five units of the electron cyclotron resonance heating (ECRH [27]) are installed in GAMMA 10/PDX: one in the central-cell and four in the east and west plug/barrier-cells. In ECRH, the micro wave with wave frequency corresponds to the cyclotron frequency of the electron is launched from Gyrotrons. The ECRH in the central-cell is used to increase the electron temperature while the ECRH in the plug/barrier-cells are used to form confinement potentials.

2.4.4 *Neutral Beam Injection*

The neutral beam injection is the method of plasma heating by injecting the high energy beam of hydrogen atoms. As the beam is injected, the collision of atoms and the plasma will happen and the energy of the beam is transferred to the plasma by charge exchange reactions. In GAMMA 10/PDX, seven units of neutral beam injection (NBI) are installed [28]: central-NBI, anchor-NBI, sloshing-NBI and pumping-NBI. The central-NBI is located at the central-cell and it heats the central-cell plasma. In both east and west anchor-cells, the unit of anchor-NBI is installed to improve the plasma parameters in the anchor-cells. The sloshing-NBI and the pumping-NBI are installed at both east and west plug/barrier-cells and these NBI systems are mainly used to modify the distribution of ions in the cell and to help the formation of confinement potentials.

2.4.5 *Gas Puffs*

The gas puffing systems with piezoelectric valves are installed in GAMMA 10/PDX to supply hydrogen gases into the chamber. The injection of gas can be controlled by changing the starting time, pulse length and the pressure of the gas reservoir tank. Due to the large size of the tandem mirror machine, many ports of gas puff are installed and these ports are distinguished by numbers (and alphabets) such as gas puff #3 or #4. The location of each gas port in GAMMA 10/PDX is shown in Fig. 2.5.

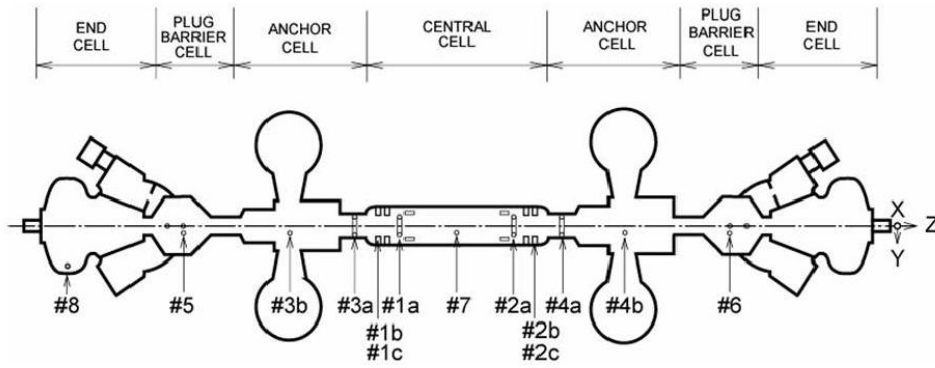


Fig. 2.6 Port locations of Gas Puff injection in GAMMA 10/PDX.

2.4.6 Supersonic Molecular Beam Injection

In order to supply gas molecules to the core region of the plasma, supersonic molecular beam injection (SMBI [29, 30]) is installed in the central-cell. In SMBI, pressure of the gas injection is much higher than that in gas puffing. As a result, the initial velocity of the molecules after the injection become larger than the sound speed and more molecules can reach the core of the plasma.

2.5 Plasma Diagnostics

2.5.1 Microwave Interferometers

When a microwave is penetrating the plasma, the phase of the microwave is changed due to the interference from the electrons in the plasma [31]. Therefore, by investigating the change of the phase of microwaves, the line integrated density of electron can be known. In GAMMA 10/PDX, the microwave interferometers are installed in each cell to measure the line integrated densities.

2.5.2 Diamagnetic Loop

The diamagnetic loop measures the diamagnetism of the plasma. Plasma is a diamagnetic material in a magnetic field since the cyclotron motion of plasma particles is directed to the direction of cancelling the magnetic field out. The strength of the diamagnetism can be a measure of the energy stored in the plasma because the diamagnetism depends on the plasma pressure P . Suppose the plasma have ion temperature T_i , electron temperature T_e , ion density n_i , electron density n_e and assuming $n_i = n_e$, the following relation is given.

$$P \propto \int n_e (T_i + T_e) dS \quad (2-4-1)$$

Here, $\int dS$ means the integration over the cross sectional area of the plasma. Since the n_e can be known from the measurement by the microwave interferometers, the change of the diamagnetism measured by the loop can be used as the indicator of plasma temperatures. In GAMMA 10/PDX, three diamagnetic loops are installed in the central-cell [32].

2.5.3 Neutral Particle Analyzer

The neutral particle analyzer (NPA [33, 34]) is installed in the perpendicular port of the central-cell of GAMMA 10/PDX in order to analyze the ion energy in the central-cell. In the mirror magnetic field, plasma particles have two components of velocities: v_{\perp} and v_{\parallel} . If a charge exchange between the plasma ion and the gas neutral atom happens in the plasma, the ion will loss from the plasma as neutral particle with possessing the same energy as plasma ions. The NPA collects the neutral particles loss from the plasma and in the chamber of the NPA, the neutral particles are re-ionized. Then, deflection voltage is applied to the re-ionized ions so as to resolve their energy distribution.

2.5.4 Thomson Scattering System

The Thomson laser scattering system of yttrium-aluminum-garnet (YAG) laser is installed in the central-cell and used to measure the electron temperature and the electron density of the central-cell plasma [35]. The laser is incident to the plasma at $z = 60\text{cm}$ in the central-cell and the scattered light of the laser is investigated to obtain the electron temperature and density.

2.5.5 Directional Mach Probe

The directive mach probe measures the mach number of ion in the flowing plasma. The mach probe consists of four electrostatic probes that direct east, west, north and south. The mach probe is placed at the west end region ($z = 1030\text{ cm}$) and at that position, the probe investigate the plasma flow of the end-loss flux along z-axis and y-axis of the tandem mirror [36]. Also, four electrostatic probes can be used as normal electrostatic probes (ESP) to measure the electron density, electron temperature and ion saturation current.

2.5.6 Calorimeter

The calorie meter is a measurement device to evaluate the total heat flux of the plasma. The device consists of the front tip metal and thermocouples. When the plasma hits the front tip, some heat energy from the plasma is transferred to the tip and the energy is detected as the change of temperature by the thermocouples. In GAMMA 10/PDX, the calorie meter is installed at the west end region and measuring the heat flux of the

end-loss flux [37].

2.5.7 *High Speed and Middle Speed Cameras*

In GAMMA 10/PDX, the high speed camera with 1000~40000 fps and the middle speed camera with 400~1000 fps are used to observe the time behavior of the plasma [38, 39]. The high speed camera is located at the central-cell and the west end region in order to investigate the behavior of core plasma and D-module plasma. In usual the cameras are measuring visible region of the light (400~800 nm), however, the measurement of specific light emission is also possible with an application of optical filters.

2.5.8 *End Plate*

The end plates are installed in the east and west end regions in order to insulate the plasma and the wall of the vacuum vessel. Basically the plates are insulated from the wall by the resistor of $1M\Omega$. In addition to their function of the insulation, the plates are also useful for the measurement of the plasma. That is, by measuring the floating potential of the plate during the plasma discharge, the total charge current of the end-loss flux can be known. In GAMMA 10/PDX, the end plates are divided into four sections in radial direction to investigate the difference of axial loss in different radial positions [40].

2.5.9 *Loss Electron Diagnostic*

The loss electron diagnostic (LED [41]) is the measurement device for the end-loss electrons. The devices are placed at both east and west end regions and they are investigating the current density and parallel energy component of the end-loss electrons. The structure of the LED is shown in Fig. 2.7. In the measurement of LED, high positive potential is applied to the ion repeller grid in order to reflect the ions in the end-loss flux. Then, negative sweep voltage is applied to the electron repeller and the electrons are resolved by its kinetic energy. Electrons passed the electron repeller grid are collected by the collector grid and the current density of the electrons is measured. By taking the V - I characteristic between the electron repeller voltage and the electron current density, temperature of the electron flux is evaluated.

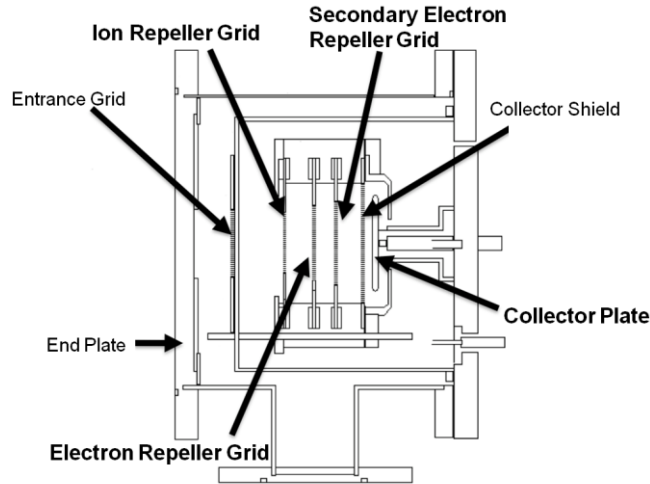


Fig. 2.7 Schematic diagram of LED

2.5.10 End-Loss ion Energy Analyzer

The end-loss ion energy analyzer is the device to measure the current density and the parallel ion energy of the end-loss flux [42, 43]. Figure 2.8 is the schematic diagram of the ELIEA device. The measurement of the ion flux by ELIEA is similar to the measurement of the electron flux by the LED device and the measurement is based on the $V-I$ characteristics between the ion repeller voltage and the ion current density. However in the case of ELIEA, the ion repeller grid is installed with angle of 42° with respect to the magnetic field and the collector plate is placed to face the ion repeller grid. Also the grounded ion energy controller grid with triangular structure exists between the ion repeller grid and the collector plate. The positions of the grids are designed in order to measure the ion current without the disturbance of high energy electrons produced by ECRH [44]. Since the collector plate is facing to the ion repeller grid, the plate collects the ions that were reflected by the ion repeller grid. Therefore the collected count of ions corresponds to the number of ions integrated from zero to the ion repeller potential in energy space. At the location that the ELIEA arrays are installed, strength of the magnetic field is very small (0.01 Tesla) in comparison with the strength in mirror cells. In such case, the perpendicular component of the particles' velocity become very small and therefore it can be assumed that the measurement of the parallel ion energy is equivalent to the measurement of total kinetic energy of the ion in the end-loss flux. In GAMMA 10/PDX, arrays of ELIEA devices are installed in order to measure the end-loss ions with different positions along x-axis and y-axis. There are ten ELIEA devices in the east end region and twenty devices in the west end region. The configuration of each arrays are shown in Fig. 2.9. In one array of ELIEA, the locations of devices in radial distance (converted to the distance in central-cell) are set as: ch.1=2.59cm, ch.2=5.26cm, ch.3=8.25cm, ch.4=11.19cm and ch.5=14.64cm. A detail of the ELIEA measurement is stated in Chapter 3.

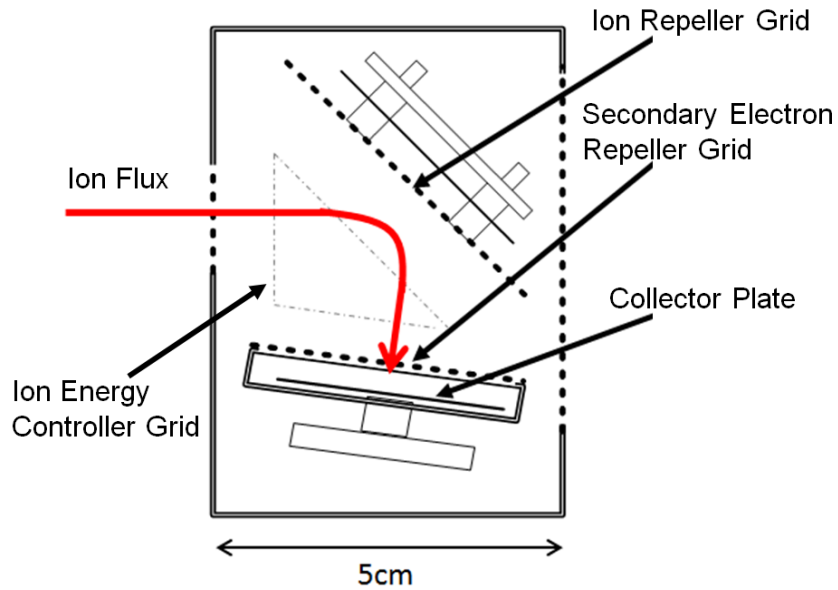


Fig. 2.8 Schematic diagram of ELIEA device.

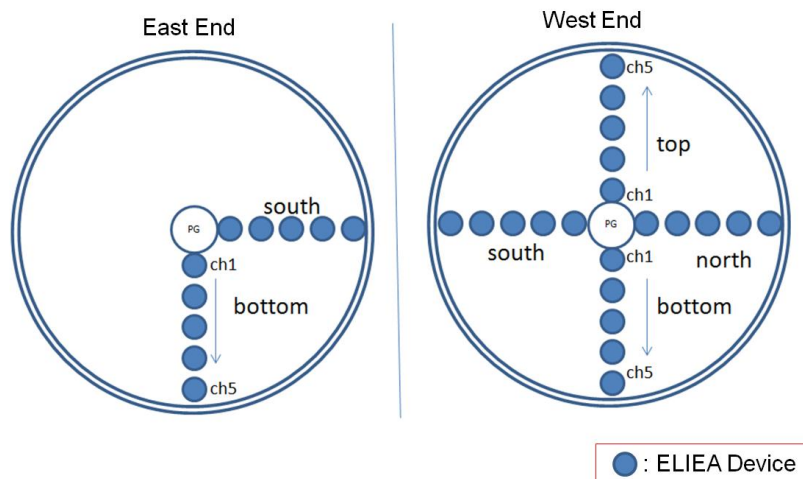


Fig. 2.9 Radial positions of ELIEA devices in east and west end cells.

2.6 Divertor Simulation Experimental Module

The divertor experimental simulation module (D-module [45, 46]), which consists of V-shaped tungsten target surrounded with semi-closed box of SUS equipped with gas injection ports, Langmuir probes, thermocouples and optical measurement systems, has been installed in the west end region of the tandem mirror. In the D-module, the experiments which experimentally simulating the situation in a divertor region of fusion reactor are performed. In example, interactions of the high temperature plasma particle and room temperature tungsten target together with the impurity gas are studied.

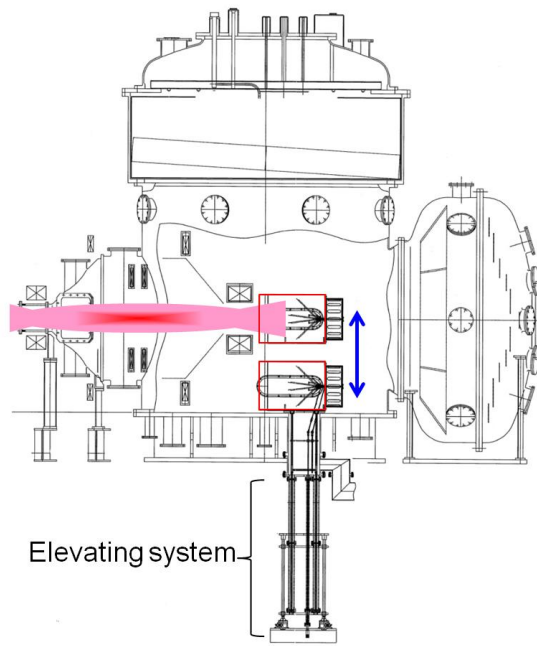


Fig. 2.10 Side view of the D-module and the west end-cell.

Chapter 3

Method of the End-Loss Ion Flux Analysis

A brief explanation of the ELIEA device was made in the section 2.5.9. In this chapter, details of the ELIEA measurement and the methods of analysis of the end-loss ion current density and ion energy in GAMMA 10/PDX are described.

3.1 Measurement of the Ion Flux by ELIEA

In the operation of the ELIEA measurement, the sweep function of the ion repeller voltage (V_{IR}) of a triangle wave with its frequency of 250~750 Hz, amplitude of 1200~1800 V and the offset of +600~+900 V is applied. The time changes of the ion repeller voltage and the ion current detected by the collector plate are obtained by the data acquisition system called CAMAC. Then, with the data stored in the system, V - I characteristics of the end-loss ion flux was investigated. In order to evaluate the energy profile of the ion flux, the ion repeller voltage was converted to the energy by taking the angle of the ion repeller grid into account. The relationship between ion repelling energy E_{IR} and the applied voltage V_{IR} is obtained as follows,

$$E_{IR} = \frac{V_{IR}}{\cos^2(42^\circ)} \quad (3-1)$$

For evaluating the data of the ion current, the conversion is required in order to evaluate the actual ion current density along the magnetic field line instead of the ion current on the slanted collector plate. First, the area of the entrance aperture of the ELIEA device (0.46cm^2) is considered to obtain the current density. Then, the mechanical transparency of the grids in the ELIEA device is taken into account. Several grids of stainless steel mesh are installed in the ELIEA device in order to apply electrical potentials for the device and the number of ions reaching to the collector plate is decreased by the existence of meshes. In analysis of the ELIEA, the transparency of the grid is defined as the ration of the area not covered by the mesh wires to the total area of grid (see Fig. 3.1). In the ELIEA devices installed to GAMMA 10/PDX, the transparency rate is 0.13~0.18 and thus 13~18% of the ions passes through the meshes.

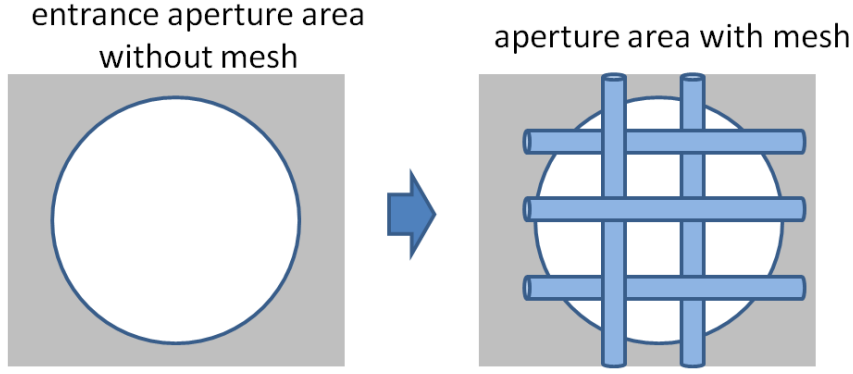


Fig. 3.1 Sketch of the change of aperture transparency change made by mesh wires.

3.2 Evaluation of the Ion Energy

Since the ion current density corresponds to the number of ions integrated over ion repeller energy, the following equation is obtained by assuming the energy distribution function of the ion flux as $f(E_{//})$,

$$I_{\text{ELIEA}} = \int_0^{E_{\text{IR}}} f(E_{//}) dE_{//} \quad (3-2)$$

Suppose that the energy distribution of the ions follow the Maxwellian distribution, Eq.(3-1) can be rewritten as below,

$$I_{\text{ELIEA}} = \int_0^{E_{\text{IR}}} A \exp\left(\frac{-E_{//}}{T_{i//}}}\right) dE_{//} \quad ,$$

(3-3)

A = arbitral constant.

In this case, the symbol $T_{i//}$ is the parallel temperature of the ion flux. Therefore the temperature can be evaluated by a fitting to the experimentally measured V - I characteristics with the model function of (3-3). However, in the measurement of the end-loss ion flux in tandem mirror plasma, the effect of ion acceleration by the space potential of mirror plasma must be considered. An electron of the mirror plasma escapes the mirror region much faster than ion and therefore the plasma is positively charged in the mirror field. As a result, potential difference between the mirror plasma and end wall is generated and the potential accelerates the ion flux. Suppose that the potential difference is given as ϕ the energy distribution of the ion is shifted by the potential and the equation (3-3) become as following,

$$I_{\text{ELIEA}} = \int_0^{E_{\text{IR}}} A \exp\left(\frac{-(E_{\parallel} - e\phi)}{T_{i\parallel}}\right) dE_{\parallel} \quad (3-4)$$

e = elementary charge.

In Fig. 3.2, a schematic image of the energy distribution of the ion shifted by the plasma potential is shown. When the measurement by ELIEA device was performed to the shifted energy distribution in Fig. 3.2, the resulting V - I characteristic become like the image in Fig. 3.3. As shown in Fig. 3.3, V - I characteristics is saturated in the region of high V_{IR} . In such region, the value of the ion current density is reflecting the total flux of the ion in the end-loss flux. Therefore the height of the V - I characteristics can be used as the measure of the on particle flux.

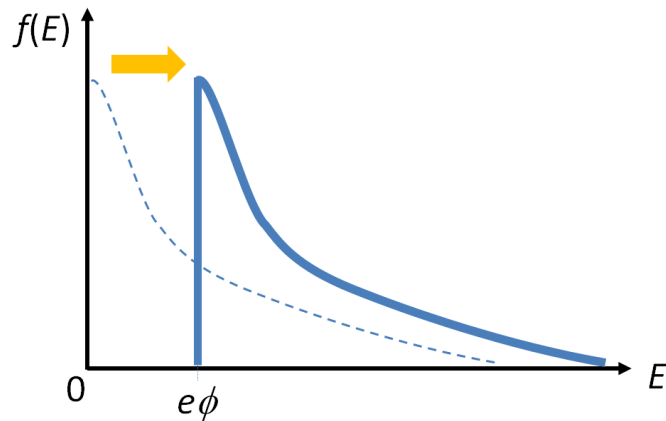


Fig. 3.2 Sketch of the ion energy distribution shifted by positive plasma potential.

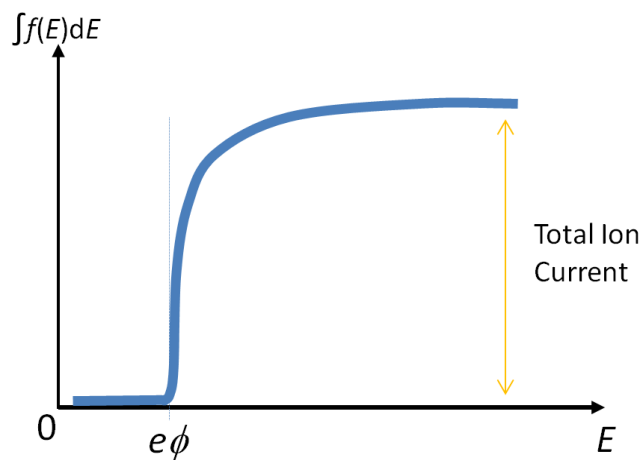


Fig. 3.3 Image of the ion energy distribution integrated in the measurement of ELIEA.

3.3 Evaluation of the Ion Particle Flux

In the end region of the tandem mirror, strength of the magnetic field changes largely (from 3 Tesla to 0.01 Tesla) and the magnetic flux tubes are expanded as they approaches to the end plates (Fig. 2.4). The ion current density measurement by ELIEA is performed at the region of $B= 0.01$ T, while the divertor simulation experiments are performed in the region around $B = 1.0$ T. Thus, in order to apply the ion current density measured by ELIEA to the divertor simulation experiments, calibrations with other diagnostics are required. The magnetic field strength at each position and the average parallel velocity of the ions at each position must be known to convert the value of ion particle flux at ELEE to the flux at D-module. However, in the case of GAMMA 10/PDX, the electrostatic probe can be used in front of the D-module and therefore the direct calibration of the ion flux is also possible. Thus, in this research, the ion particle flux was calibrated by directly comparing the ELIEA result with result of electrostatic probe installed at the entrance of D-module.

3.4 Evaluation of Measurement Errors

The first major cause of the measurement error of ELIEA is a fluctuation or perturbation of the plasma. Since the ELIEA measurement is based on the sweep voltage, change of the plasma condition faster than the sweep frequency (typically 500Hz) cause the error of the $V-I$ characteristics. With the plasma fluctuation, the error around 10% is typically expected for the detection of ion current density. Fitting to the $V-I$ characteristics also have error of the analysis. In this research, the fitting of the least square method was used and the typical error is about 5~15 %. For other causes, the back ground noises and the miss-synchronization of the data exist. Typically, background noise is about 1% of the signals and the miss-synchronization of one sample point will cause the error of 9 Volts (0.005% of maximum repeller voltage) in the signals of $V-I$. As a whole, the typical result of the ELIEA measurement is expected to include 10~30% of error.

Chapter 4 Analysis of the GAMMA 10/PDX

End-Loss Flux in Standard Experiments

In this chapter, results of the end-loss flux measurement in the standard plasma discharges of the GAMMA 10/PDX are introduced and discussed.

4.1 Time Behavior of Plasma Parameters in Standard ICRF-Heated Plasmas

In this research, the standard operation means the plasma discharge with plasma heating of ICRF Nagoya-type III (ICRF1) and DHT antennas(ICRF2) and fueling from several gas puffers; gas puff#1b, #2b, #3a and #4a. Therefore other additional input of power or particle, such as NBI, ECRH and SMBI are not applied. The characteristics of the end-loss flux are investigated by changing the power of ICRF heating and the amount of gas puffing. The typical behavior of the standard plasma is shown in Fig. 4.1.

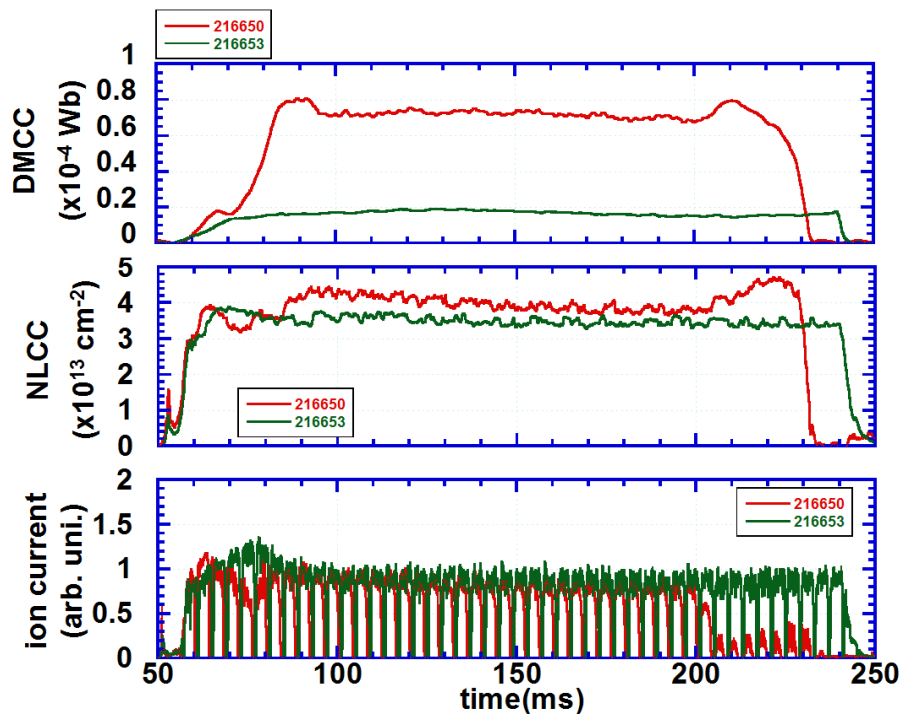


Fig. 4.1 Diamagnetism in the central-cell, electron line integrated density in the central-cell, and the ion current density detected by the ELIEA at west end-cell in high power and low power operations of standard mode.

4.2 V - I Characteristics and Ion Energy Distribution in Standard Operations

In order to analyze the characteristics of the end-loss ion flux in the standard operation of GAMMA 10/PDX, two plasma discharge shots are examined. One is the shot number #216650 and the other is the shot number #216653. In #216650, the power of ICRF heating is 140 kW and the injection plenum pressure of the gas-puff #3 and gas-puff #4 are set to be 60 Torr. On the other hand, the power of ICRF heating is 48 kW and the injection plenum pressure of the gas-puff #3 and gas-puff #4 are set to be 80 Torr in #216653. As a result, diamagnetism in the central-cell plasma (DMCC) of #216650 is much higher than that of #216653 as seen in Fig. 4.1 and therefore it is expected that the plasma temperature in #216650 is higher than #216653. Other plasma parameters such as electron line density in the central-cell (NLCC) and the end-loss ion current density show no large differences over the time range of 100~200ms. The result of the ELIEA measurement (west, top, ch.1) in both plasma shots are investigated and the obtained V - I characteristics are plotted in Fig. 4.2. Next, smoothing for the V - I curves was applied by using the exponential moving average method and then, energy spectrum of the end-loss ion flux has been achieved by taking a differentiation between each sample points of the smoothed curve. The obtained energy spectrums are shown in Fig. 4.3. As expected, both V - I curves and the energy spectrum curves are shifted toward higher energy region due to the acceleration from the plasma potential. In the following fitting analysis, ions with energy lower than the shift of the curves are excluded from the fitting.

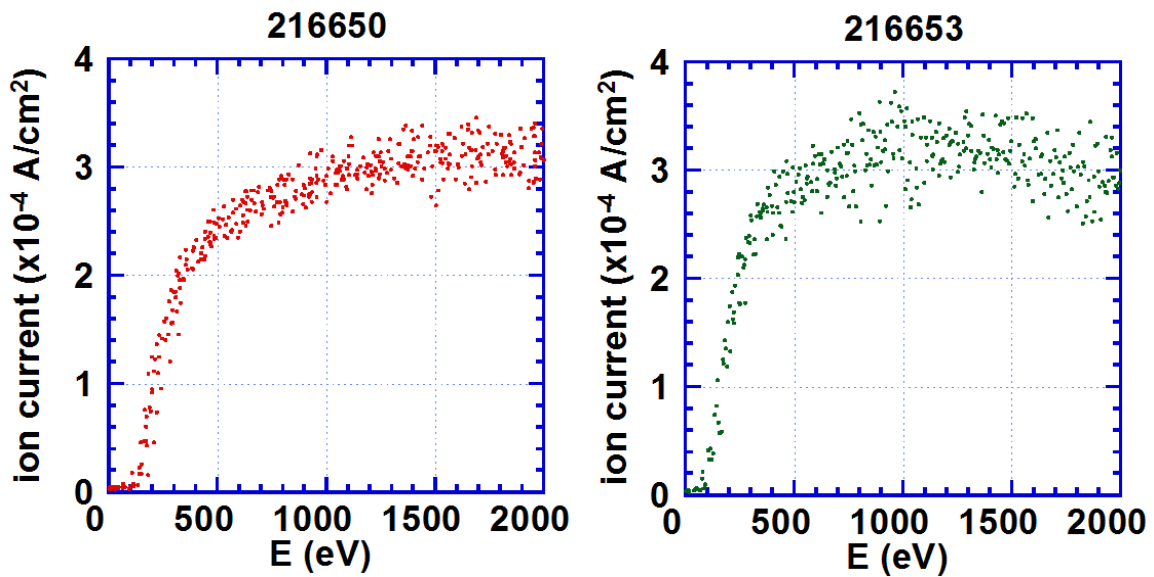


Fig. 4.2 V - I characteristics measured by ELIEA.

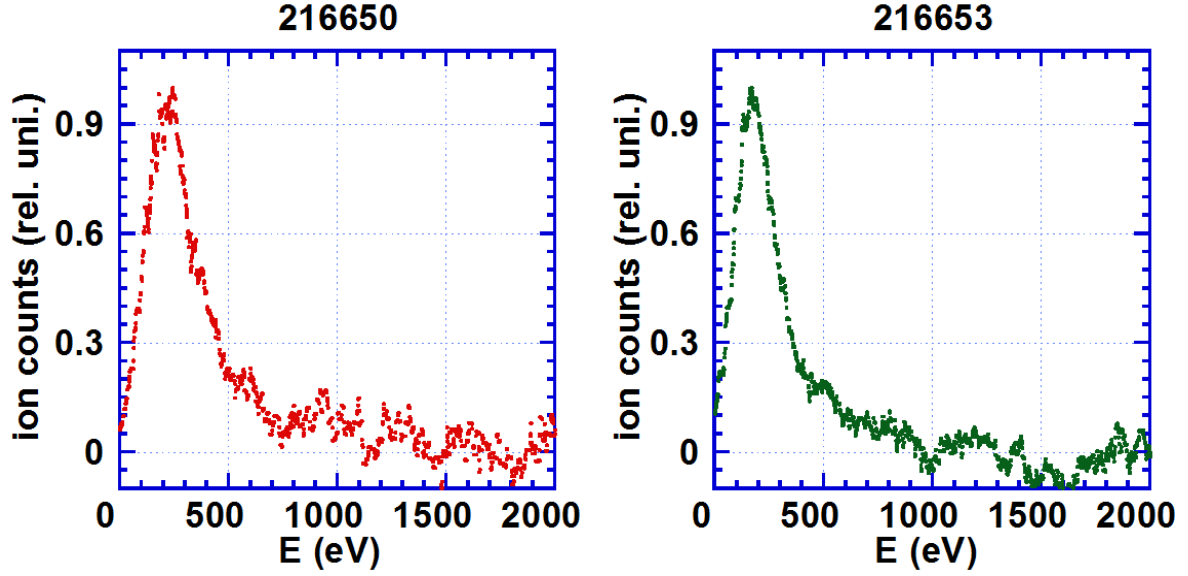


Fig. 4.3 Energy spectrum of the ion flux obtained from the V - I characteristics.

4.3 Energy Analysis on the Standard End-Loss Ion Flux

4.3.1 Energy Analysis by Single-Component Maxwellian Model

In order to evaluate the parallel ion temperature of the lower power discharge (#216653), fitting analysis by the least-square method was performed with the model function of the following shifted-Maxwellian curve as follows

$$f(E_{//}) = A \exp \left\{ - \frac{(E_{//} - e\Phi)}{T_{i//}} \right\}. \quad (4-1)$$

The result of the fitting analysis for #216653 is shown in Fig. 4.4(a). In this case, the parallel ion temperature of the ion flux was evaluated as 173eV with the fitting error of ± 4 eV and the plasma potential evaluated from the spectrum ($\phi_{\text{spec.}}$) is 190 V. The parallel ion temperature evaluated from the fitting in the integrated curve is 161 ± 7 eV and the plasma potential evaluated from the integrated curve (ϕ_{integral}) is 91.1 V as shown in Fig. 4.4(b). With considering the error of the energy spectrum due to the smoothing, it can be said that those two results of ion temperature evaluation are corresponding. The difference of these two fitting is the existence of ions with energy lower than $e\phi_{\text{spec.}}$. Since the value of $\phi_{\text{spec.}}$ is closer to the core plasma potential measured in the central-cell, low energy ions are assumed to be come from the collision of particles in boundary region of the mirror and the ionization of neutral particles exists between the mirror region and the end-region. In the fitting for the energy spectrum curve, ions in the region of $E < (e\phi_{\text{spec.}})$ are not included to the fitting. However, as shown in Fig. 4.4(b), these low energy ions occupy nearly 30% of the total ion

current and they can affect the result of fitting analysis. Suppose that the ions of $E < (e\phi_{\text{spec}})$ are not thermalized, these low energy ions will make a step structure or a hump structure of the $V-I$ curve and such structure will cause large error for the fitting analysis. However, as seen in Fig. 4.4(b) and Fig. 4.5, the $V-I$ curve does not show these characteristics and the amount of non-thermalized ions are as small as background noise. It means that most part of low energy ions is thermalized and the error of fitting analysis due to the low energy ions is small. In addition, the non-thermalized ions are excluded from the fitting analysis since their energy is apparently smaller than the shift of $V-I$ curves as stated in the section 4.2. Therefore the fitting for $V-I$ curve is sufficiently reliable as long as a hump or a step structure are not seen in the curve.

Figure 4.6 (a) shows the $V-I$ characteristic contains relatively large amount of non-thermalized ions. With removal of the low energy ions, the ion temperature of the thermalized ions can be evaluated. In addition, since the non-thermal part of ions show linear slope in the $V-I$ curve, it can be assumed that the non-thermalized ions are distributed in the energy space as shown in Fig. 4.6 (b). In that case, the average energy of the non-thermal ions can be evaluated as $0.5 \times \phi_{\text{integral}}$ eV. In this thesis, the fitting analysis for $V-I$ curves is used to evaluate the value of ion temperatures.

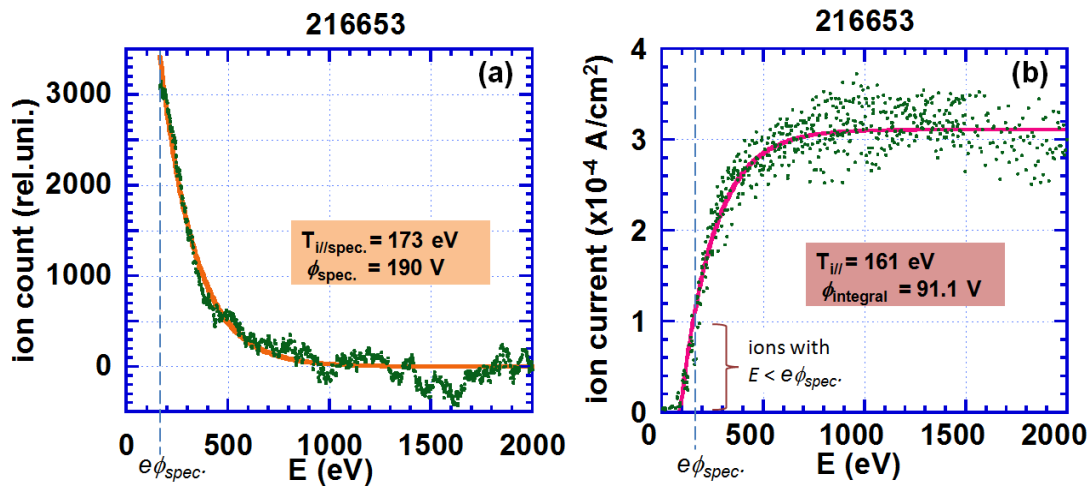


Fig. 4.4 Energy spectrum and Maxwellian fitting curve for $V-I$ curve in the ion flux in lower power discharge.

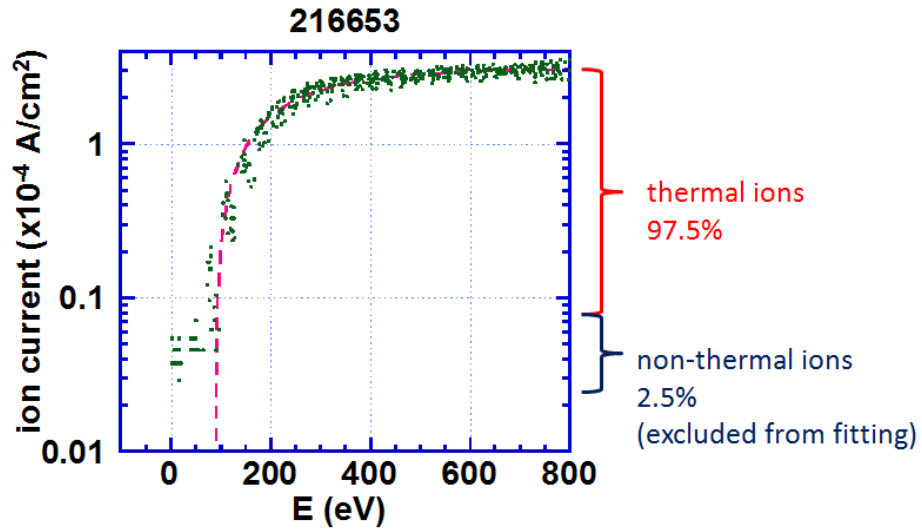


Fig. 4.5 V - I characteristics of the lower energy discharge plotted in the semi-logarithmic form.

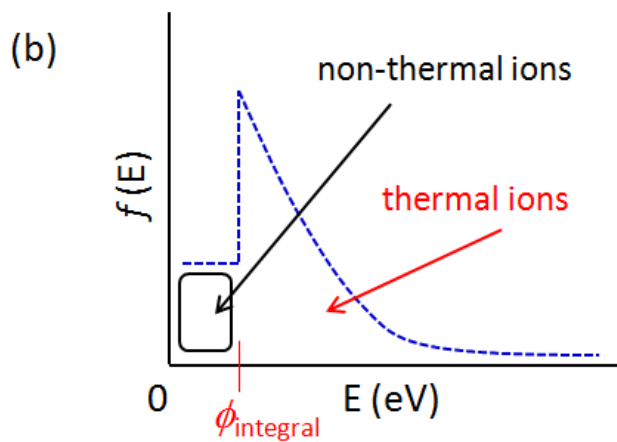
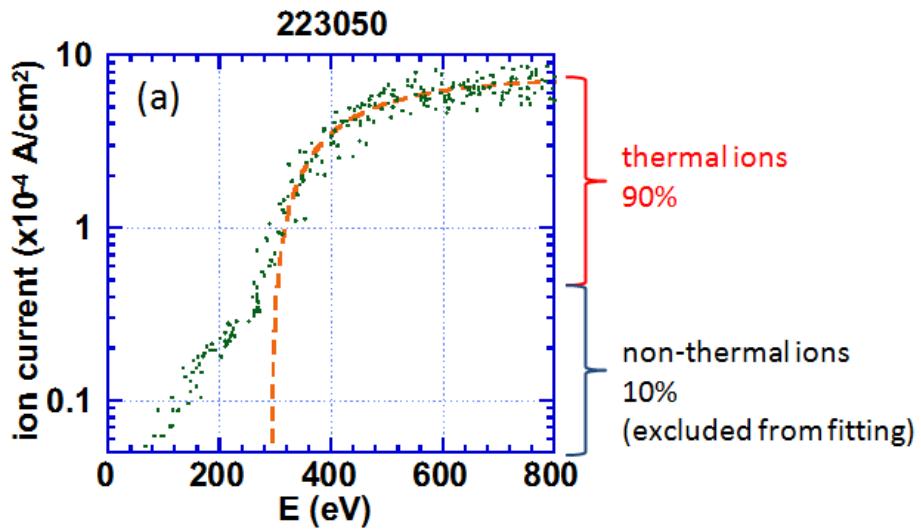


Fig. 4.6 (a): V - I characteristics with higher amount of non-thermal ions. (b): schematic diagram of the energy distribution corresponds to the V - I curve of (a).

4.3.2 Energy Analysis by Double-Components Maxwellian Model

The results of fitting analysis for higher power plasma (#216650) are shown in Figs. 4.7(a) and (b). In higher energy plasma experiment, the fitting analysis to the V - I profile show a disagreement of the curve at high energy region. In this case, behavior of the ions in high energy region is assumed to be important for the analysis of the ion temperature. Figure 4.8 shows the plot of energy spectrums plotted against the semi-logarithm scale axis. If the energy distribution of the end-loss ion flux completely follows the Maxwellian distribution, the energy spectrum in Fig. 4.7 is thought to be a straight decaying line. As seen in the figures, plots in high energy (around 1000 eV) region are not in the linear line of the semi-logarithm scale and there could be a tail-component in the energy spectrum. However, the high energy region of the spectrum has large ambiguity and not suits for a fitting analysis. During the process of achieving the spectrum from a V - I profile, derivatives between data points are calculated and therefore a small errors in the data points of V - I curve are strongly enhanced. Then large fluctuations are made on the high energy region of the profiles.

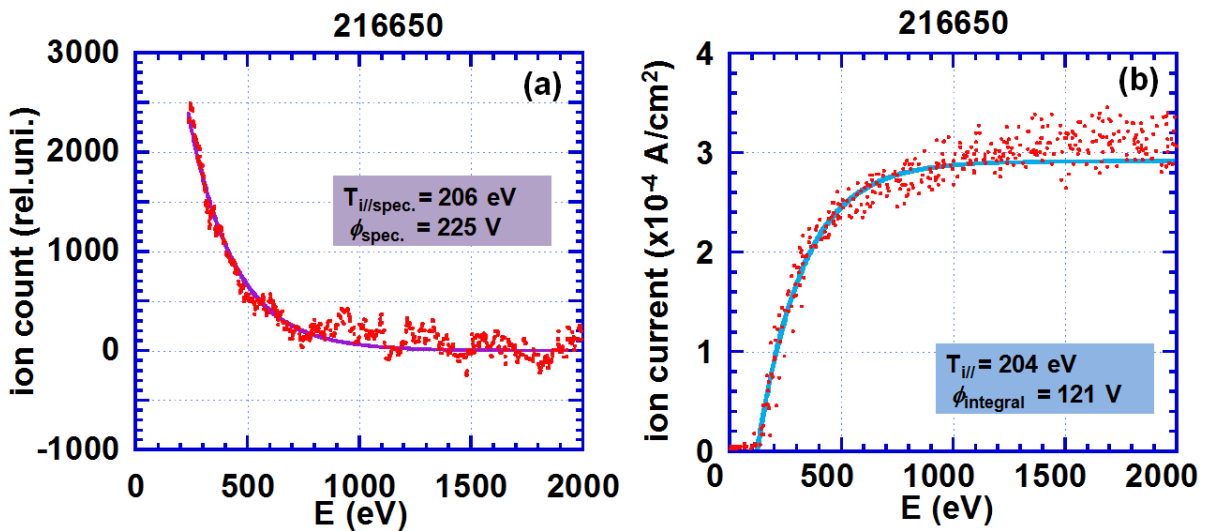


Fig. 4.7 Energy spectrum and Maxwellian fitting curve for the ion flux in higher power discharge.

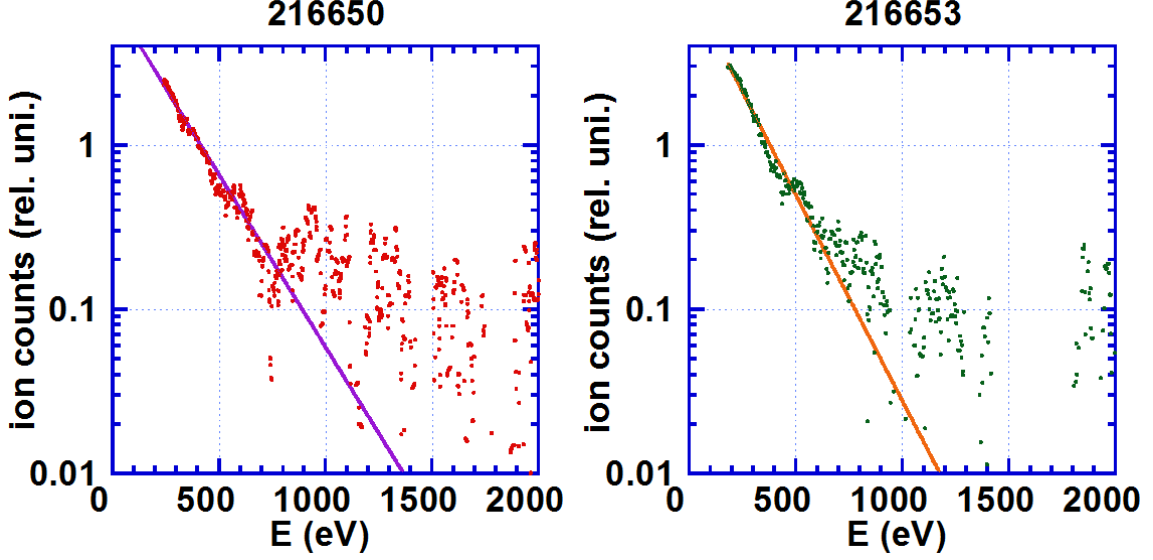


Fig. 4.8 Energy spectrums and the fitting curves of the ion flux plotted in semi-logarithm scale.

Assuming that the tail-component exists in the high energy region, fittings for the V - I curve were performed. In the fitting analysis, the double-components of the ion current are represented as low temperature and high temperature component as in the following equation,

$$I_{\text{ELIEA}} = \int f(E)dE = A \left[\beta \times \exp \left\{ -\frac{(E_{//} - e\Phi)}{T_{\text{low}}} \right\} + (1 - \beta) \times \exp \left\{ -\frac{(E_{//} - e\Phi)}{T_{\text{high}}} \right\} \right] \quad (4-2)$$

In this case, the effective parallel ion temperature is evaluated by the values of temperature and the ratio of each component in the total ion current.

$$T_{i//}^{\text{eff}} = \beta \times T_{\text{high}} + (1 - \beta) \times T_{\text{low}}, \quad (4-3)$$

$$\beta = \frac{I_{\text{low}}}{(I_{\text{low}} + I_{\text{high}})}. \quad (4-4)$$

Results of the fitting analysis with double-components for the V - I curves are plotted in Fig. 4.8. The double-components fitting for the higher power plasma shot indicate that the tail-component of the energy distribution has ion temperature of 807 eV as seen in Fig. 4.9(a). Suppose that the analysis with double-component is correct, the evaluation of the ion temperature is changed from 257 eV (single-component) to 361 eV (double-components). On the other hand, in lower power shot (Fig. 4.8(b)), the values of ion temperature in each component are very close to the ion temperature obtained in single-component fitting. Thus it can be assumed that the high temperature tail-component is only observed in high power plasma shots.

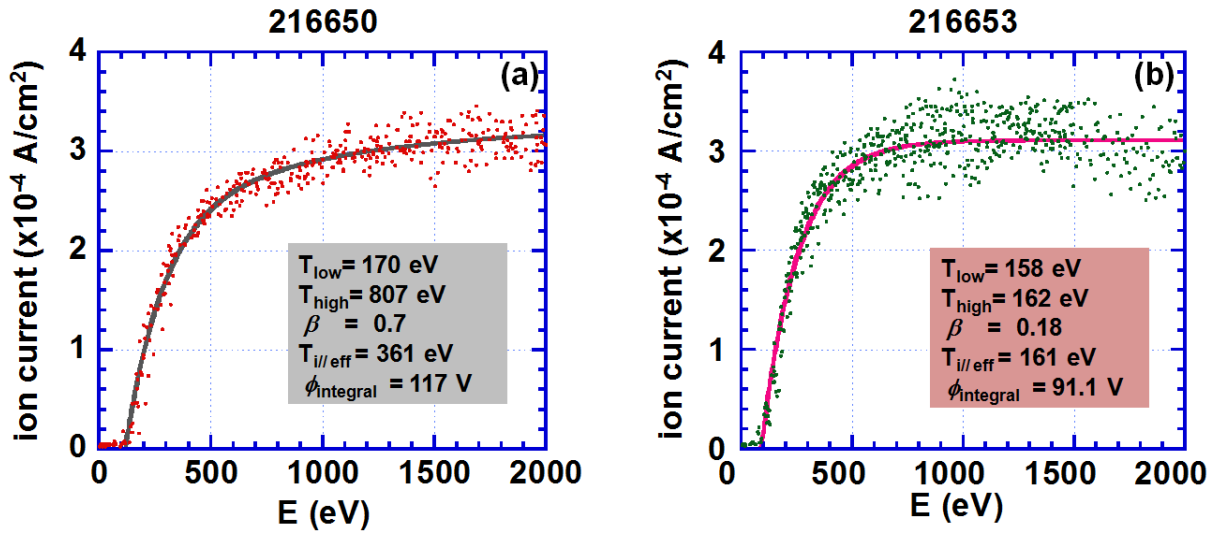


Fig. 4.9 Results of double-components fitting for the V - I curve of (a): higher power plasma and (b): lower power plasma.

In Fig. 4.10, the energy spectrum of the ion flux is plotted with the curve of the energy distribution evaluated from the fitting for the V - I profile. Although the large uncertainty of the energy profile in high energy region exists, the tail-component in the energy range of 1000~2000eV can be observed. In the GAMMA 10/PDX tandem mirror, Alfvén ion cyclotron (AIC) wave is driven by the anisotropy of the perpendicular and parallel ion temperature of the core plasma. In that case, ions with energy 1000~2000eV is transported to the end region by the resonance effect with the AIC wave. In the higher power plasma shot, perpendicular ion temperature of the core plasma is increased and the anisotropy becomes strong. Therefore the high energy component is assumed to be driven by the AIC wave.

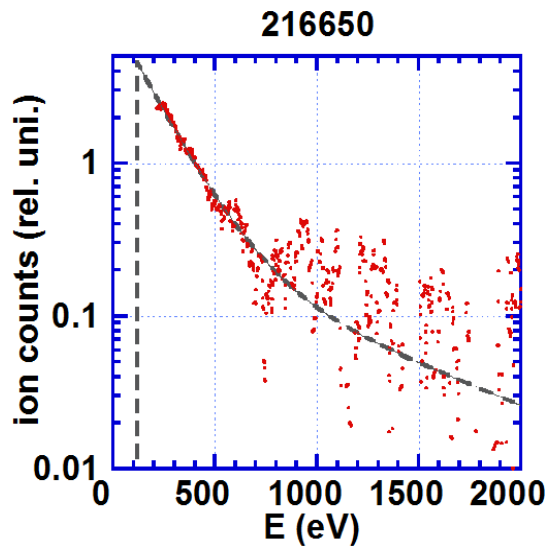


Fig. 4.10 Energy spectrum of higher power plasma with differentiated curve of double-components fitting for the V - I profile.

Dependence of the parallel temperature of the end-loss ion flux to the power of ICRF heating is plotted in Fig. 4.11. In the figure, values of the ion temperature obtained from the double-components fitting for $V-I$ curve ($T_{i/eff}$), the single-component fitting for the energy spectrum ($T_{i/spec}$) and the ion temperature evaluated from the calorimetric measurement at the end region are compared. It is found that the ion temperatures measured by the calorimetric measurements are closer to the parallel ion temperature evaluated from the double-components fitting especially in the area of high ICRF power. In standard operations of GAMMA 10/PDX, operation ranges of the ion energy for the end-loss ion flux are 100~450 eV by double components fitting and 150~300 eV by single component Maxwellian fitting.

In the expected fusion reactor, ion temperature is several 100 eV at the boundary region called scrape off layer (SOL) and the temperature is reduced to about 10 eV at divertor regions. From the measurement of the end-loss ion flux by ELIEA, the high ion temperature and Maxwellian like energy distribution of the ion flux were observed. In addition, it is found that the temperature and energy distribution of the ion flux can be controlled by changing the power of ICRF heating. In comparison with conventional linear divertor simulators, it can be noted that the tandem mirror have wide controllable range of the ion temperature. These properties of the end-loss ion flux of the tandem mirror are useful for the fusion study since they fit well to the requirement of current divertor simulation studies introduced in chapter 1.

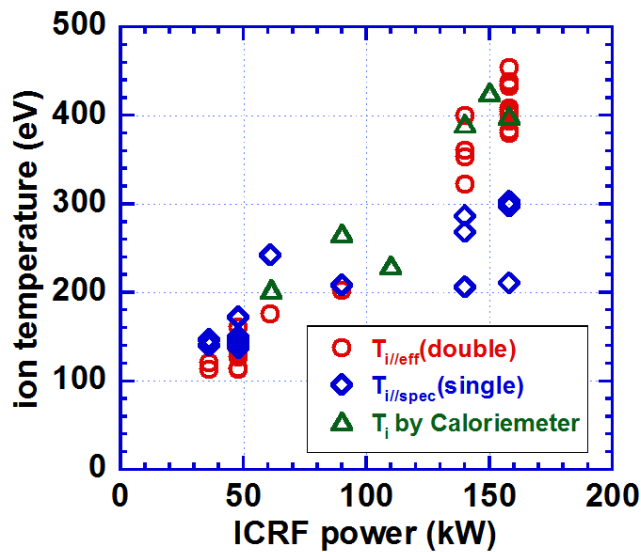


Fig. 4.11 Dependence of parallel ion temperature of the end-loss ion flux to the power of ICRF heating.

4.4 Analysis on the Ion Particle Flux

Since the end-loss ion flux is the axial loss of the core plasma in the mirror region, the value of ion current density measured by ELIEA is expected to depend on the density of mirror confined plasma. In Fig. 4.12, the dependency of the ion current density (west, top, ch1) on the electron line density of the central cell plasma (NLCC) is shown. Apparently the value of ion current density is increasing as NLCC increases. Here, since

the ion current density of ELIEA is measured at the position behind the end-plates ($z = 1330$ cm), calibration of the value is required to evaluate the ion particle flux at the region of divertor simulation experiment ($z = 1030\sim 1100$ cm).

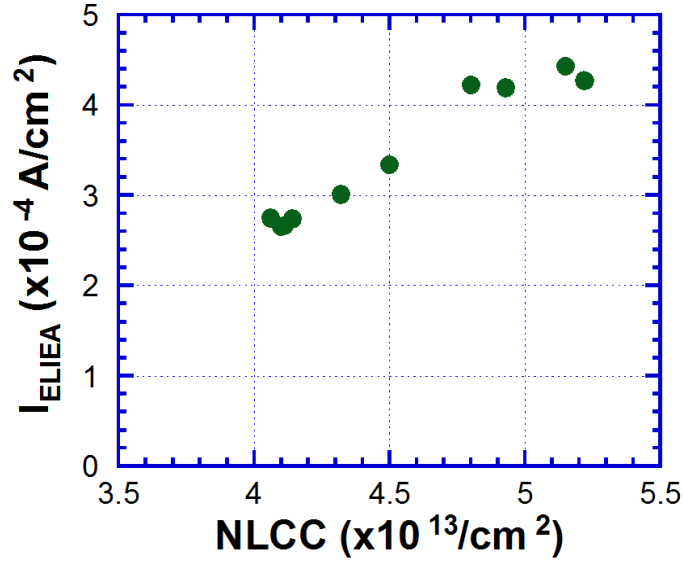


Fig. 4.12 Dependence of ELEA ion current density on the electron line density of central-cell plasma.

In order to convert the ELIEA ion current to the ion particle flux at $z = 1030$ cm, calibration of ELIEA with the electrostatic probe at $z = 1030$ cm (Fig. 2.4) was performed. Due to the geometry of measurement, the measurement of ESP at $z = 1030$ cm cannot be performed with ELIEA simultaneously. Thus the calibration was based on the analysis on the data of each measurement results. First, the dependence of the ion particle flux measured by ESP on the NLCC is examined and the particle flux by ESP is represented as the function of NLCC by assuming the parabolic function (Fig.4.13).

$$\Gamma_i \propto \frac{N_i^2}{T_{i//}^{3/2}} \propto \frac{(NLCC)^2}{T_{i//}^{3/2}} \quad (4-5)$$

Then, the dependence seen in the ESP case is compared with the case of the ELIEA measurement and finally, the relationship between the ELIEA ion current and ESP particle flux was revealed as Eq.(4-6) and Fig. 4.14,

$$\Gamma_i = I_{\text{ELIEA}} \times 1.275 \times 10^{22} (\text{particles}/\text{m}^2\text{sec}). \quad (4-6)$$

Here, the unit for I_{ELIEA} is $10^{-4} \text{ A}/\text{cm}^2$. The error of Eq. (4-5) due to the fitting errors in Fig. 4.13 is evaluated to be $\pm 10\%$.

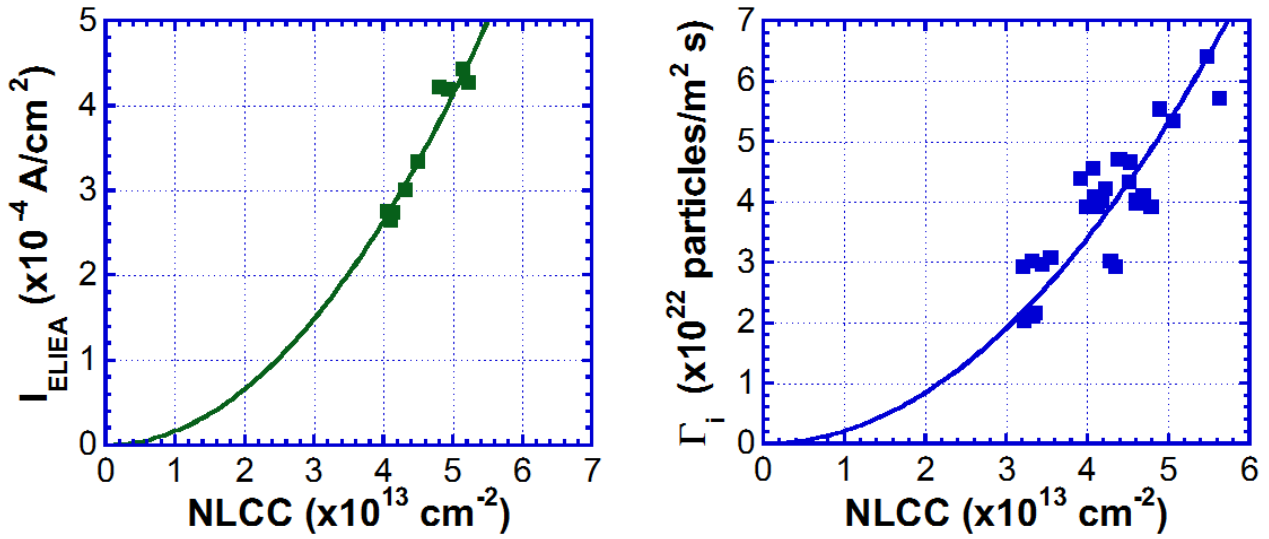


Fig. 4.13 Plots of parabolic dependences of the ELIEA ion current and ESP particle flux on the NLCC.

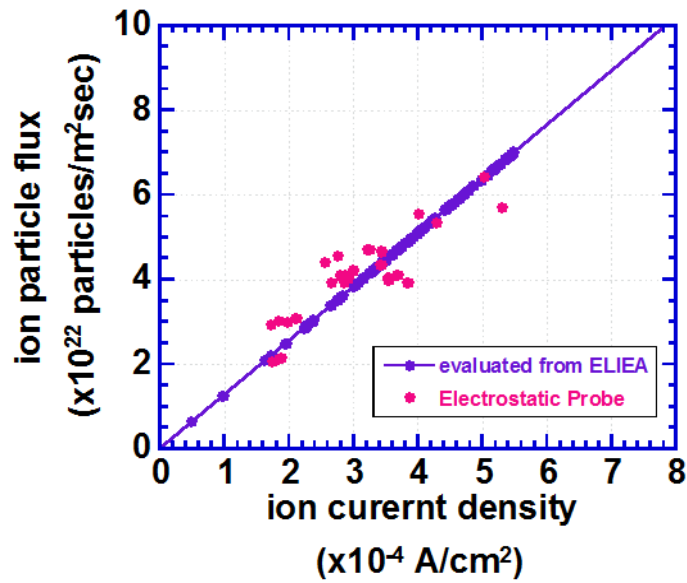


Fig. 4.14 The measured and evaluated values of ion particle flux plotted against the ion current density.

Therefore it is found that ion particle flux of 2~6 ($\times 10^{22}$ particles/ $m^2\text{sec}$) is achieved in the standard operation of GAMMA 10/PDX. In fusion reactors, the range of ion particle flux in the divertor region is expected to be $10^{23}\sim 10^{25}$ (particles/ $m^2\text{sec}$). Therefore, in order to reproduce the circumstances of fusion divertor precisely, the ion particle flux must be increased by several orders. For the increase of the ion particle flux, plasma operations with and additional heating or fueling will be required.

4.5 Typical Radial Profile of the End-Loss Ion Flux

Radial profiles of the end-loss ion flux and the electron density of the central-cell plasma (NECC) with high diamagnetism (#228325, DMCC = 0.6×10^{-4} Wb) and low diamagnetism plasma (#228339, DMCC = 0.14×10^{-4} Wb) are investigated. Figure 4.15 shows the time behavior of the diamagnetism of the plasma and Fig. 4.16 shows the radial profiles of the parameters plotted against x-axis scaled at $z=1030$ cm. In the plot of particle flux, the error bar is given from as the standard deviation of the ion current. It is seen that in both high and low diamagnetism plasma, the radial profile of the ion particle flux and the NECC have the full width half maximum (FWHM) around 12 cm at $z = 1030$ cm.

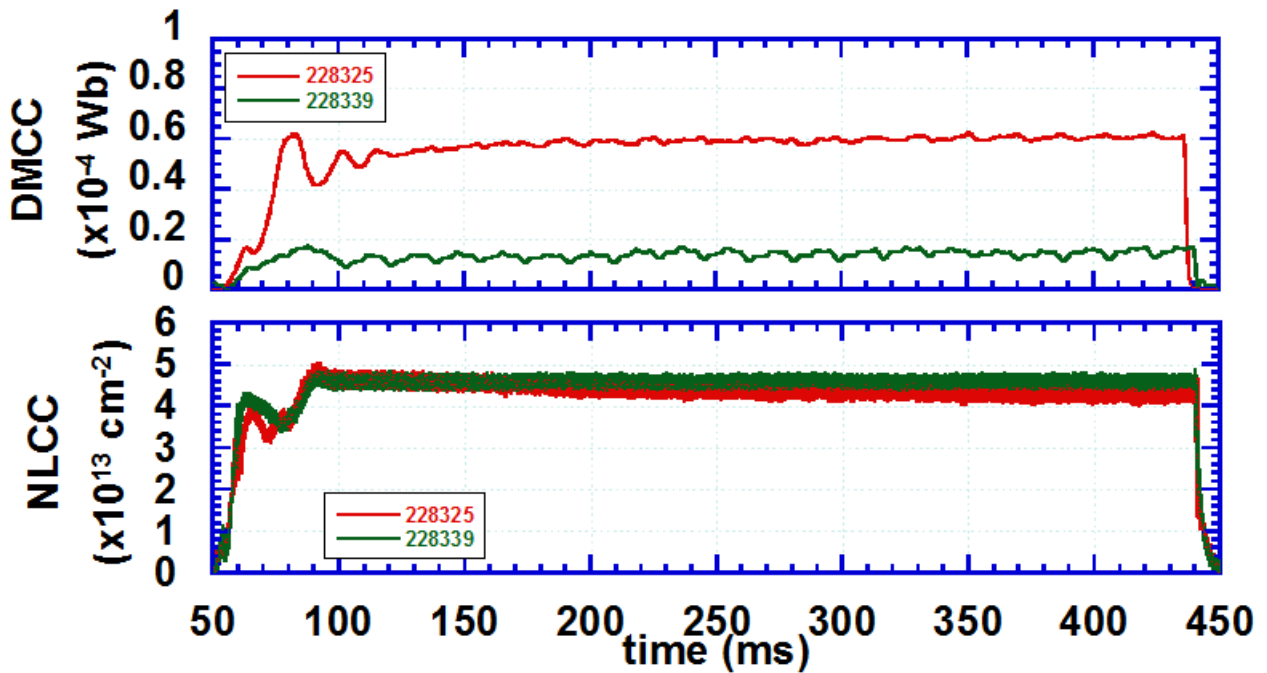


Fig. 4.15 Time evolution diamagnetism and line density of central-cell plasma.

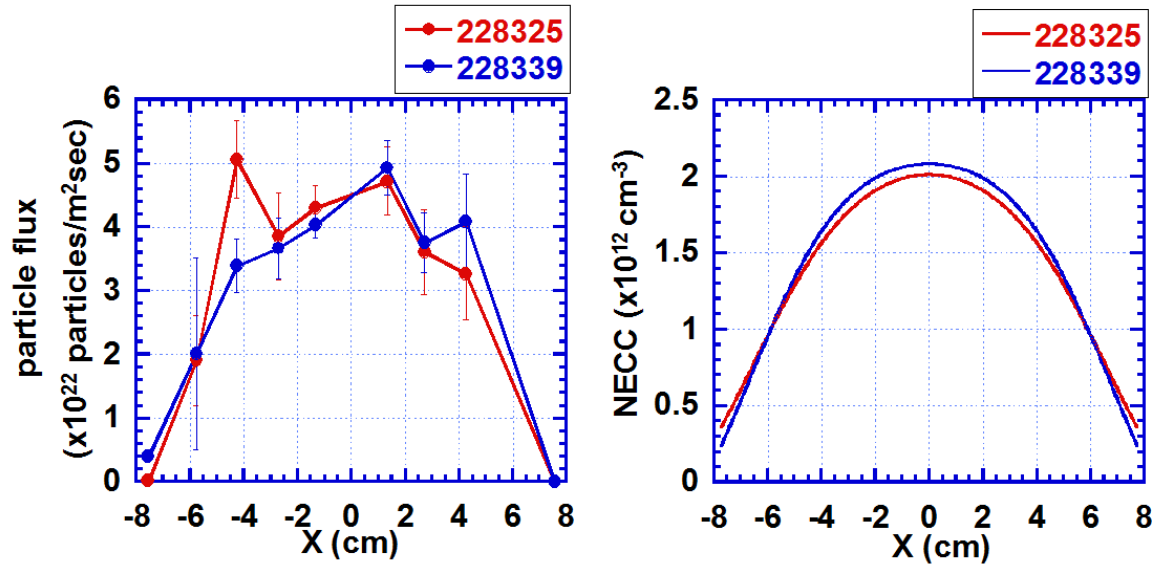


Fig. 4.16 Radial profiles of the ion particle flux and the electron density in the central-cell (NECC) in plasma discharges with high and low diamagnetism of the central-cell plasma.

The radial profiles of parallel ion temperature are plotted in Fig. 4.17. In the higher DMCC plasma, higher ion temperature is obtained. It is seen that the radial distribution of ion temperature is flat over -4~4 cm compared with the ion current density in Fig. 4.16. Since the heat flux is evaluated as $T_{i||} \times J_i$, the radial distribution of heat flux will become similar to the radial profile of the ion particle flux if the radial distribution of the ion temperature is flat. As shown in Fig. 4.18, the result of heat flux and particle flux measurement by calorimeter and ESP [47] shows that the FWHM is about 8 cm for both heat flux and particle flux. Therefore it can be concluded that the flat radial profile of the ion temperature measured by ELIEA agrees with the result of calorimeter and ESP measurement.

These results show that the end-loss ion flux of the tandem mirror has typical radius around 5 cm. Therefore it is confirmed that the divertor simulation experiment with 10 cm scale plasma diameter can be performed by using the tandem mirror.

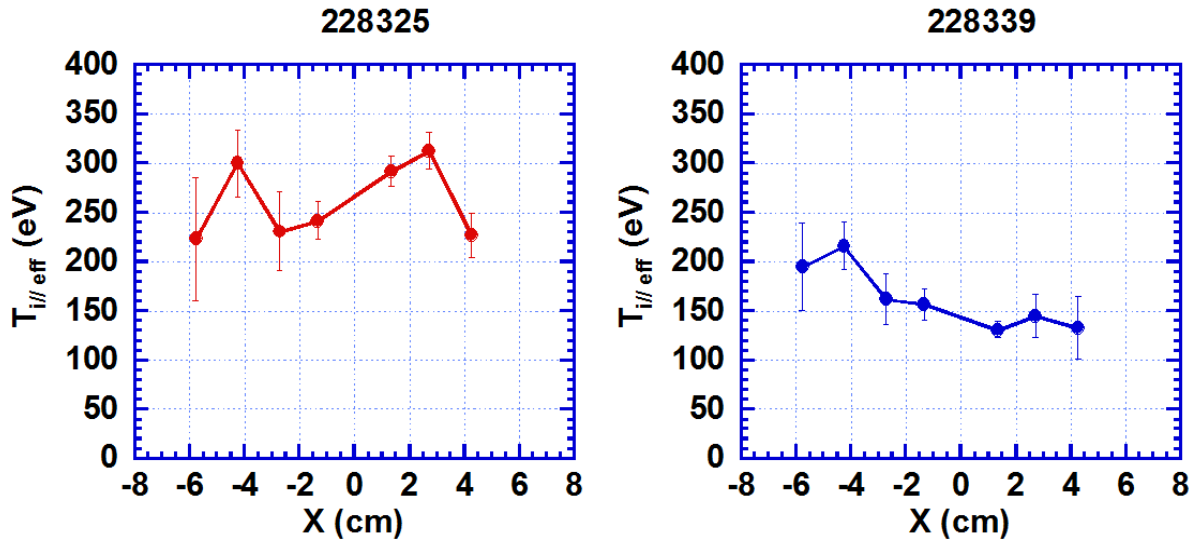


Fig. 4.17 Radial profiles of parallel ion temperature measured by ELIEA in west end-cell.

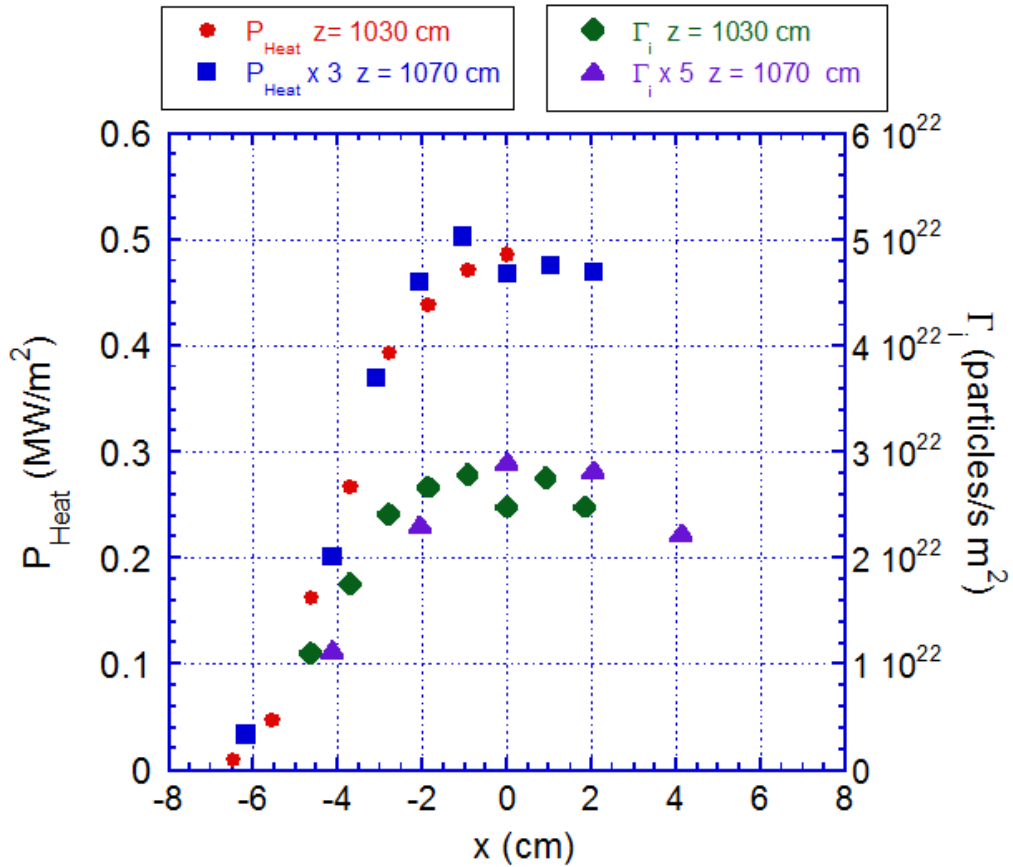


Fig. 4.18 Radial profiles of the ion particle flux and the heat flux along x-axis measured by electro static probe and Calorimeter at $z = 1030$ and 1070 cm [43].

Chapter 5 Enhancement of the Ion Particle Flux by Additional Fueling and Heating

In Chapter 4, characteristics of the end-loss ion flux in the standard operations of GAMMA 10/PDX were investigated and it was shown that the end-loss ion flux has high ion temperature and large plasma radius. On the other hand, the ion particle flux of the end-loss flux is lower than that expected in divertor of fusion devices by a few orders. In this chapter, behavior of the end-loss flux with the additional plasma heating and fueling such as ICRF heating in anchor-cells and supersonic molecular beam injection in the central-cell are reported. Then, the effect of additional actions on the enhancement of ion particle flux will be investigated.

5.1 Ion Particle Flux in Previous Works

In previous works [48, 49], several additional fueling and heating for the standard plasma of GAMMA 10/PDX were performed in order to enhance the ion particle flux. As a result shown in Fig. 5.1, it was found that the superimposing of ICRF heating into anchor-cell is effective to increase the amount of ion particle flux. It is also observed that the ion flux have dependence on the electron line density of the plasma in the central-cell (NLCC). With the help of additional ICRF heating, the ion particle flux was increased to $8\sim 9 \times 10^{23}$ particles/m²sec.

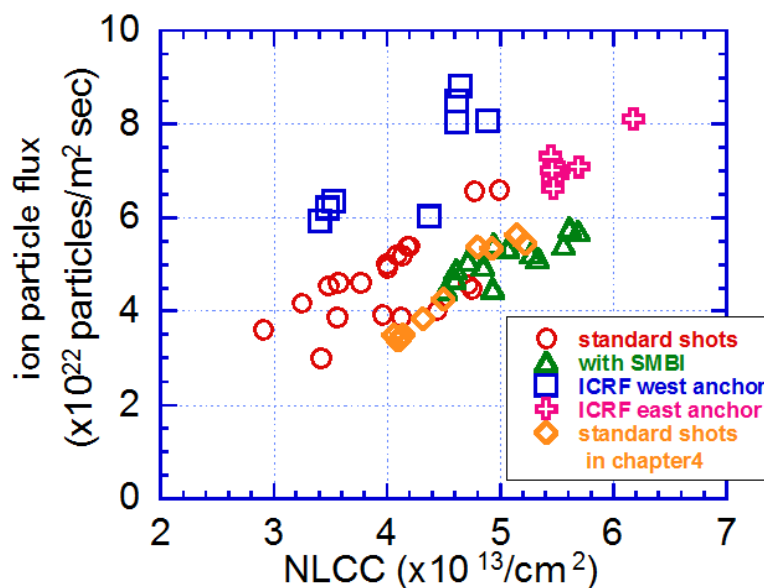


Fig. 5.1 Ion particle flux with various experimental conditions evaluated from the ELIEA measurement in the west end-cell ch1 plotted against the electron line density of the central-cell plasma.

5.2 Enhancement of the Particle Flux by Supersonic Molecular Beam Injection

The Supersonic Molecular Beam Injection (SMBI) system injects hydrogen gas into the central-cell plasma from a small aperture and with high plenum pressure. As a result, hydrogen molecules are injected to the central-cell plasma with velocity larger than sonic speed. The results of SMBI with the condition of the plenum pressure of 1.0 MPa and the pulse length of 0.4 ms are shown in Fig. 5.2. It is observed that the electron line density (NLCC) was increased by 60% and the end-loss ion particle flux was increased by 60% while the diamagnetism (DMCC) is decreased to 30% of its original value. The radial profiles of the end-loss ion flux with and without SMBI (Fig. 5.3) indicates that the increase of ion flux in outer ($r > 3\text{cm}$) region is larger than that in inner region ($r < 3\text{cm}$) and therefore the plasma radius is increased.

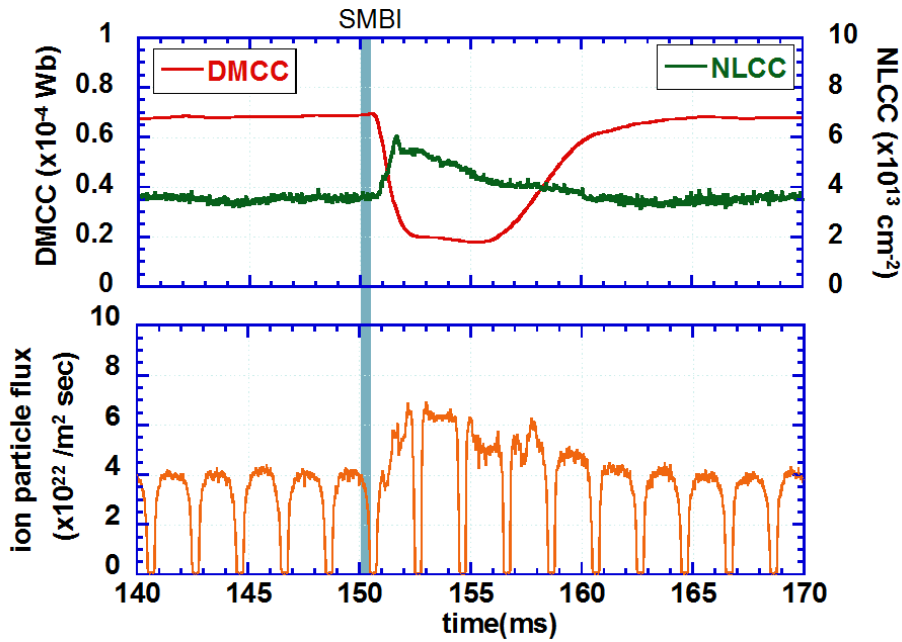


Fig. 5.2 Time evolutions of diamagnetism of central plasma (DMCC), electron line density (NLCC), and ion particle flux in west end-cell in the experiment of supersonic molecular beam injection.

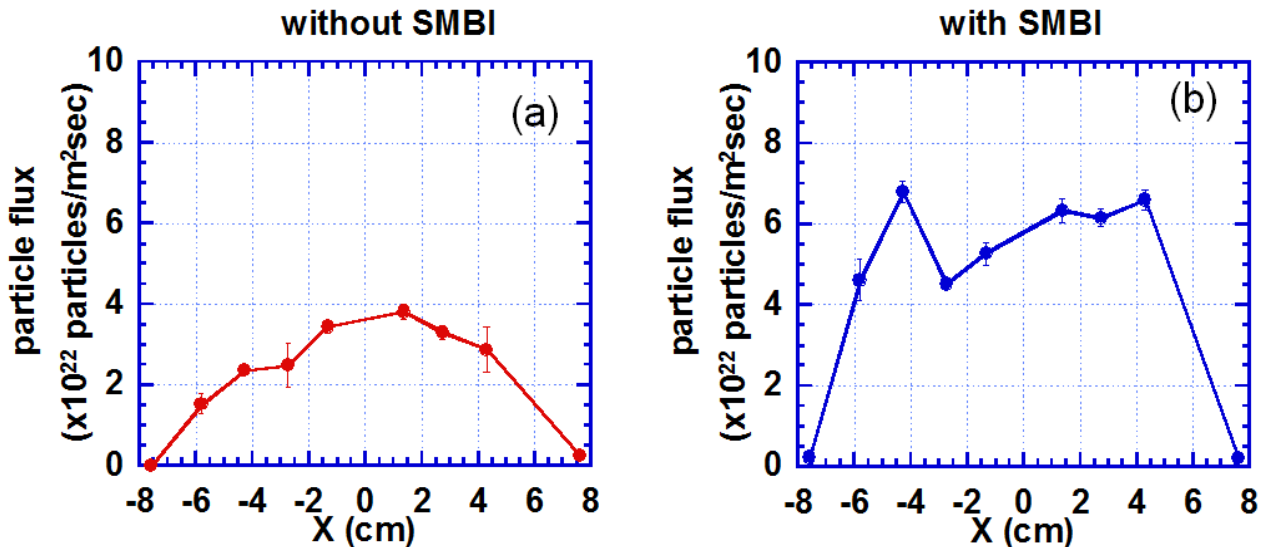


Fig. 5.3 Radial profiles of the end-loss ion particle flux (a): with SMBI and (b): without SMBI.

Figure 5.4 shows the radial profile of parallel ion temperature during the SMBI. In this case, the ion temperature is decreased as the total energy of the plasma (DMCC) is decreased. Therefore in comparison with standard high-diamagnetism plasma experiment, ion temperature of the ion flux is lower in SMBI experiment. As shown in Fig. 5.4, the ion temperature with SMBI is not changing largely over the radius of 4 cm. thus the gas injection by SMBI can be used to enlarge the radius of the end-loss ion flux.

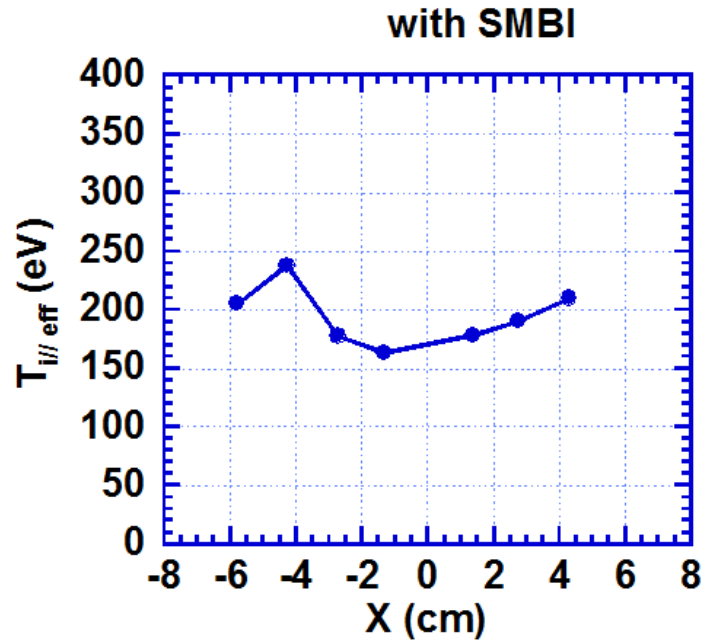


Fig. 5.4 Radial profile of the parallel ion temperature in SMBI experiment.

5.3 Enhancement of the Particle Flux by ICRF Heating in Anchor Region

As seen in Fig. 5.1, superimposing of an additional ICRF heating into anchor-cell is quite effective for the enhancement of ion particle flux. In this section, results of the plasma experiments with additional ICRF heating are described.

5.3.1 Additional ICRF Heating with East Anchor DAT

The time behaviors of diamagnetism in the central-cell, line density in each cell and the end-loss ion current in the west end-cell during the experiment of the additional ICRF in east anchor-cell are shown in Fig. 5.5. With the ICRF heating by the DAT antenna in east anchor-cell, the line density in each cell of GAMMA 10/PDX and the end-loss ion current were increased and the diamagnetism of the central-cell plasma was decreased. The radial profiles of ion particle flux shown in Fig. 5.6 indicates that the ICRF heating increased the ion particle flux without making large change of the FWHM for the radial profile. The results of energy analysis for the experiment are shown in Fig. 5.7. As discussed in chapter 4, the evaluation of the ion energy from the V - I curve is used as ion temperature of the end-loss ion flux. The plot of energy spectrum and the value of $T_{i/spec}$ are also plotted in order to clarify that the behavior of ion energy during the additional plasma heating is within the consideration made in chapter 4. It is observed that the plasma in the experiment had relatively high parallel ion temperature and low plasma potential before superimposing ICRF wave. Then, as the additional ICRF heating was performed, the parallel ion temperature was decreased and the plasma potential was increased. Since the diamagnetism of the plasma was decreased during the superimposing of ICRF, it can be assumed that the decrease of the parallel ion temperature was caused by the decrease of ion temperature of the central-cell plasma.

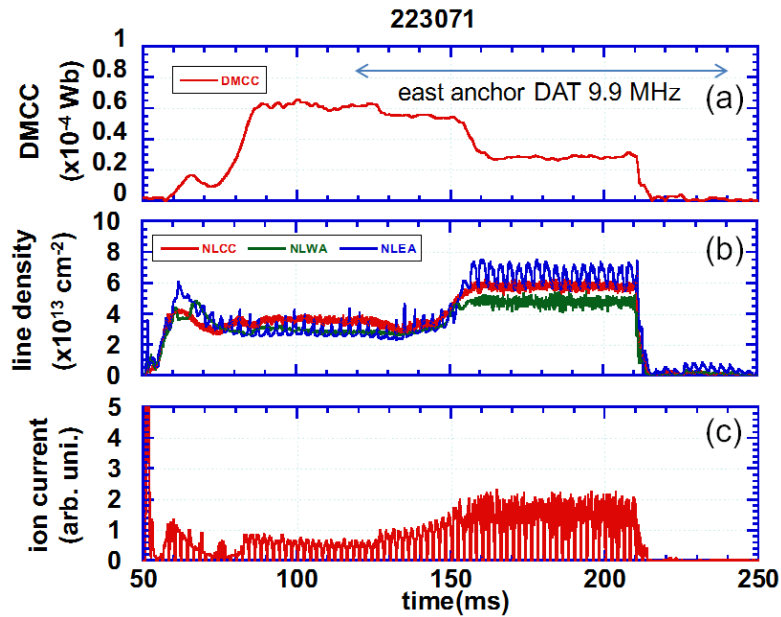


Fig. 5.5 Time evolutions of (a): DMCC, (b): electron line density in each cell (NLCC, NLWA, NLEA), and (c): ion particle flux in in the experiment of additional ICRF heating in east anchor-cell.

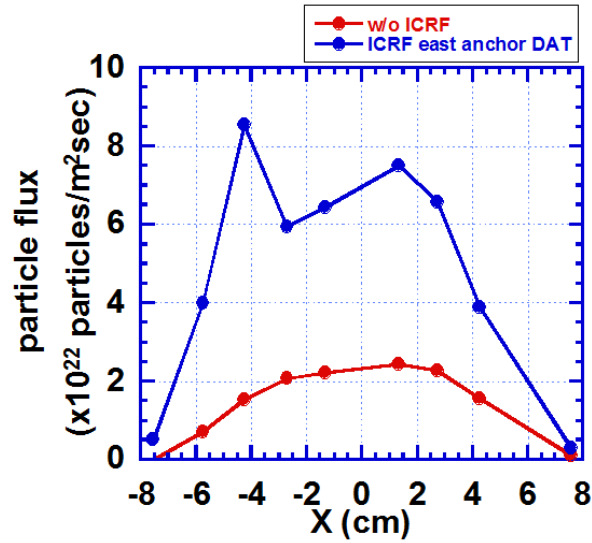


Fig. 5.6. Radial profiles of the ion flux in experiment of additional ICRF by east anchor DAT antenna.

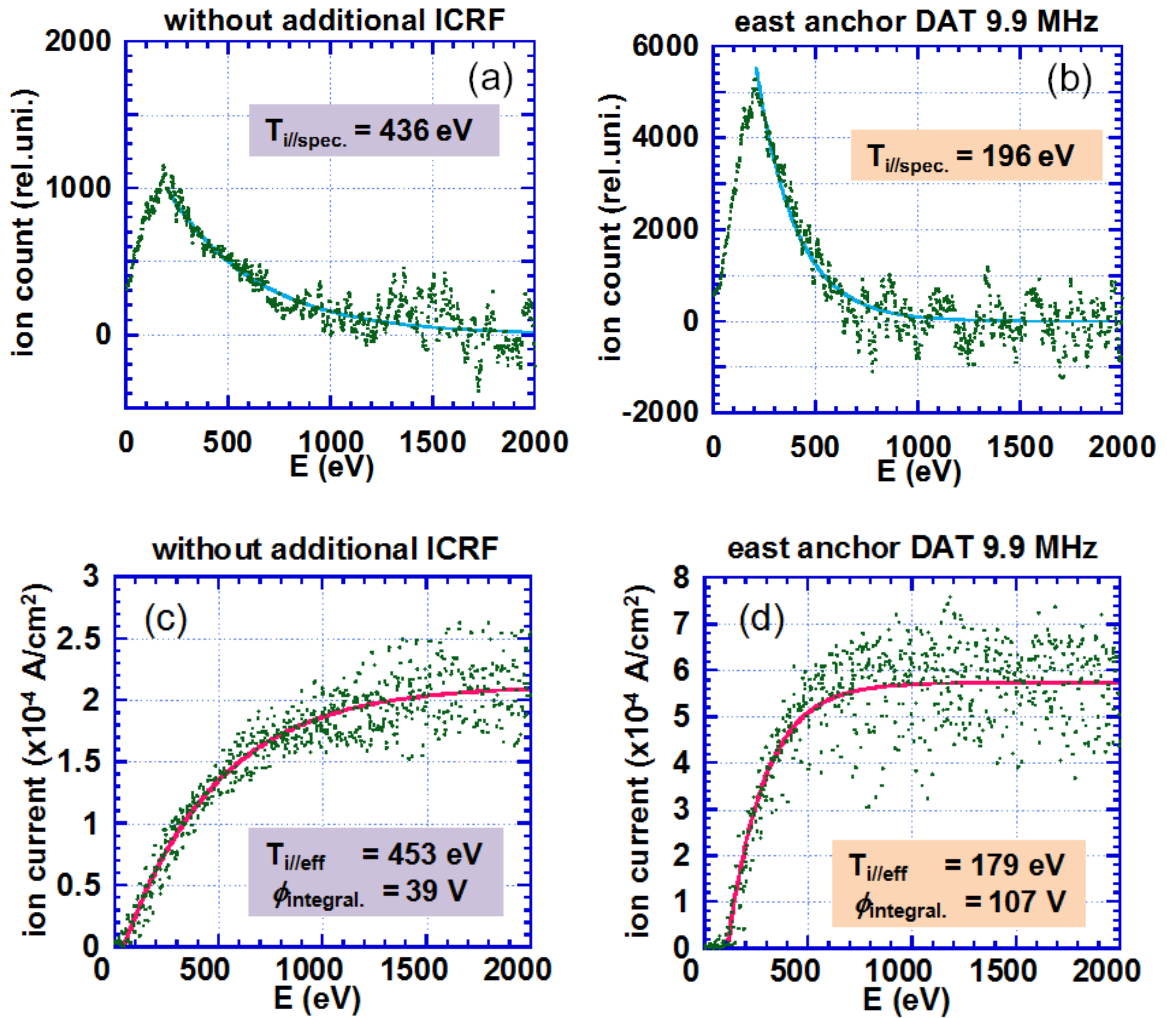


Fig. 5.7. Ion temperature and plasma potential evaluated from (a): energy spectrums without DAT (b): spectrum with DAT, (c): V - I curve without DAT and (d): V - I curve with east anchor DAT.

5.3.2 Additional ICRF Heating with West Anchor DAT

As in the case with additional ICRF heating by the DAT antenna in east anchor-cell, superimposing ICRF wave from the DAT antenna in west anchor-cell is also very effective for the production of intense ion particle flux. Figure 5.8 shows the time evolutions of diamagnetism in central-cell, line densities in each cell and the end-loss ion current measured by ELIEA at west top ch1. The line density of plasma in each cell and the end-loss ion current were increased by the superimposing ICRF by DAT antenna in west anchor-cell while the diamagnetism in the central-cell was decreased. In comparison with the case with east anchor DAT antenna experiment, the radial profile of the ion particle flux become much narrower in the case of west anchor DAT as shown in Fig. 5.9. The FWHM of the radial profile with west anchor DAT antenna is about 10 cm, which is about a half of the value in standard plasma. On the other hand, the maximum value of the ion particle flux with the west anchor ICRF is higher than east anchor case and the value close to 10^{23} particles/m²sec was achieved. Also it should be noted that the plasma potential increase largely by addition of ICRF west. As shown in Fig. 5.10, both potential evaluated from the energy spectrum and the potential evaluated from the $V-I$ profile are raised by the ICRF heating. Basically, potential of the mirror confined plasma depends on the electron temperature because the energy of electrons mainly determines the formation of plasma potential [50]. Therefore it is indicated that the electrons had been affected by the superimposition of ICRF by west anchor DAT.

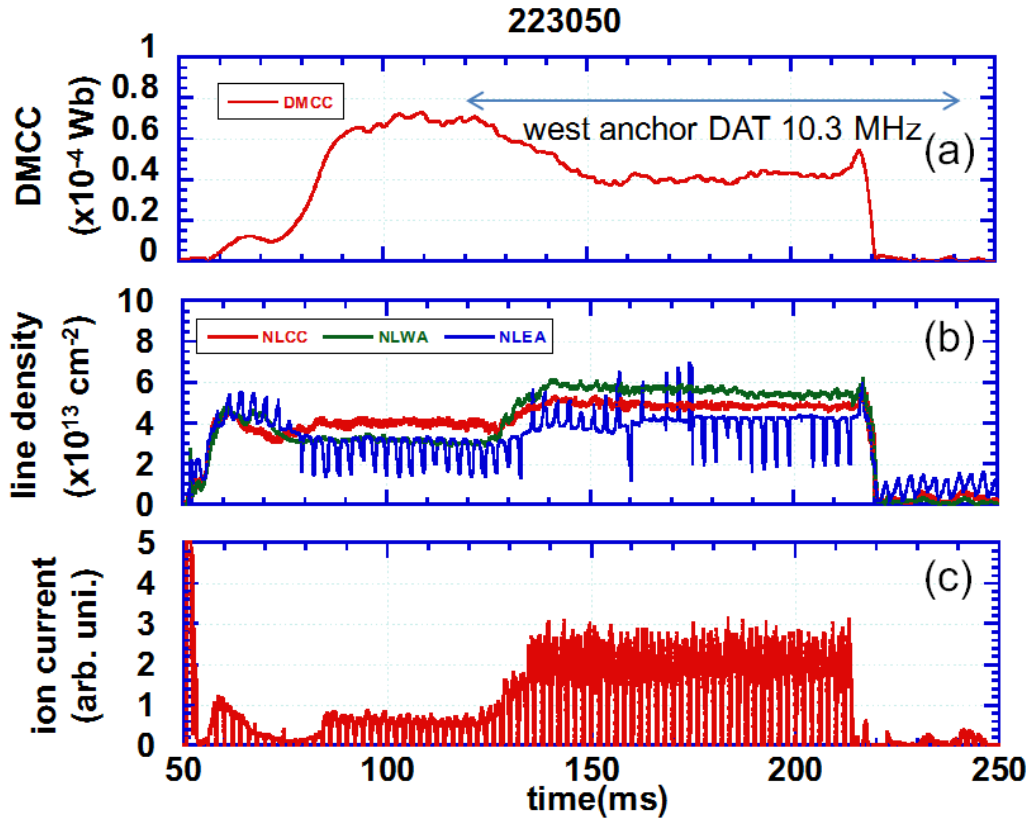


Fig. 5.8 Time evolutions of (a): DMCC, (b): electron line density in each cell and (c): ion particle flux in west end-cell in the experiment of additional ICRF heating in west anchor-cell.

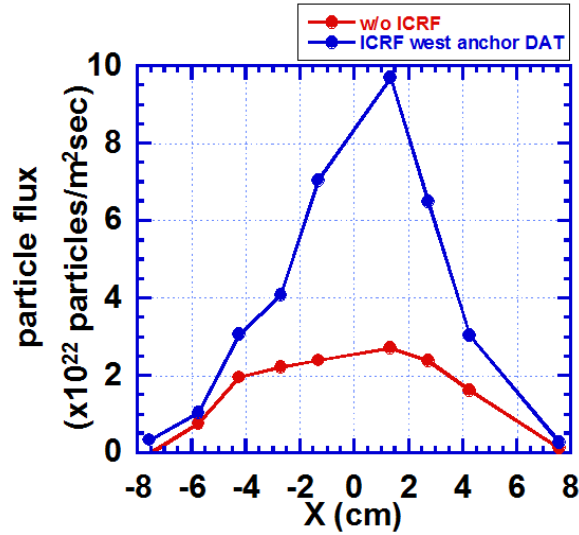


Fig. 5.9. Radial profiles of the ion flux in experiment of additional ICRF by west anchor DAT antenna.

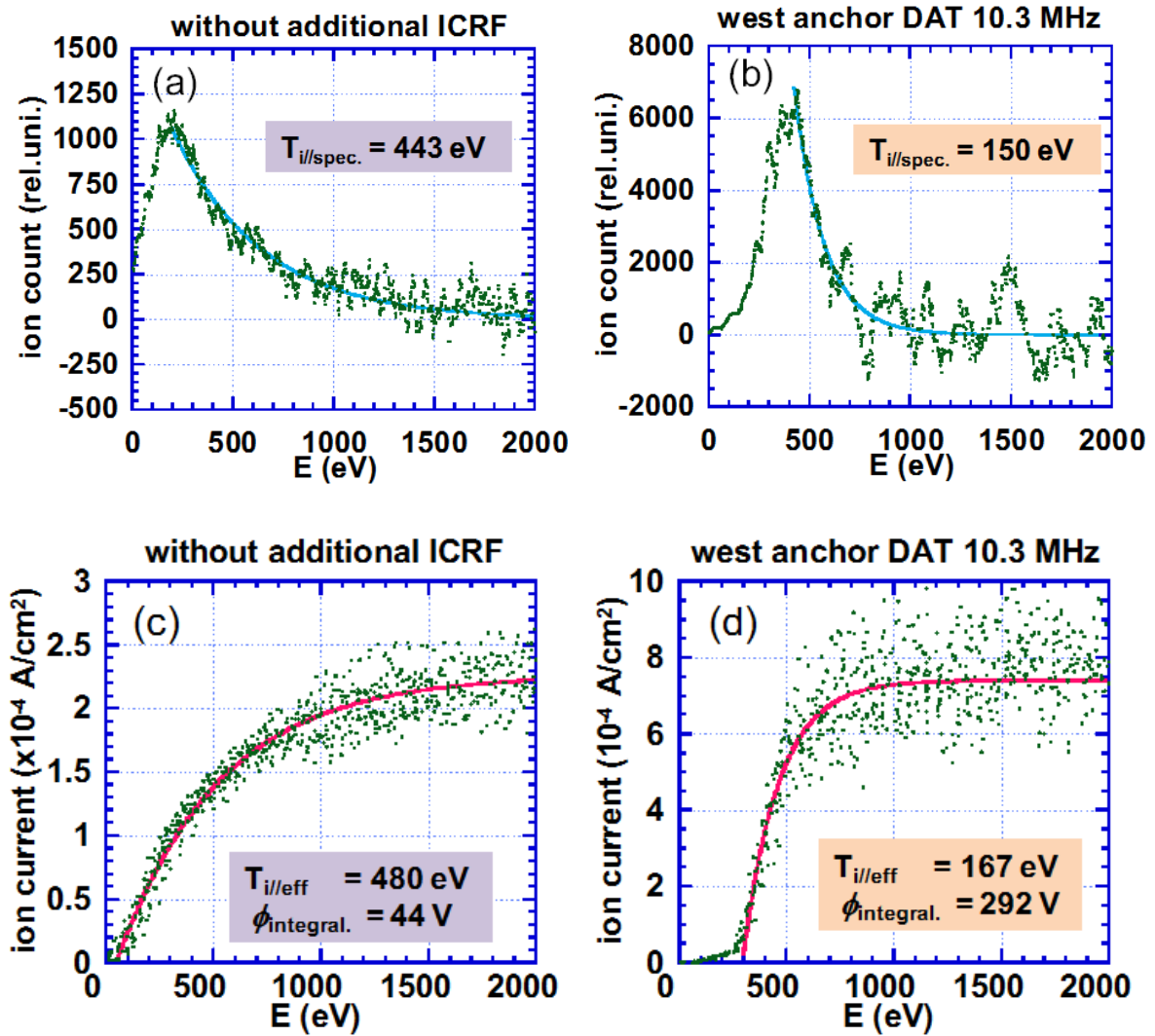


Fig. 5.10. Ion temperature and plasma potential evaluated from (a): energy spectrums without DAT (b): spectrum with DAT, (c): V-I curve without DAT and (d): V-I curve with west anchor DAT.

5.3.3 Gas Puffing with Anchor DAT

In this experiment, the additional ICRF heating was applied to the plasma twice as two separate pulses. Then, the gas fueling by using the Gas Puff #2a, which locates at the west end of the central-cell was applied together with the second pulse of the ICRF heating. With the gas fueling and the superimposing of ICRF by west anchor DAT antenna, electron line density of the plasma in each cell and the end-loss ion current are increased (Fig. 5.11). The increase of the ion current and line density in the second pulse are larger than those in the first pulse of ICRF because of the gas fueling. As seen in Fig. 5.12, the radial profile of the ion flux become broader as the gas is added. Furthermore, it is observed that the parallel ion temperature and plasma potential are decreased by the use of gas puffing as shown in Figs. 5.13 and 5.14. Therefore it was found that similar to the case of SMBI, the injection of gas can be used for the control of the radial profiles of the particle flux, ion temperature and the plasma potential during the addition of ICRF heating by west anchor DAT antenna.

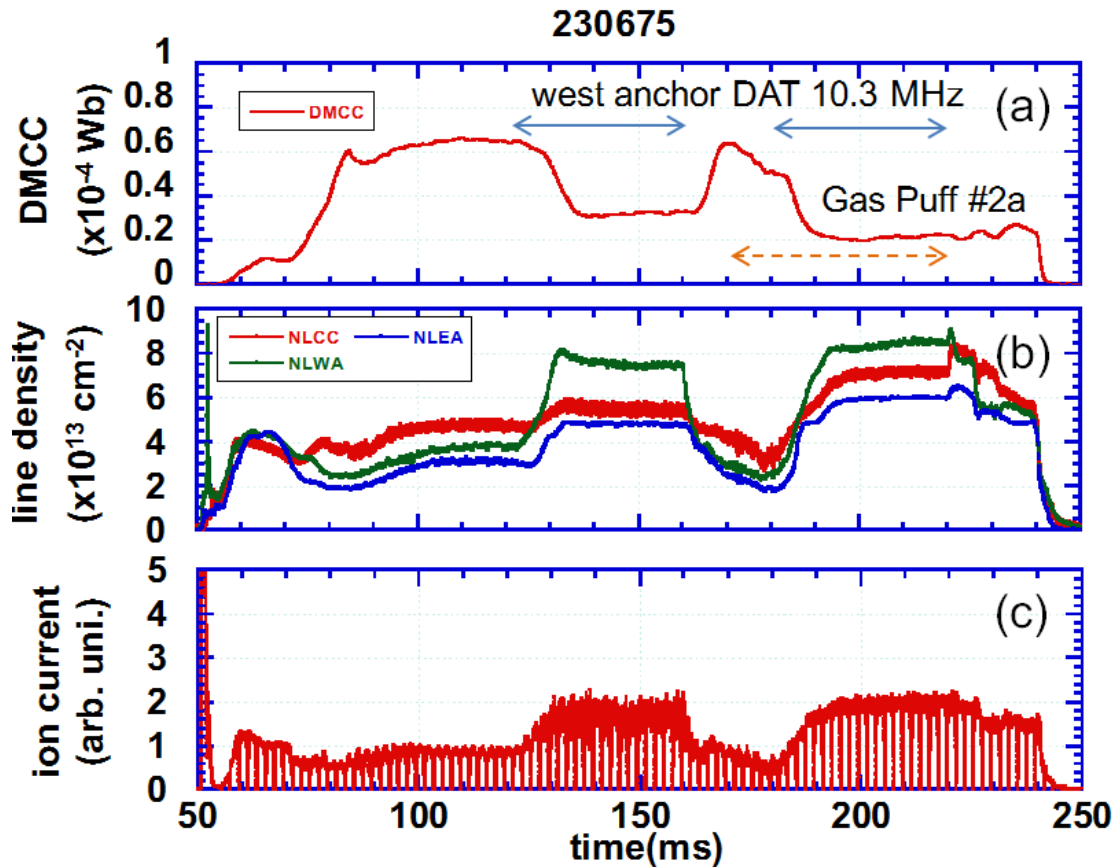


Fig. 5.11. Time evolutions of (a): DMCC, (b): electron line density in each cell and (c): ion particle flux in west end-cell in the experiment of additional ICRF heating in west anchor-cell and gas puffing.

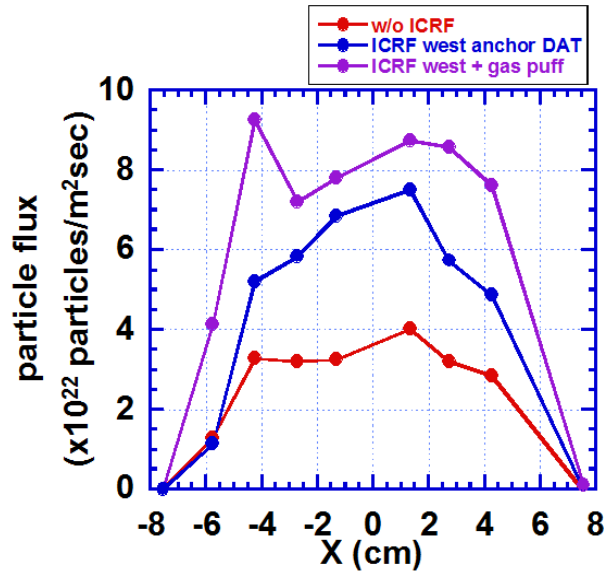


Fig. 5.12. Radial profiles of the ion flux in experiment of additional ICRF in west anchor and Gas Puffing.

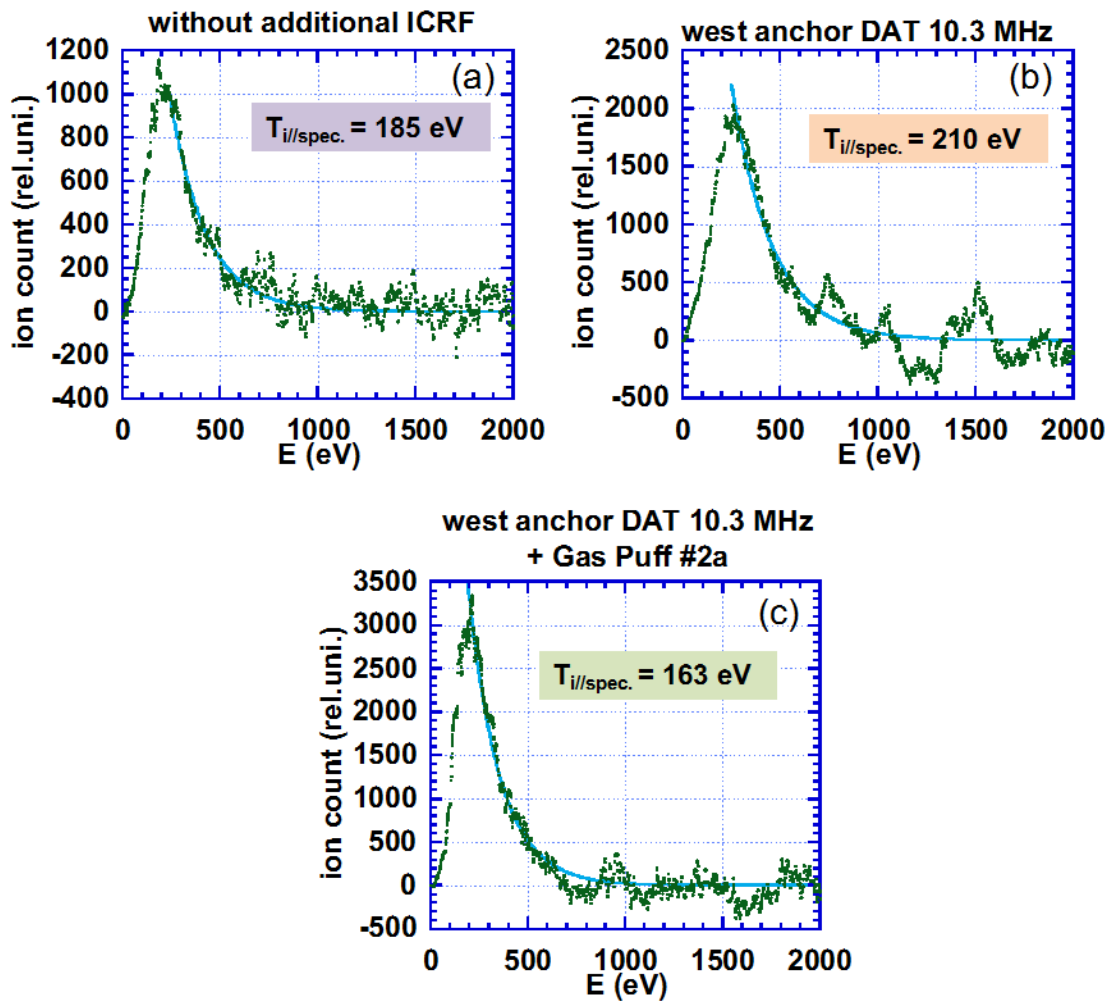


Fig. 5.13. Ion temperature and plasma potential evaluated from energy spectrums in the conditions of (a): without DAT, (b) with DAT ICRF heating and (c): with ICRF heating by the west anchor DAT antenna and gas puffing.

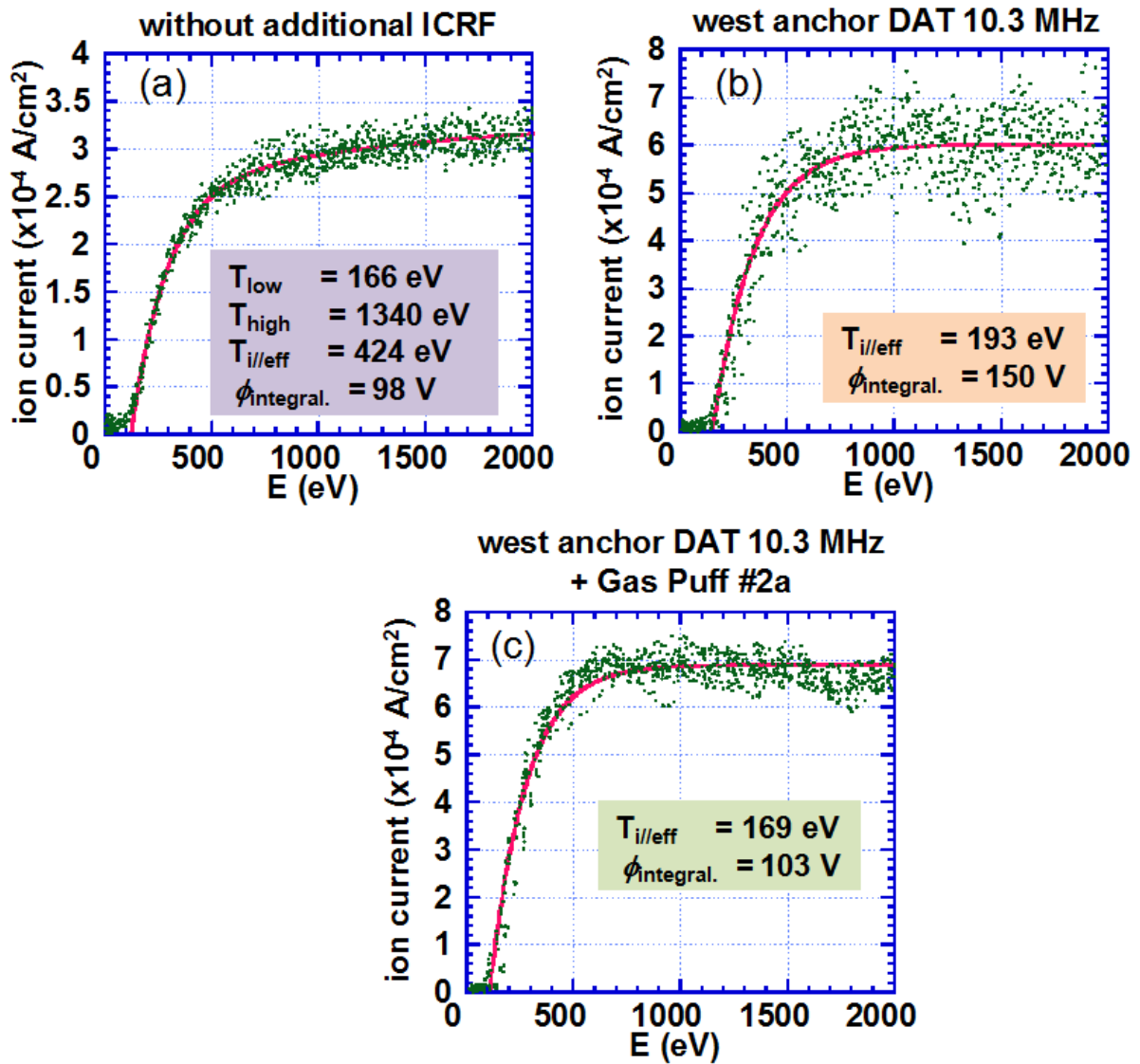


Fig. 5.14. Ion temperature and plasma potential evaluated from V - I curve in the experiment of additional ICRF heating by west anchor DAT antenna and gas puffing.

5.3.4 Simultaneous ICRF Heating in East and West Anchor-Cells

In order to achieve the ion particle flux higher than 10^{23} particles/m²sec, gas puffing and additional ICRF heating by both east and west anchor DAT antennas were performed simultaneously by using the power supply system of the type-II (ICRF2) for the DAT antennas in anchor-cells. The time evolutions of the experimental parameters are plotted in Fig. 5.15. It can be seen that the diamagnetism of the plasma is low compared to the other experiments since the ICRF heating from the type-II antenna is not applied. After the gas puffing and the ICRF heating from the DAT antennas are applied, the electron line density in each cell and the end-loss ion current were increased largely. As shown in Fig. 5.16, the maximum amount of the ion particle flux in this experiment achieved the value larger than 10^{23} particles/m²sec, which is in a range of expected particle flux in the divertor region of fusion experimental machine. The FWHM of the radial profile become larger during the ICRF. As seen in Fig. 5.17, the parallel ion temperature of the ion flux became lower during the ICRF. However, the ion temperature is still higher than 100 eV. Similar to the other DAT experiments, the increase of the ϕ_{integral} was observed. It is found the ion flux during the operation of simultaneous ICRF heating from the DAT antennas have high particle flux and high ion temperature at the same time. It is also notable that the ion temperature of 100 eV was obtained with only the plasma heating from ICRF1.

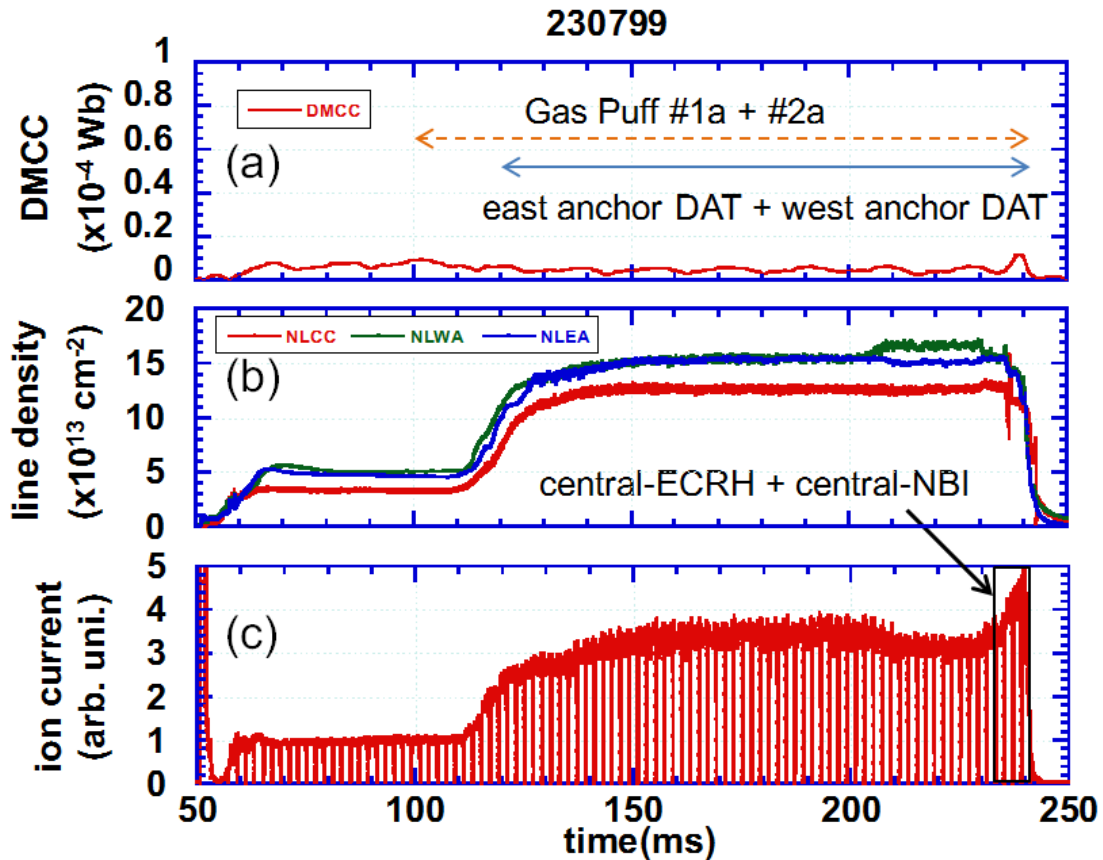


Fig. 5.15 Time evolutions of (a): DMCC, (b): electron line density in each cell and (c): ion particle flux in west end-cell in the experiment of additional ICRF heating in both east and west anchor-cells.

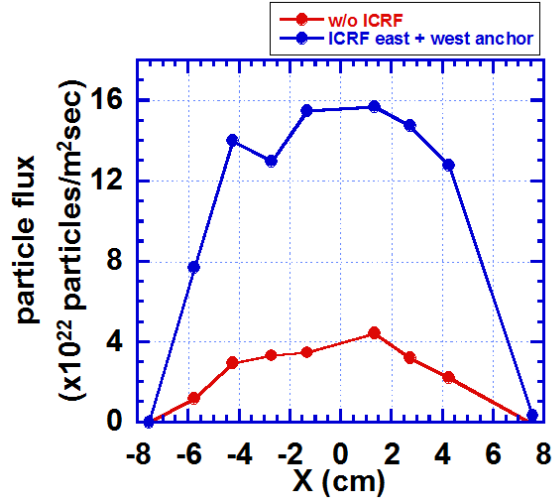


Fig. 5.16. Radial profiles of the ion flux in experiment of additional ICRF in both east and west anchor region together with Gas Puffing.

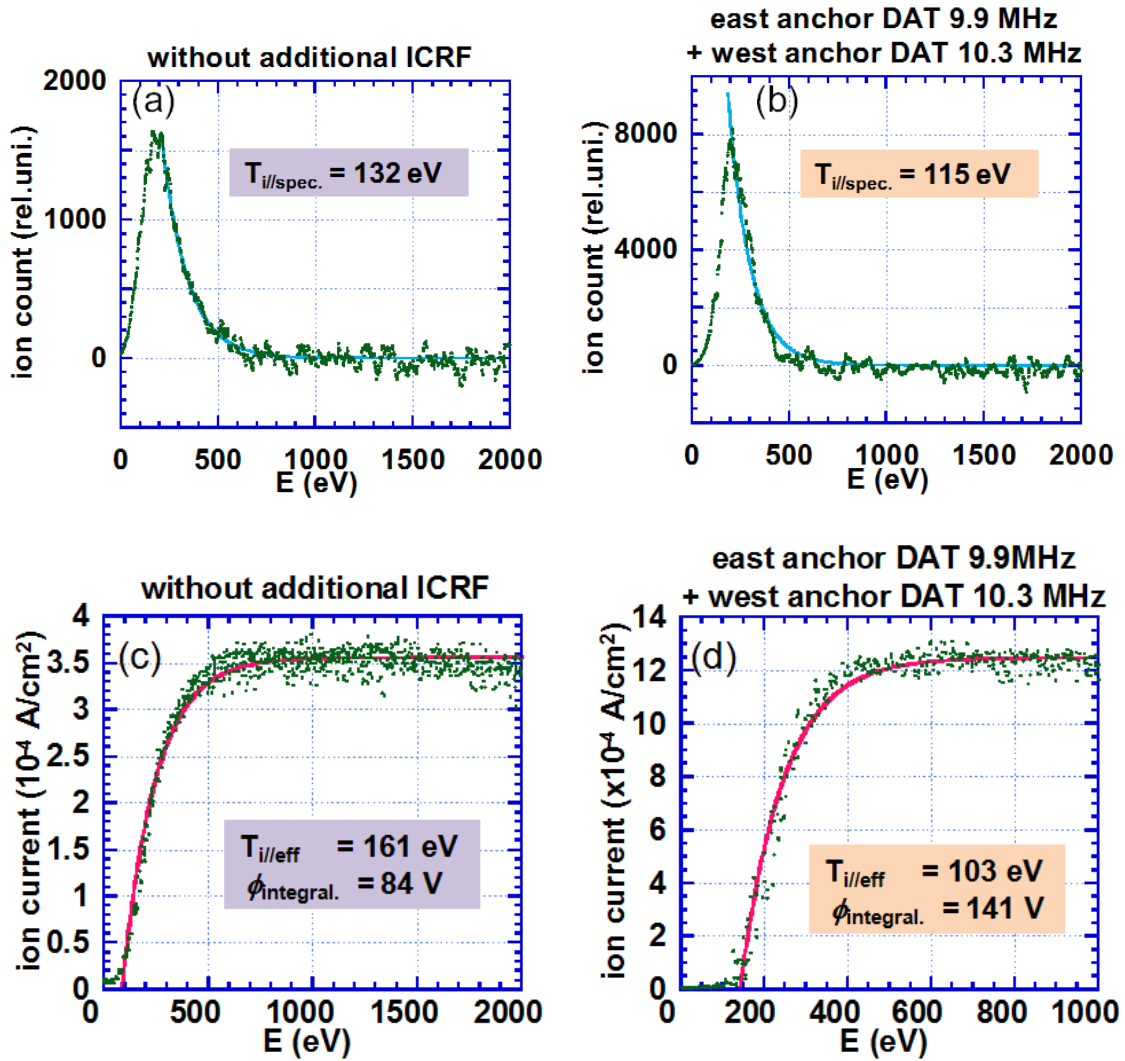


Fig. 5.17. Ion temperature and plasma potential evaluated from (a): energy spectrums without DAT (b): spectrum with DAT and gas puffing, (c): V-I curve without DAT and (d): V-I curve with east and west anchor DAT with gas puffing.

5.3.5 Effect of Plasma Potential on Particle Flux Enhancement

In the experiments of the additional ICRF heating in the anchor-cell, the result of ELIEA measurement indicated the increase of plasma potential. Because an increase of plasma potential in mirror plasma leads the degradation of ion confinement time, the change of plasma potential can enhance the particle flux. Assuming that all other parameters such as plasma temperature and density do not change, the confinement time of the ion depends on $\log R_{\text{eff}}$ [51]

where
$$R_{\text{eff}} = \frac{R}{\left(1 + \frac{q\phi}{T_i}\right)}. \quad (5-1)$$

Suppose that plasma potential ϕ has changed from 200 V to 400 V by the superimposition of ICRF, and the mirror ratio $R = 6$ and the ion energy $T_i = 400$ eV are given, equation (5-1) indicates that the ion flux will be increase by 26 %. However, the increase of the plasma potential only a part of the increase of the particle flux since the increase is usually larger than 50 % in the experiments.

5.4 Enhancement of the Particle Flux by Plasma Gun

Tandem mirror have open ends of magnetic field and therefore injection of plasma particles along the magnetic field line is possible. Actually, such injection of plasma particle is used for the generation of seed plasma by plasma guns (MPD Jet) in GAMMA 10/PDX. Due to the effect of mirror confinement at the end mirror throat, large part of the plasma particles injected by MPD Jet is reflected and several % of the particle enters into the mirror region. As listed in Table 2, the plasma generated by the MPD Jet has plasma density 100 times higher than the plasma in the central-cell. Therefore it is expected that the injection of plasma particles by the MPD Jet can enhance the particle flux at the west end-cell and the experiment of plasma injection by MPD Jet into standard ICRF heated plasma was performed [52].

Table 2 Plasma parameters in GAMMA 10/PDX experiments and the parameter of plasma injected by MPD Jet in the east end-cell [53].

	T_i (eV)	T_e (eV)	N_e (m^{-3})	Heat Flux (MW/m^2)
Main Plasma	4000	100	10^{18}	-
End-loss Flux (at the west end-cell)	400	40	10^{17}	1.0
Plasma by MPD Jet (at the east end-cell)	4	4	10^{20}	5.7

The experimental set up of the additional plasma injection experiment by MPD Jet is shown in Fig. 5.18. In the experiment, standard ICRF plasma in the main mirror confinement region is started up by the discharge

of ECRH wave instead of the MPD Jet [54]. Then, after the rump-up of standard plasma, plasma injection by the east MPD Jet was performed. The effect of the plasma injection is measured by the microwave interferometers in each cells and the ELIEA at the west end-cell.

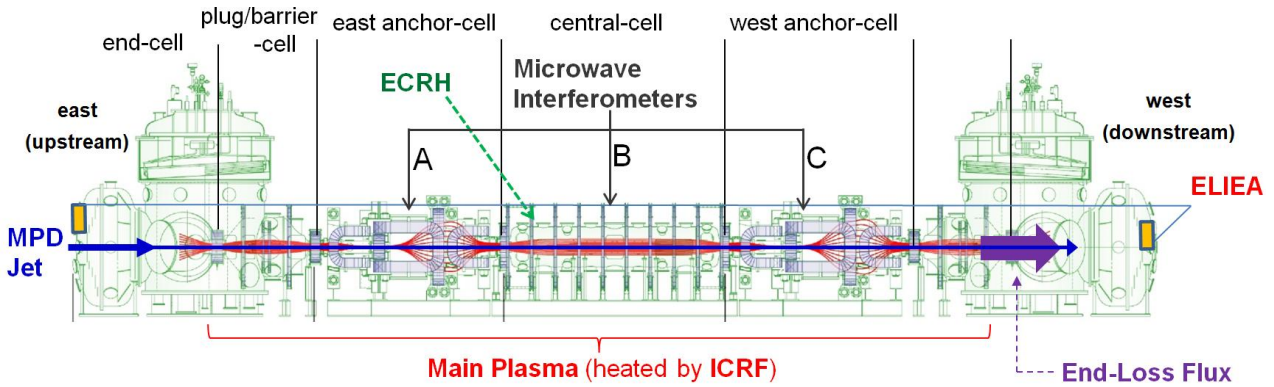


Fig. 5.18. The experimental set up of MPD Jet plasma injection.

Results of two plasma start up operations are shown in Fig. 5.19. Both diamagnetism and electron line density in the central cell showed almost same behavior and values for each operation modes except for the beginning of the discharge.

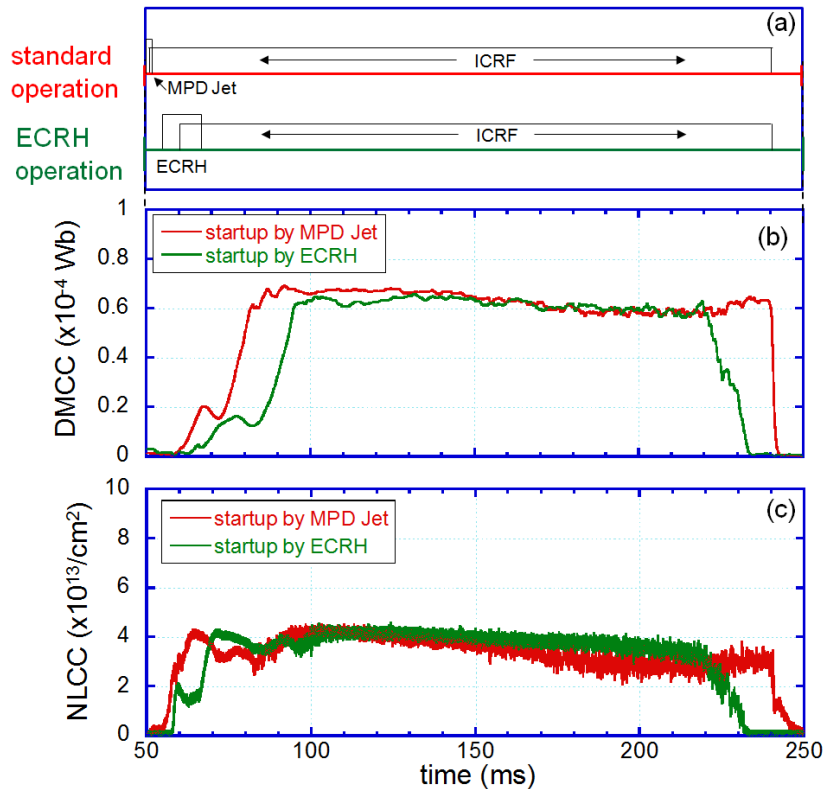


Fig. 5.19 (a): the time sequence of two plasma startup experiment, (b): time behavior of the diamagnetisms in the central-cell and (c): time behavior of the electron line density of the central-cell plasma.

For the plasma ignited by ECRH, the injection of plasma particle was performed. The time behaviors of plasma density in each cell and the end-loss ion particle flux are plotted in Fig. 5.20. By the injection of plasma particles, increase of the electron line density in each cell and the ion particle flux was observed. With the condition of the experiment, increase of the ion particle flux about 3×10^{22} particles/m²sec was obtained. It is notable that, unlike the case of SMBI experiment, the electron line density and the end-loss flux show multiple peaks ((i), (ii) and (iii)) in the time range of 100~106.5 ms.

Result of Mach probe measurement [53] showed that the drift speed of plasma injected by the MPD Jet is about 4 ~ 6 km/s. Since the total length of GAMMA 10/PDX is 27 m, it takes about 4.5 ~ 7 ms for particles to travel from upstream to downstream. The appearance of the peak (iii) at $t = 106.5$ ms can be explained as the arrival of injected plasmoid by the drift speed. For the first two peaks, effect of ionization and mirror confinement by particles' thermal speed needs to be considered. In the time range of 100~101 ms, the electron line density in each cell is increasing while the ion particle flux is not changing. The increase of the plasma density is mainly caused by the fast electrons by MPD jet injection moving with the thermal velocity. With the fast electrons, ionization is enhanced in each mirror cell and newly ionized ions will reach to the end-cell as ion particle flux after 1~2 ms from the ionization as peak (i). For the peak (ii), effect of mirror confinement is a plausible cause. That is, when the fast electrons enhanced the ionization in each cell, newly ionized particles actually can go to both west and east. Then, particles moved toward east are reflected by mirror magnetic field and start moving toward west. Since the reflected ions move longer distance, the peak of the ion particle flux appears as the peak (ii).

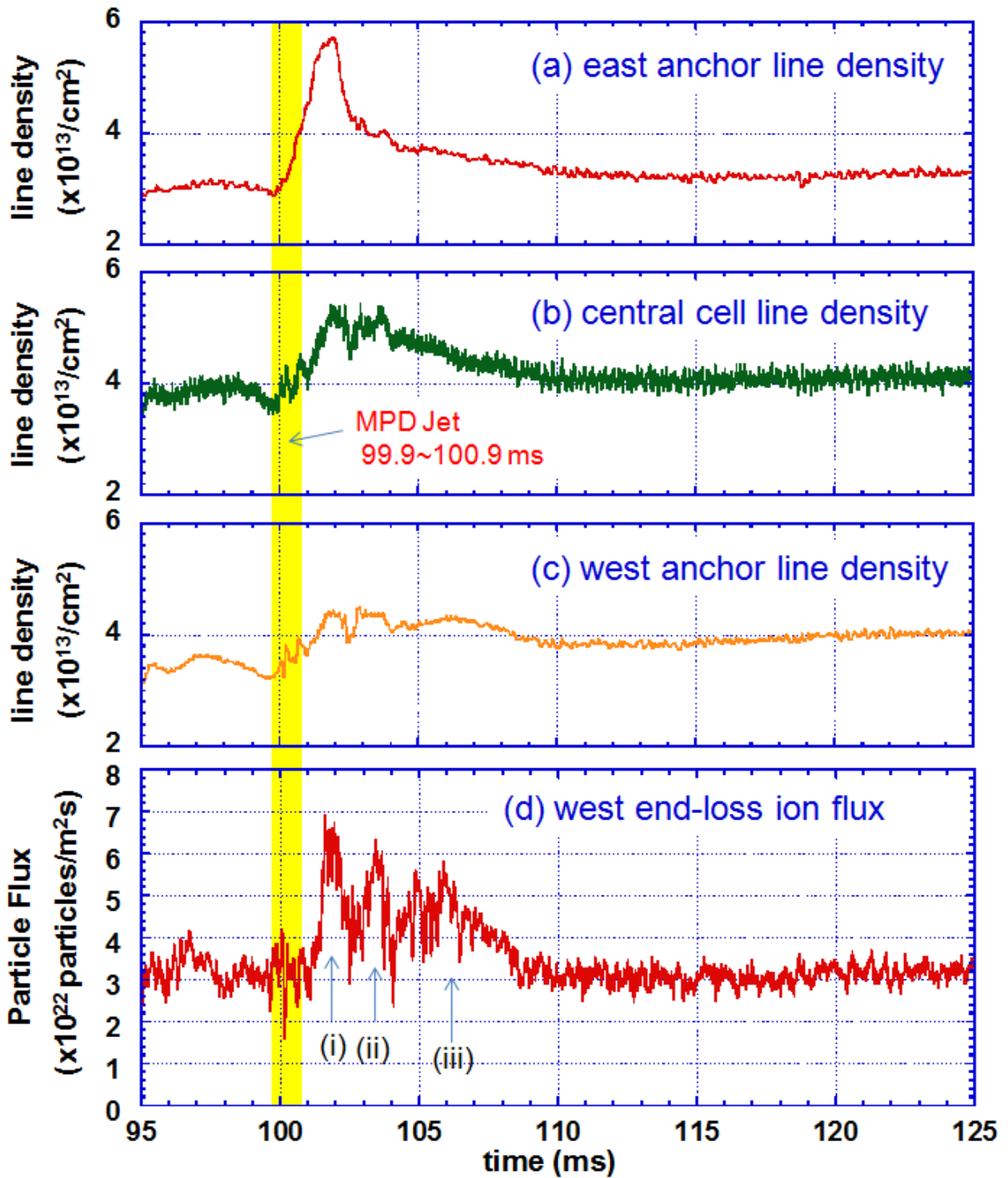


Fig. 5.20 Results of the MPD Jet plasma injection experiment. The upper three plots show the time evolution of electron line density in (a) the east anchor cell, (b) the central cell, and (c) the west anchor cell. Plot (d) is time profile of the end-loss ion current measured by ELIEA in the west end-cell.

5.5 Summary of the High Particle Flux Operations

The results of experiments for enhancing the ion particle flux are summarized in Fig. 5.21. The typical operation range of the ion particle flux for the standard operation plasma of GAMMA 10/PDX are $2\sim 6 \times 10^{22}$ particles/m²sec. Then, with adding the ICRF heating by DAT antenna, the ion particle flux higher than 8×10^{22} particles/m²sec was achieved. The range of the ion flux was largely increased and the value of 1.6×10^{23} particles/m²sec was achieved by the use of Gas Puffing and ICRF wave in both east and west anchor-cell simultaneously. Therefore, with an adequate upgrading of the power supply system and magnetic coils, the tandem mirror can generate the ion particle flux with ion temperature around 100 eV and particle flux about 1.6×10^{23} particles/m²sec in a steady state operation. It was also observed that the addition of electron cyclotron resonance heating (ECRH) and the neutral beam injection (NBI) for the central-cell plasma during the high flux operation can enhance the particle flux to the value of 2.0×10^{23} particles/m²sec. In the next chapter, effect of the plasma parameter in the anchor-cell for the enhancement of the ion particle flux will be discussed by using numerical calculations.

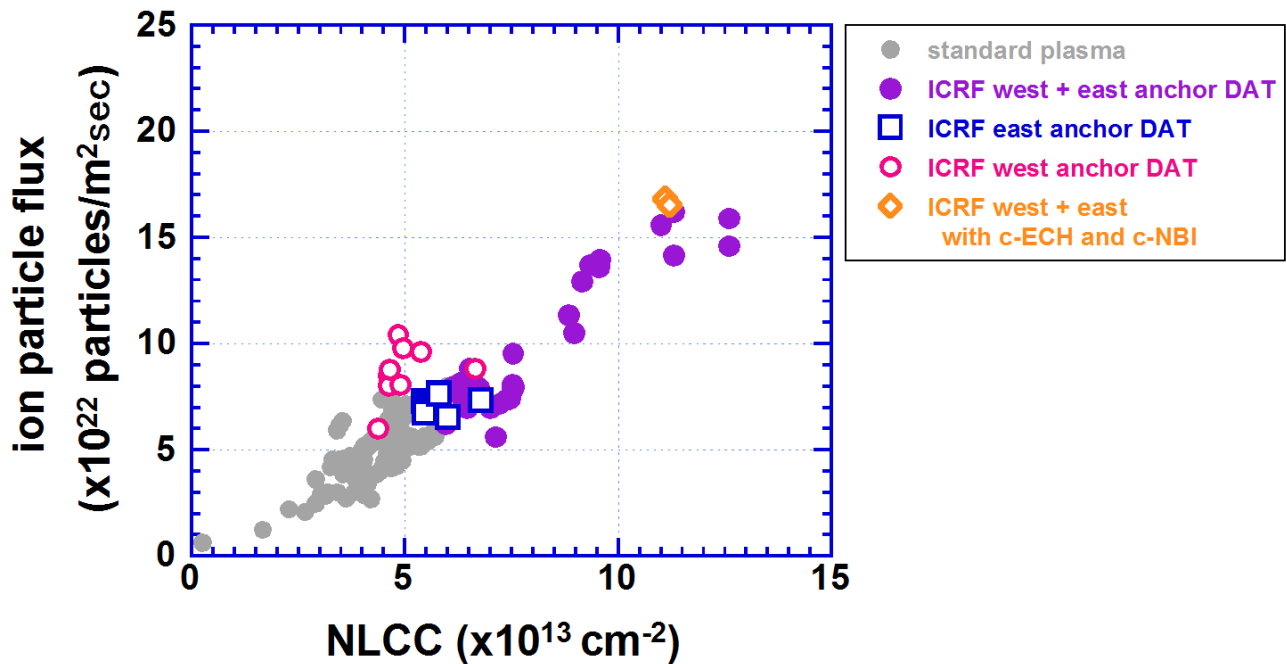


Fig. 5.21. Ion particle flux with high flux operation modes evaluated from the ELIEA measurement in the west end-cell ch1 plotted against the electron line density of the central-cell plasma.

Chapter 6 Numerical Analysis on the End-Loss Flux Production

In this chapter, the numerical study on the production of the end-loss flux in the tandem mirror is described. As discussed in the last chapter, superimposing of the ICRF heating by DAT antennas in anchor-cell showed remarkable effect of increasing the plasma density and the end-loss ion particle flux. Therefore it is obvious that the condition of plasma heating in anchor-cells is important for the production of the end-loss ion flux of the tandem mirror. On the other hand, the figure of ion particle flux plotted against the electron line density in the plasma of central-cell (Fig. 5.21) shows that the amount of ion flux strongly depends on the line density of the plasma in central-cell. It indicates that the interaction between the anchor plasma heating and the central-cell plasma plays an important role for the enhancement of the ion flux. In order to analyze the experimental results and physical mechanisms of ion flux production, a numerical simulation code for the ion flux calculation was newly developed.

6.1 Development of Flux Calculation Code

6.1.1 Original Plasma Build-Up Code

For the development of the flux calculation code, principle of the code called plasma build-up simulation code [55, 56] was used. The plasma build-up code considers a bulk-plasma in steady state and external particle sources for the bulk-plasma, such as gas injection or NBI. Then the code solves balances of plasma energy and particles and calculates the time evolution of plasma parameters produced by the external sources. In GAMMA 10/PDX, the original version of the plasma build-up code is used to simulate the change of plasma parameters during the injection of NBI in the central cell. Then the effect of NBI for the axial-loss ions can be evaluated from the density and the axial confinement time of the central cell plasma (Fig. 6.1).

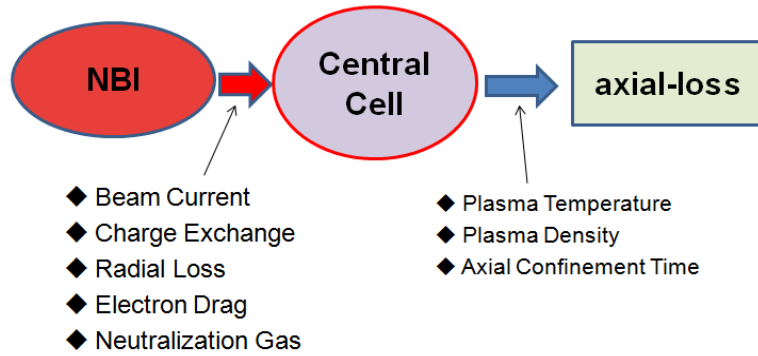


Fig. 6.1 Schematic diagram of the propagation of the effect of NBI plasma heating in the experiment of GAMMA 10/PDX.

6.1.2 Upgrade for Flux Calculation Code

In the experiment of anchor ICRF heating by DAT antennas, wave of ICRF is superimposed to the mid-plane of the anchor-cell. Effect of the ICRF heating should appear not only in the end-loss flux, but also in the plasma parameters in other cells. In order to reproduce the effect of ICRF heating by anchor DAT antenna, the code was remodeled. In the new code, calculation region was extended to include anchor regions as shown in Fig. 6.2. In this case, understanding of the interaction among mirror cell (particle transport) is needed to evaluate the end-loss flux.

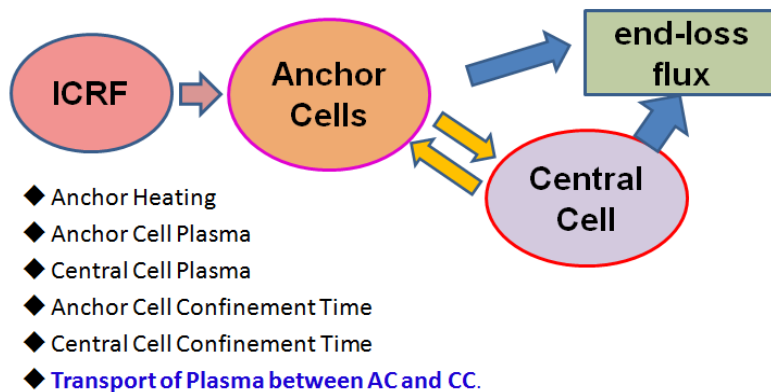


Fig. 6.2 Schematic drawing of the propagation of the effect of ICRF heating during the experiment of GAMMA 10/PDX.

For simplification, a calculation region of the flux calculation code was defined in the magnetic flux tube that has a cross-sectional area of electrostatic probe at $z=1030$ cm. In order to evaluate the particle transport between the central and anchor-cells, the volumes of the magnetic flux tube was calculated. In mirror magnetic fields, the strength of the magnetic field changes largely along the z -axis. In such case, the cross-sections of magnetic flux tube also change along the z -axis and therefore it is difficult to evaluate the volume of the magnetic flux tube [57, 58]. For the volume calculation of magnetic flux tube, the idea of

effective mirror length is applied. As described in Fig. 6.3, the volume of the magnetic flux tube can be calculated by considering the cylinder with its cross-section A_0 and length $L_{\text{effective}}$. Here, since the relationship between the cross-section and the magnetic field strength is given as equation (6-1-1),

$$A_0 B_0 = A_{\text{throat}} B_{\text{throat}} = S_{\text{Probe}} B_{\text{Probe}} \quad (6-1-1)$$

where S_{Probe} is the surface area of the ESP and B_{Probe} is the magnetic field strength at the position of ESP ($z=1030$ cm). The effective mirror length $L_{\text{effective}}$ is given as (6-1-2). as follow,

$$L_{\text{effective}} = B_0 \int \left(\frac{1}{B(z)} \right) dz \quad (6-1-2)$$

In equation (6-1-2), the interval of the integration corresponds to the axial distance from the throat to the other mirror throat. Then, by substituting A_0 by $(S_{\text{Probe}} \times B_{\text{Probe}} / B_0)$, the volume of the magnetic flux tube that corresponds to the measurement surface of the ESP can be calculated as $L_{\text{effective}} \times (S_{\text{Probe}} \times B_{\text{Probe}} / B_0)$. By using this method, the volume of the magnetic flux tube in the central-cell and the anchor-cells are calculated and applied for the code.

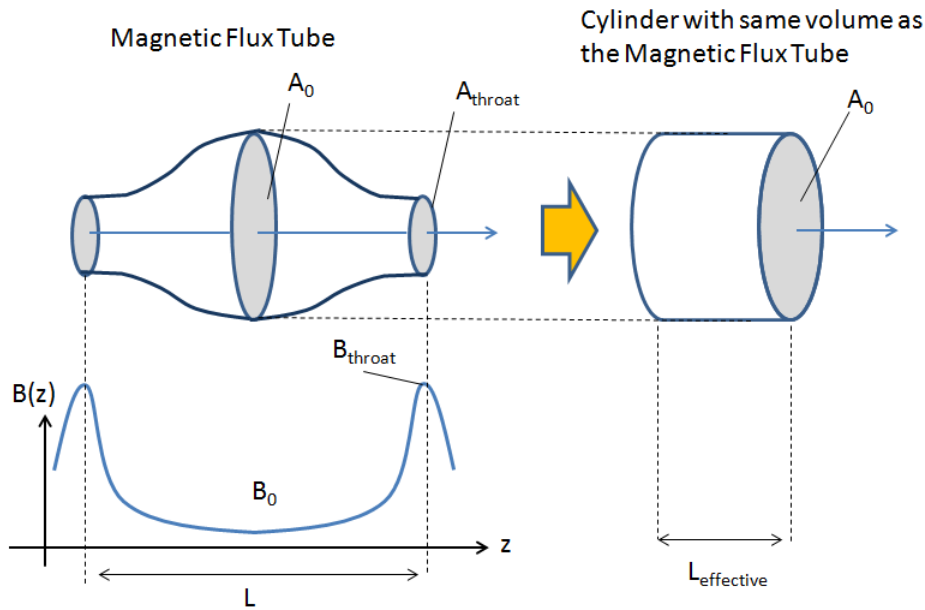


Fig. 6.3 Schematic drawing of the magnetic flux tube and the cylinder of the same volume as the magnetic flux tube of a mirror magnetic field.

6.1.3 Calculation of the Cell-To-Cell Transport of Plasma Particles

In chapter 5, it was introduced that the superimposing of the ICRF heating by the DAT antenna increases the line density of the plasma in the central-cell and anchor-cells. Since the wave of ICRF heating is only applied to the cell where DAT locates, the increase of the line density in the central-cell and the other anchor-cell should be mainly caused by the interactions between the mirror cells such as transport of plasma particles. In order to simulate the interactions, the idea of cell-to-cell transport was introduced. In the cell-to-cell transport, the transport of particle among the mirror cell is defined from the confinement-time of each cell. As shown in Fig. 6.4, the maximum strength of the mirror magnetic field is 3 Tesla at the inner and outer mirror throats while the minimum is 0.4 Tesla at the mid-plane of the central-cell. In this case, the total mirror ratio of GAMMA 10/PDX can be considered as $R_{\text{total}} = 7.5$. On the other hand, as an individual mirror cell, the central-cell has mirror ratio $R_{\text{central}} = 5$ and the anchor-cells have $R_{\text{anchor}} = 3.3$. The difference of the mirror ratio makes the difference of the confinement time of plasma particles. Especially, it is predicted by the theoretical calculation that most particles of end-loss plasma locate at the boundary of the loss-cones since the particles are kicked to the loss-cones mainly by the small angle scattering. Therefore particles escaped from the central-cell mirror of 2 Tesla are likely to be still reflected by the 3 Tesla mirror at the inner throat of GAMMA 10/PDX. Then the particle can travel between the 3 Tesla mirror throats freely and such travelling particle can contribute to the density of anchor-cells and central-cell until the particle escapes from the 3 Tesla mirror. By investigating the travelling particle from each mirror cell, the interactions between the cells can be analyzed. In the code, the axial confinement time of the ion is defined by the following equation which is based on the classical collision theory [59].

$$\tau_{\text{theoretical}} = 0.78 \times \tau_{\text{ii}} \log(R), \quad (6-1-3)$$

where

$$\tau_{\text{ii}} = \frac{6.6 \times 10^{-3} \times T_i^{\frac{3}{2}}}{N_i \times (10^{-20}) \times Z_i^4 \times \ln \Delta}.$$

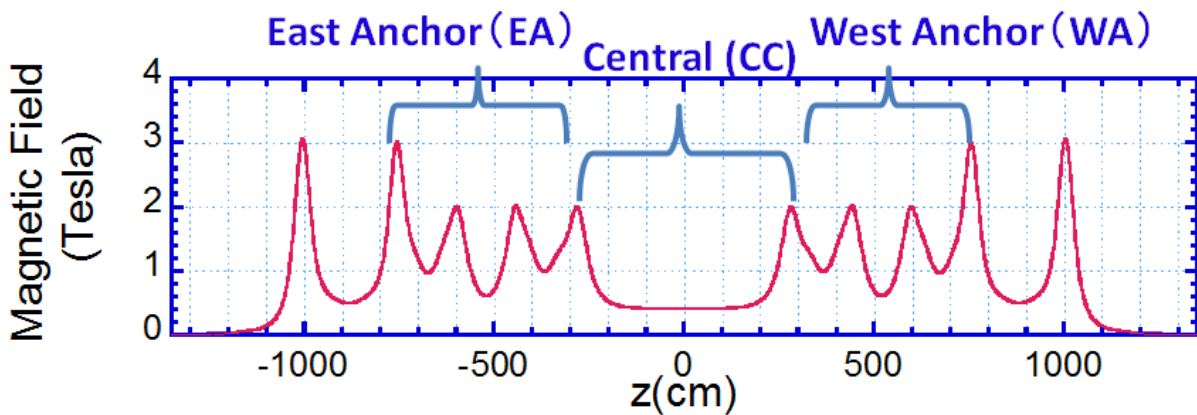


Fig. 6.4 Strength of the magnetic field of GAMMA 10/PDX plotted against z-axis.

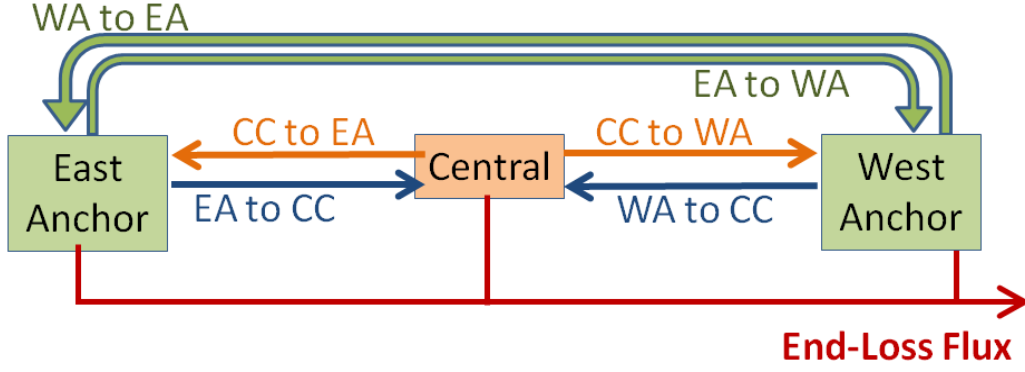


Fig. 6.5 Schematic diagram of possible contribution passes of a particle for each cell of tandem mirror.

The image shown in Fig. 6.5 is a schematic diagram of particles' contribution passes that are considered in the new calculation. The essential equations to determine the cell-to-cell transport are follows;

$$N_{CC} = n_{CC} \times \alpha_{CCtoCC} + n_{EA} \times \alpha_{EAtoCC} \times \left(\frac{V_{EA}}{V_{CC}}\right) + n_{WA} \times \alpha_{WAtoCC} \times \left(\frac{V_{WA}}{V_{CC}}\right) , \quad (6-1-4)$$

$$n_{CC} \times V_{CC} + n_{EA} \times V_{EA} + n_{WA} \times V_{WA} = N_{CC} \times V_{CC} + N_{EA} \times V_{EA} + N_{WA} \times V_{WA} , \quad (6-1-5)$$

$$\alpha_{CCtoEA} = \frac{(\tau_{G10} - \tau_{CC}) \times \left(\frac{L_{EA}}{L_{CC} + L_{EA} + L_{WA}}\right)}{\tau_{G10}} , \quad (6-1-6)$$

$$\alpha_{CCtoCC} = \frac{\tau_{CC}}{\tau_{G10}} + \frac{(\tau_{G10} - \tau_{CC}) \times \left(\frac{L_{CC}}{L_{CC} + L_{EA} + L_{WA}}\right)}{\tau_{G10}} . \quad (6-1-7)$$

$$\text{where } n_{CC} = S_{CC} \times \tau_{G10} . \quad (6-1-8)$$

Here, the observed density N in each cell is the result of cell-to-cell transport. When we measure the density of the central-cell plasma, the measured N_{cc} already includes the particle imported from the east or west anchor cells as in Fig. 6.5. Thus we defined the effective plasma density n in each cell. Here, the effective density n represents the plasma density before the cell-to-cell transport while the observed density N represents the density after the transport. Since the total number of particle (N_{total}) is same in both before and after the transport, the effective density and the observed density satisfy equation (6-1-4). The particle's mirror confinement time in the central-cell is defined as τ_{CC} and that in the total GAMMA10/PDX mirrors (east anchor-cell, central-cell and west anchor-cell), τ_{G10} . The term α is determined by the mirror confinement time τ and the length of the mirror cell L as equations (6-1-5) and (6-1-6). The α substitutes the rate of particle's dwell time in a specific cell with respect to the particle's total confinement time in the

machine. For example, if $\alpha_{CCtoCC} = 0.60$ is given, it means that a particle newly trapped in the central-cell will spend 60% of its total mirror confined time (τ_{G10}) in the central-cell and will spend 40% in other cells. In this calculation model, the effective density n corresponds to the plasma particle source S ($m^{-3}s^{-1}$) multiplied by the total confinement time τ_{G10} (sec).

6.1.4 Particle Balance Equations

The balance equations of the particles used in the code are shown in below. In the code, “warm ion” means the ions of the plasma without the ICRF heating by DAT antenna and “hot ion” means the ions produced by the additional ICRF heating by the DAT antennas in anchor-cell. In the calculation, injection of hot ion to the anchor-cell is used to simulate the change of plasma parameters made by the additional ICRF heating.

- Warm ion;

$$\begin{aligned} \frac{dN_{CCw}(t)}{dt} &= N_{CC0}(t)[N_{CCh}(t)\{\langle \sigma v \rangle_{hpi} + \langle \sigma v \rangle_{cx}\} + N_w(t)\langle \sigma v \rangle_{wpi} + \{N_{CCw}(t) + N_{CCh}(t)\}\langle \sigma v \rangle_{ei}] \\ &+ \frac{1}{\tau_{G10}} \left\{ -n_{CCw}(t) \cdot (1 - \alpha_{CCtoCC}) + n_{EAw}(t) \cdot \alpha_{EAtoCC} \times \left(\frac{V_{EA}}{V_{CC}} \right) + n_{WAw}(t) \cdot \alpha_{WAtoCC} \times \left(\frac{V_{WA}}{V_{CC}} \right) \right\} \\ &+ S_{CCbg} - \frac{N_{CCw}(t)}{\tau_{G10}} - \frac{N_{CCw}(t)}{\tau_{radial}}. \end{aligned} \quad (6-1-9)$$

- Hot ion;

$$\begin{aligned} \frac{dN_{CCh}(t)}{dt} &= S_{ICRF} - N_{CC0}(t)N_h(t)\langle \sigma v \rangle_{cx} \\ &+ \frac{1}{\tau_{G10h}} \left\{ -n_{CCh}(t) \cdot (1 - \alpha_{hCCtoCC}) + n_{EAh}(t) \cdot \alpha_{hEAtoCC} \times \left(\frac{V_{EA}}{V_{CC}} \right) + n_{WAh}(t) \cdot \alpha_{hWAtoCC} \times \left(\frac{V_{EA}}{V_{CC}} \right) \right\} \\ &- \frac{N_{CCh}(t)}{\tau_{G10h}} - \frac{N_{CCh}(t)}{\tau_{radial}}. \end{aligned} \quad (6-1-10)$$

- Neutral;

$$\begin{aligned} \frac{dN_{CC0}(t)}{dt} &= +(\gamma - 1)N_{CC0}(t)\{N_{CCh}(t)\langle \sigma v \rangle_{cx} + N_{CCw}(t)\langle \sigma v \rangle_{cx}\} - N_{CC0}(t)[N_{CCh}(t)\langle \sigma v \rangle_{pi} \\ &+ N_{CCw}(t)\langle \sigma v \rangle_{pi} + \{N_{CCw}(t) + N_{CCh}(t)\}\langle \sigma v \rangle_{ei}] - \frac{N_0(t)}{\tau_{pump}} + Q_{CCbg} + \frac{N_{CCw}(t) + N_{CCh}(t)}{\tau_{radial}}. \end{aligned} \quad (6-1-11)$$

Here, $N_{CCw}(t)$, $N_{CCh}(t)$, $N_{CC0}(t)$ are the densities of warm ions, hot ions and neutrals in the central-cell

respectively. Terms $\langle\sigma\nu\rangle_{cx}$, $\langle\sigma\nu\rangle_{pi}$, $\langle\sigma\nu\rangle_{ei}$ denote the rate coefficients of charge exchange, proton ionization and electron ionization. The term τ_{G10} and τ_{G10h} are the total axial confinement time for the warm ions and hot ions. τ_{pump} represents the characteristic time of vacuum pumps (0.33 s) and τ_{radial} represents the radial loss time of the ions (5 s). The γ is the coefficient of gas recycling at the mid-plane of the central-cell. S_{CCbg} is the background flow of the warm ion and Q_{CCbg} is the background flow of gas. The amount of background flow are determined to make the left hand term of equation (6-1-9) and (6-1-11) zero at $t = 0$. The notation of S_{ICRF} means the source term of hot ions made by the additional ICRF heating in anchor-cell. In calculation, balance equations of the east anchor-cell and the west anchor-cell are calculated in the same way as the central-cell.

6.1.5 Energy Balance Equations

The balance equations of the energy in the code are shown as below.

- Warm ion;

$$\begin{aligned} \frac{dW_{CCw}(t)}{dt} = & Q_{CCbg}^w - W_{CCw}(t)N_{CC0}(t)\langle\sigma\nu\rangle_{cx} - \frac{\frac{3}{2}N_{CCw}(t)\{T_{CCw}(t) - T_{CCe}(t)\}}{\tau_{CCed}^{warm}} \\ & + \frac{1}{\tau_{G10}} \left\{ -w_{CCw}(t) \cdot (1 - \alpha_{CCtoCC}) + w_{EAw}(t) \cdot \alpha_{EAtoCC} \times \left(\frac{V_{EA}}{V_{CC}}\right) + w_{WAw}(t) \cdot \alpha_{WAtoCC} \times \left(\frac{V_{WA}}{V_{CC}}\right) \right\} \\ & - \frac{W_w(t)}{\tau_E^{warm}} - \frac{W_w(t)}{\tau_{radial}}, \end{aligned} \quad (6-1-12)$$

- Electron;

$$\frac{dW_{CCe}(t)}{dt} = Q_{CCbg}^e + \frac{\frac{3}{2}N_{CCh}(t)\{T_{CCh}(t) - T_{CCe}(t)\}}{\tau_{CCed}^{hot}} + \frac{\frac{3}{2}N_{CCw}(t)\{T_{CCw}(t) - T_{CCe}(t)\}}{\tau_{CCed}^{warm}} - \frac{W_{CCe}(t)}{\tau_E^{electron}}, \quad (6-1-13)$$

where $W_{CCw}(t)$ is the energy density of warm ions, $W_{CCe}(t)$ is the energy density of the electrons, $T_{CCw}(t)$ and $T_{CCh}(t)$ shows the perpendicular temperature of warm and hot ions and $T_{CCe}(t)$ is the electron temperature of the central-cell plasma. The term τ_{CCed}^{warm} , τ_E^{warm} and $\tau_E^{electron}$ are the electron drag time, warm ion energy confinement time and electron energy confinement time respectively. The background flow of energy for warm ion is Q_{CCbg}^{warm} and for the electron is $Q_{CCbg}^{electron}$. The amount of background energy flow is determined to satisfy the left hand term of equation (6-1-12) and (6-1-13) become zero at $t = 0$. The energy balance of the east and west anchor-cells are also calculated in the same form of balance equations.

For the calculation, five balance equations are defined for three cells. Then for the fifteen equations, the initial condition of plasma parameters and the condition of ICRF heating are applied and the time change of

the plasma parameters are numerically solved as simultaneous differential equations of time.

6.2 Evaluation of Axial Confinement Time

Since the equation (6-1-3) is considering an ideal simple mirror field, the confinement time will not fit for the experimental confinement time of the complex mirror field of the tandem mirror machine. Thus, in order to evaluate the experimental confinement time, calculation of the ion particle flux was performed with the typical plasma parameters of standard operation

($T_{iCC} = 3$ keV, $T_{iAC} = 1.5$ keV and $T_e = 40$ eV). It is assumed that the plasmas in anchor mirror cells have the same electron line density as the central-cell plasma ($1.0 \sim 7.0 \times 10^{13} \text{ cm}^{-2}$) and plasma in every cell has a parallel ion temperature of 300 eV. Then, the results of calculation were compared with the experimental value of the ion particle flux measured by ESP. As in Fig. 6.6, calculated ion particle flux by the model of classical mirror confinement time is compared with the experimental values. The result with simple theoretical confinement time is 4.7 times longer than the experimentally evaluated confinement time. It means that the actual confinement time of GAMMA 10/PDX experiment is smaller than the classically theory model due to the miscellaneous factors such as instabilities.

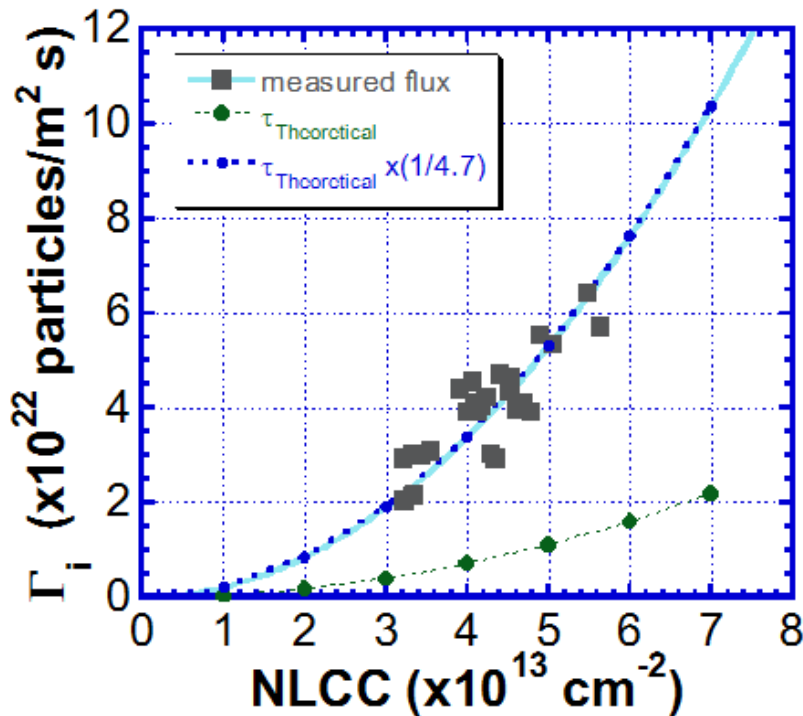


Fig. 6.6 Comparison of ESP measurement and the calculation of ion flux by classical collision theory of mirror confinement time.

Next, cell-to-cell transport of the plasma particle was tested by applying the artificial plasma density source S_{ICRF} into east anchor-cell. The result of the transport test is shown in Fig. 6.7. During the artificial increase

of plasma density in east anchor, plasma density in the central-cell and the west anchor-cell were increased. It is confirmed that the increase of plasma density made in the east anchor-cell propagated to other cells by the process of cell-to-cell transport in the code

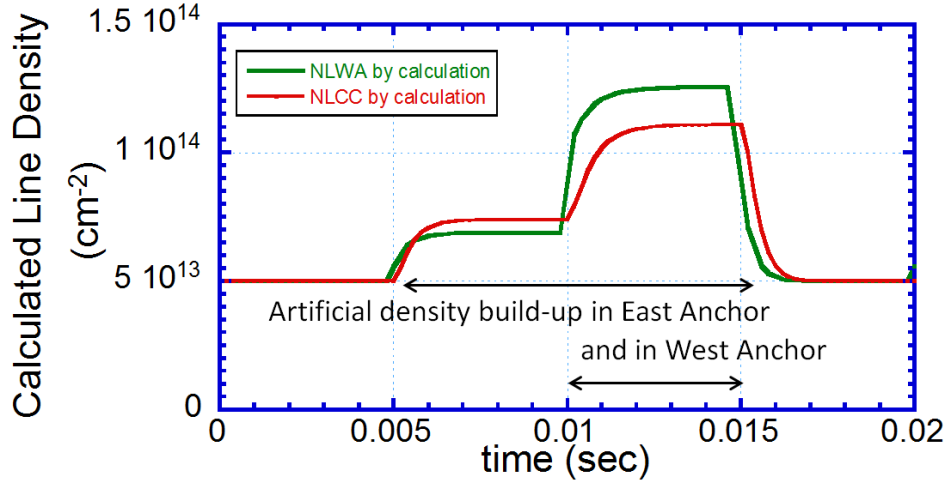


Fig. 6.7 Result of test calculation for the transport of the plasma density from the east anchor-cell to other cells by cell-to-cell transport. An artificial density source S_{ICRF} is inputted to the anchor-cell.

6.3 Analysis of the End-Loss Ion Flux by the Code

Figure 6.8 shows the electron line densities and particle flux measured in the high flux experiments in chapter 5. The initial plasma parameters for the calculation, such as plasma density and temperatures are given from the measurement and the increase of the plasma density in anchor-cell was simulated by adding the artificial change of plasma source S_{ICRF} that correspond to the change observed during the additional ICRF heating. We defined three cases of calculations in order to simulate the present experiments. Case (A) simulates the standard operation mode plasma of GAMMA 10/PDX without new ICRF. In case (B), plasma heating by east anchor antenna (EA) and west anchor antenna (WA) are simulated by increasing the plasma density in east and west anchor-cells. In case (C), only the plasma density in east anchor-cell was increased in order to reproduce the case of the additional ICRF heating by east anchor antenna only.

Figure 6.9 shows the results of numerical calculation by the upgraded plasma build up code. Case (A) is the initial condition case without an additional ICRF heating and the plasma density is given from the typical experimental results. In condition (B), the artificial plasma source S_{ICRF} was applied to both east and west anchor-cells as the simulation of simultaneous ICRF heating of east and west anchor region. The plasma source S_{ICRF} was applied to east anchor-cells in condition (C), as the simulation of ICRF heating of east anchor region. The amounts of S_{ICRF} are determined to reproduce the density of the anchor-cell where the additional heating is applied. From the calculations, qualitative behavior of the plasma density in each cell was roughly reproduced although there is a gap between the calculation and the experimental results shown

in Fig. 6.8. Especially, the increase of the NLCC is under estimated in both cases and the increase of the particle flux is over estimated in both (B) and (C).

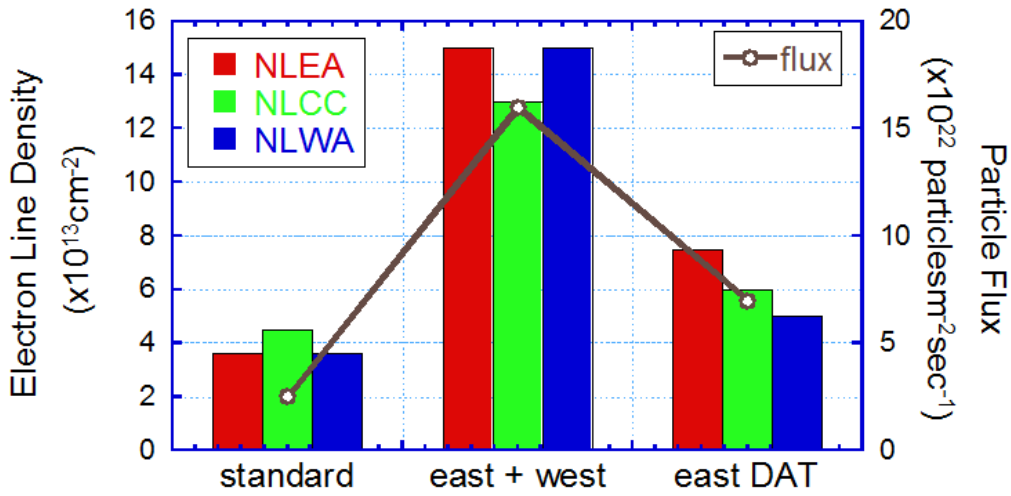


Fig. 6.8 Experimental results of the electron line densities and particle flux during the anchor ICRF heating experiments.

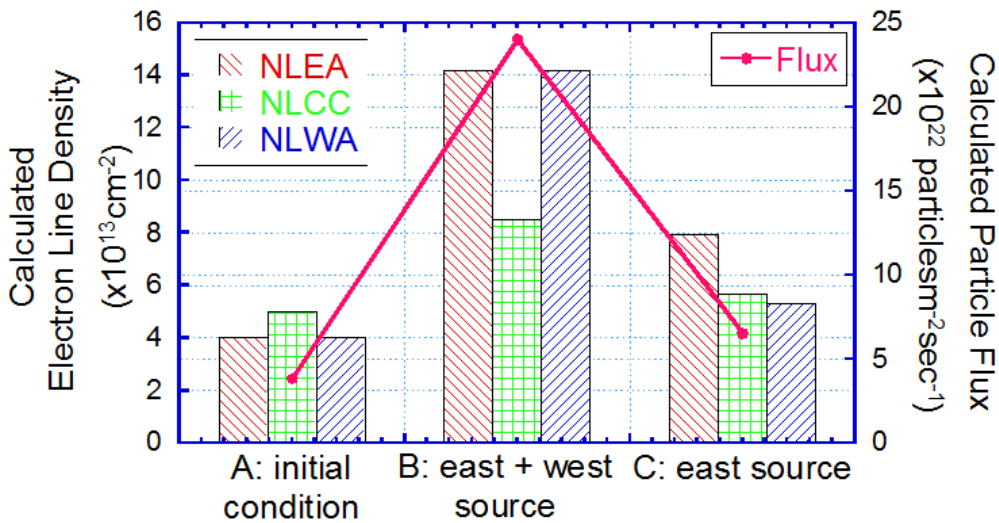


Fig. 6.9 Results of calculations reproducing the plasma density in anchor ICRF heating experiments; A: initial condition (standard experiment), B: S_{ICRF} applied to both east and west anchor cells C: S_{ICRF} applied to east anchor-cell to simulate ICRF heating in EA.

Then, the balance of the effective density source n_{CC} , n_{EA} and n_{WA} was reconsidered by using the ratio of amount of ionizations between the central-cell and anchor-cells based on the $H\alpha$ line emission [60]. According to the result of $H\alpha$ measurement, ionization quantity in the anchor-cell is about 1/10 of that in the central-cell. In the current calculation model, the balance of the source is determined by the confinement time and the actual length of the mirror cells and the ionization in the anchor-cell is about 1/4 of the central-cell. In the calculation of Fig. 6.10, values of α are artificially changed in order to satisfy the balance

of ionization source between the anchor-cell and the central-cell equals to 1: 10 and the balance of electron line density in each cell as shown in the case (D) in Fig. 6.10. Cases (E) and (F) are the results of calculations plasma sources S_{ICRF} in cases (B) and (C) respectively. However, in these cases the transport of the particle is based on the condition of the case (D). In these cases, the plasma density is more localized to the anchor-cells since the transport of particles into the anchor region is enhanced in the condition. The calculation is still far from the experimental result and therefore it is assumed that behavior of the plasma density during the ICRF heating into anchor-cell is affected not only by the mirror confinement, but also the particle trap by the ICRF wave or plasma potentials.

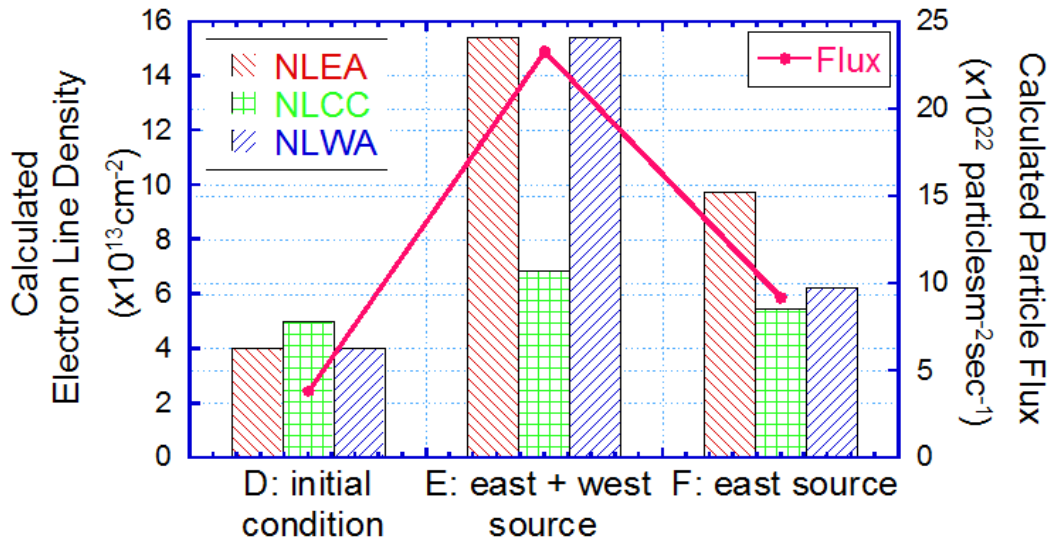


Fig. 6.10 Results of calculations reproducing the plasma density in anchor ICRF heating experiments with modulated source balance; D: initial condition (standard experiment), E: S_{ICRF} applied to both east and west anchor cells, F: S_{ICRF} applied to east anchor-cell to simulate ICRF heating in EA.

6.5 Discussion

Another plausible cause of the gap between the calculation and experiment is the change of axial confinement time of ion. In Fig. 6.11, plot of the measured ion particle flux and the fitting curves for the plot with models of parabolic curve and linear slope are shown. The parabolic curve is obtained from the particle flux measurements in standard operation mode shown in Fig. 4.13. In the standard operations, the dependency become parabolic since the process of the ion particle loss from the mirror is determined by the collision time of the ions as in equation (6-1-3). On the other hand, unlike the calculation results and the particle flux in the standard operations (operation with ICRF1 and ICRF2 only), the ion particle flux measured in the high flux experiments (with additional ICRF in anchor region) are not following the parabolic dependency and the plots show linear dependency of the ion flux to the NLCC. Such change of the dependency is predicted in the numerical study of mirror confinement time [61]. In the plasma confinement in mirror magnetic field, the axial ion confinement time is determined by the mirror ratio and ion collision

time when the collision time is long enough in comparison with the transit time of ion. The transient time is defined as following equation;

$$\tau_{\text{transit}} = \frac{L}{v_{i//}} \quad , \quad (6-1-14)$$

where L is the length of the mirror system. The τ_{transit} divided by the collision time τ_{ii} indicate the collision frequency of transit ions. In equation, the collision rate is described as follows;

$$\frac{\tau_{\text{transit}}}{\tau_{ii}} \propto \frac{N_i}{(T_{i//})^2} \quad . \quad (6-1-15)$$

The collision rate ($\tau_{\text{transit}}/\tau_{ii}$) calculated for the plasma parameter of GAMMA 10/PDX is shown in Fig. 6.12. In the standard experiments, plasma density is around $2 \times 10^{18} \text{ m}^{-3}$ and typical ion temperature is 200~400 eV. Therefore the collision rate of GAMMA 10/PDX plasma is small. On the other hand, plasma density is increased and the ion temperature is decreased in the high flux operations. In this case, it is predicted that the collision rate is not negligible and the confinement time of the ion is determined by the transit time of the ions in loss cones;

$$\tau_{i//} \propto \frac{\sqrt{\pi} \times R \times L}{\sqrt{T_{i//}}} \quad . \quad (6-1-16)$$

In the high collision rate case, ion confinement time is determined by equation (6-1-16) and therefore the value of the end-loss ion flux depends linearly on the density of plasma as seen in Fig. 6.11. These results indicate that the change of particle loss process must be considered in the calculation code in order to explain the high flux experiments.

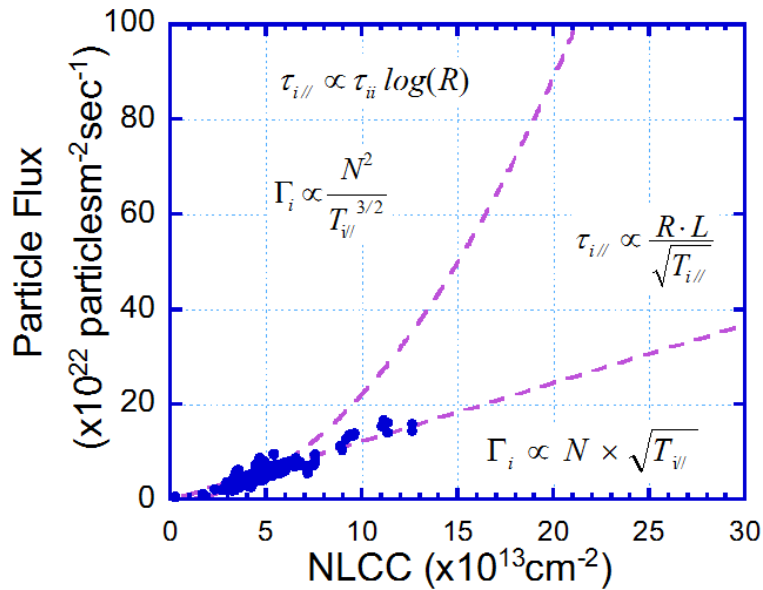


Fig. 6.11. Measured particle flux and fitting curves plotted against NLCC.

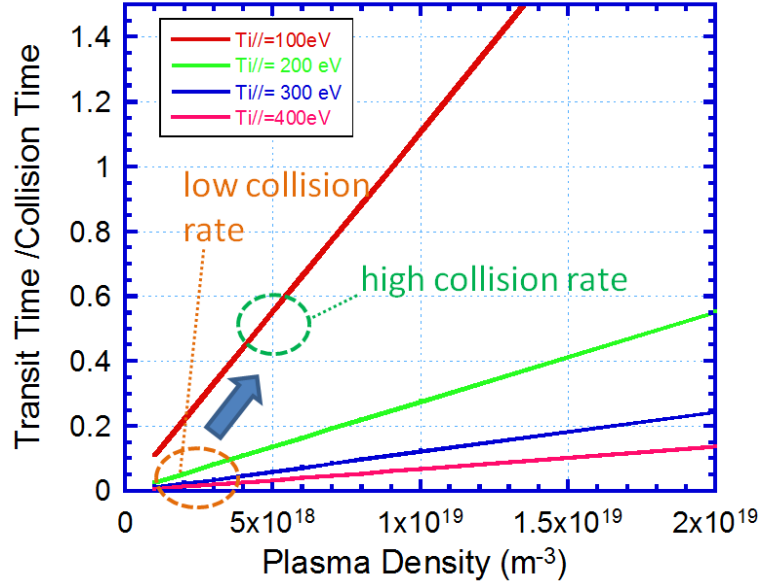


Fig. 6.12. transit time of the ion divided by the collision time of the ion calculated for the parameters of GAMMA 10/PDX mirror plasma.

From the view point of divertor simulation study, higher particle flux of the tandem mirror is more favorable. If the plasma is in high collision rate, density of the plasma needs to be increased 10 times higher in order to enhance the ion particle flux by an order. On the other hand, if the particle flux depends on the plasma density with parabolic function, increase of the plasma density by only 3~4 times is required to enhance the ion particle flux by 10 times. Although the parabolic dependency of the ion particle flux on the plasma density is attractive, we cannot expect the parabolic increase of the particle flux in high plasma density range since the gradual increase of collision rate is the cause of the parabolic dependency. In high density range, collision rate becomes extremely high and the particle flux will depend on the plasma density linearly.

Equation (6-1-17) is the relationship between the ion particle flux and the plasma density with high collision rate.

$$\Gamma_i \propto \frac{N \times \sqrt{T_{i//}} \times (1 + \frac{q\phi}{E_i})}{R \times L} \quad (6-1-17)$$

Here, the electrostatic potential of the mirror plasma ϕ and the change of the mirror ratio due to the potential described in Eq. (5-1) are taken into account. The dependency of the ion particle flux on the plasma density with the ratio of Eq. (6-1-17) is plotted in Fig. 6.13. It is found that the increase of electrostatic potential of the plasma can increase the ion particle flux largely. Finally, it can be concluded that the collision rate of the ion and the electrostatic potential of the mirror confined plasma is very essential to the discussion of the behavior of the end-loss ion particle flux. For the further enhancement of the ion particle flux, the effect of the plasma potential should be noted.

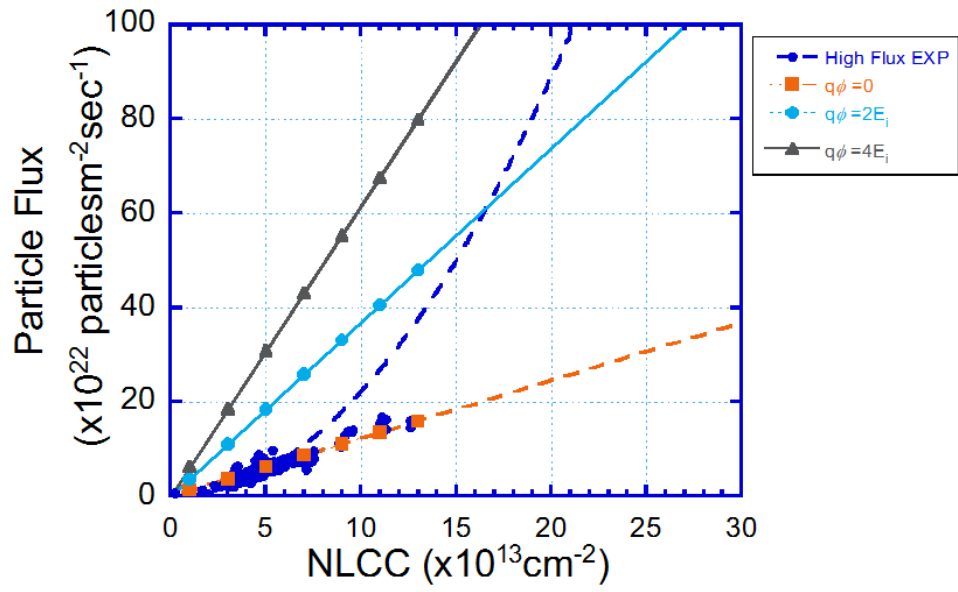


Fig. 6.13. Measured particle flux and the slopes of particle flux calculated by changing the value of plasma potentials plotted against NLCC.

Chapter 7 Conclusion

From the view point of divertor simulation experimental study, the end-loss flux of the large tandem mirror device GAMAM 10/PDX was investigated. By using the diagnostic tool called ELIEA, characteristics of the end-loss ion flux was precisely measured. The results were also analyzed by numerical calculations and the following findings are obtained.

1. The end-loss ion flux have high parallel ion temperature with the range of ion temperature 100~400eV which is useful for the research of divertor simulation experiment. In addition, the strong controllability of the ion temperature of the end-loss flux by controlling the heating power of ICRF was confirmed.
2. The large plasma radius of GAMMA 10/PDX is also observed in the end-loss plasma flux and it was found that the end-loss flux typically has full-width half maximum of 10 cm.
3. Radial profiles of the parallel ion temperature of the ion flux were found to be flat, even in the condition of large gas injection from SMBI.
4. The energy distribution of the end-loss ion flux revealed that the distribution is mainly composed of Maxwellian distribution. However, the distribution is not the pure Maxwellian and the double component of Maxwellian distribution is required in the operation of high power plasma.
5. For the enhancement of the ion particle flux, the superimposing of additional ICRF heating in anchor-cell is found to be very effective. By the improvement of the antenna configuration, ion particle flux larger than 1.6×10^{23} particles/m²s was achieved.
6. Increase of ion particle flux and the behavior of the plasmoid in the tandem mirror were first observed in the experiment of plasma particle injection along the axial direction by using the MPD Arcjet.
7. By using the flux calculation code, experimental results of anchor ICRF heating for the enhancement of end-loss ion particle flux was analyzed. It was found that the transport of the plasma density during the additional anchor ICRF experiment is not only determined by the mirror confinement, but also the plasma potentials.
8. From the experimental and numerical analysis, change of the particle loss mechanisms of the tandem mirror during the high flux experiment was indicated. It was found that to increase the plasma potential is important for the effective enhancement of the end-loss ion flux.

Concluding Remarks

In this thesis, we performed the analysis of the end-loss flux of the tandem mirror GAMMA 10/PDX both experimentally and numerically. It was observed that the tandem mirror have remarkable features of performing divertor simulation studies. Firstly the parallel ion temperature of the end-loss ion flux is several hundred eV and the temperature can be controlled in the range of 100~450 eV by changing the power of ICRF heating. In addition, high flux operation was achieved by applying the ICRF heating for anchor-cells of GAMMA 10/PDX and the ion particle flux was enhanced to the value of 10^{23} particles/m²s. Since the plasma behaviors in anchor-cell play important roles during the high flux operations, numerical code was newly established and the transport of plasma particles between the central and anchor-cells are analyzed for the first time. Comparison between the calculated result and the result of high flux experiments, it was found that the collision rate of the plasma can be a critical factor in the high flux experiments of GAMMA 10/PDX. By the analysis of collision frequency, the importance of the ion temperature for enhancing the end-loss particle flux was revealed. Those understanding will sufficiently contribute to the divertor simulation study and the improvement of a tandem mirror operations.

Acknowledgements

The author would like to express his greatest appreciation to Prof. Y. Nakashima at University of Tsukuba for his generous support, elaborated guidance, and considerable encouragement in the course of the present study. Without his help, the present study would not have been possible.

He would particularly like to thank to Prof. M. Ichimura and T. Imai for their advice, comment and continuing interest in the present study.

He also wishes to thank to Prof. M. Sakamoto, M. Yoshikawa and T. Kariya for his insightful comments and suggestions.

He would like to deeply appreciate Dr. K. Hosoi, H. Ueda, M. Hirata, R. Minami R. Ikezoe, K. Oki, and M. Mizuguchi for their helpful advices.

He also wishes to express his appreciation to H. Takeda, T. Yokoyama and Y. Morikawa for their helpful discussions and advises.

This study is partly supported by the bi-directional collaboration research program of National Institute for Fusion Science and University of Tsukuba.

Finally he would like to thank the members of GAMMA 10 groups for their collaboration in the experiments and for helpful discussion.

References

- [1] J. Wesson, *Tokamaks*, Oxford University Press, [1997].
- [2] P. H. Rebut, *Fusion Eng. Design* **30** 85-118 [1995].
- [3] H. Kawashima et al., *Plasma Fusion Res.* **1**, 031 [2006].
- [4] D. Lumma, et al., *Phys. Plasmas* **4**, 2989 [1997].
- [5] N. Ohno et al., *Nucl. Fusion* **41** 1055 [2001].
- [6] S. Kado et al., *J. Plasma Fusion. Res.* **81** 810-821 [2005].
- [7] A. Tonegawa et al., *J. Advanced Science* **11** 232 [1999].
- [8] M. Sakamoto et al., *Phys. Scr.* **T138** 014043 [2009].
- [9] P. Korenejew et al., *Phys. Scr.* **T91** 29-32 [2001].
- [10] J. Scholten et al., *Fusion Eng. Des.* **88** 1785 [2013].
- [11] J. Rapp et al., *Fusion Sci. Technol.* **54** 237 [2013].
- [12] ITER Physics Expert Group on Divertor et al., *ITER Physics Basis*, *Nucl. Fusion* **39**, 2391 [1999].
- [13] M. Wischmeir et al., *J. Nucl. Mater.* **415**, S523 [2011].
- [14] O. V. Batishchev et al., *Physics of Plasmas* **4** 1672 [1997].
- [15] S. Shinohara et al., *Plasma Phys. Control. Fusion* **37** 1015 [1995].
- [16] G. M. W. Kroesen et al., *Plasma Chemistry and Plasma Processing* **10** 4 231 [1990].
- [17] Dazhi Liu et al., *J. Plasma Fusion Res. SERIES*, **8** 999-1002 [2009].
- [18] Y. Nakashima et al., *Fusion Eng. Design* **85** 956-962 [2010].
- [19] T. Imai et al., *Trans. Fusion Sci. Tech.* **63** 1T 8-15 [2013].
- [20] M. Inutake et al, *Physi. Rev. Lett.* **55** 939 [1985].
- [21] D. Maisonnier et al., *Fusion Eng. Des.* **81** 1123-1130 [2006].
- [22] K. Yatsu et al., *Nucl. Fusion* **39** No.11Y 1707 [1999].
- [23] S. Miyoshi, *Plasma Phys. Reports* **23** 723 [1997].
- [24] M. Ichimura et al., *Nuclear Fusion* **28**, 799 [1988].
- [25] M. Inutake et al., *J. Plasma Fusion Res.* **78** No.12 1352-1360 [2002].
- [26] T. Yokoyama et al., *Plasma Fusion Res.* **7** 2402136 [2012].
- [27] T. Imai et al., *J. Plasma Fusion Res.* **85**, 378-382 [2009].
- [28] Y. Nakashima et al *J. Nucl. Mater.* **313-316** 553-558[2003].
- [29] K. Hosoi et al., *Plasma Fusion Res.* **7** 2402126 [2012].
- [30] K. Hosoi, Ph. D. Thesis Univ. Tsukuba [2014].
- [31] M. A. Heald and C.B. Wharton, *Plasma Diagnostics with Microwaves*, John Wiley & Sons Inc., [1965].
- [32] R. Katsumata et al., *Jpn. J. apple. Phys.* **31** 2249-2254 [1992].

- [33] Y. Nakashima et al., Rev. Sci. Instrum. **70** 1 849-852 [1999].
- [34] M. Shoji, Ph. D. Thesis Univ. Tsukuba [1995].
- [35] M. Yoshikawa et al., Rev. Sci. Instrum. **83** 10E333 [2012].
- [36] H. Takeda et al., Plasma Fusion Res. **7** 2405147 [2012].
- [37] M. Iwamoto et al., Plasma Fusion Res. **9** 3402087 [2014].
- [38] R. Yonenaga et al., Plasma Fusion Res. **5** S2045 [2010].
- [39] S. Kigure et al., Trans. Fusion Sci. Technol. **63** 1T 241-243 [2013].
- [40] Y. Miyata et al., J. Plasma Fusion Res. SERIES **9** 84-87 [2010].
- [41] K. Kurihara et al., J. Phys. Soc. Jpn. **58** 3453 [1989].
- [42] W. Molvik, Rev. Sci. Instrum. **52** 704 [1981].
- [43] J. H. Foote et al., Rev. Sci. Instrum. **56** 5 [1985].
- [44] T. Kuwabara et al., Rev. Sci. Instrum. **65** 936-942 [1994].
- [45] Y. Nakashima et al., Trans. Fusion Sci. Tech. **63** 1T 100-105 [2013].
- [46] Y. Nakashima et al., J. Nucl. Mater. **438** S738 [2013].
- [47] H. Takeda, Master Thesis, Univ Tsukuba [2012].
- [48] K. Ichimura et al., Plasma Fusion Res. **7** 2405147 [2012].
- [49] K. Ichimura et al., Trans. Fusion Sci. Technol. **63** 1T 209-212 [2013].
- [50] R. H. Cohen et al., Nucl. Fusion **20** 1421 [1980].
- [51] E. E. Yushmanov, J. Exptl. Theoret. Phys. (U.S.S.R.) **49** 588-598 [1965].
- [52] K. Ichimura et al., Plasma Fusion Res. **9** 3406098 [2014].
- [53] K. Nemoto et al., Trans. Fusion. Sci. Technol. **51** 223-225 [2007].
- [54] H. Shidara et al., Fusion Eng. Design **86** 913-915 [2011].
- [55] H. Ozawa et al., Plasma Fusion Res. **5** S2084 [2010].
- [56] H. Ueda et al., Trans. Fusion Sci. Technol. **63** 1T 316-318 [2013].
- [57] H. Sugawara, Master Thesis, Univ. Tsukuba [1989].
- [58] M. Yoshida, Ph. D. Thesis Univ. Tsukuba [2004].
- [59] M.A. Leontovich, Review of Plasma Physics ed. Acad. (Consultants Bureau, New York) vol. I, p.205 [1966].
- [60] H. Aminaka Master Thesis Univ. Tsukuba [2001].
- [61] R. Minai et al., J. Phys. Soc. Jpn. **66** 7 2051-2056 [1997].